

THE NUMERICAL MODELING OF AN ANTENNA IN PLASMA

by

Jeffrey D. Ward

A dissertation submitted in partial fulfillment
of the requirements for the degree

of

DOCTOR OF PHILOSOPHY

in

Electrical Engineering

Approved:

Dr. Charles M. Swenson
Major Professor

Dr. Robert Schunk
Committee Member

Dr. Bela Fejer
Committee Member

Dr. Randy Jost
Committee Member

Dr. George Liang
Committee Member

Dr. Byron R. Burnham
Dean of Graduate Studies

UTAH STATE UNIVERSITY
Logan, Utah

2006

Copyright © Jeffrey D. Ward 2006

All Rights Reserved

Abstract

The Numerical Modeling of an Antenna in Plasma

by

Jeffrey D. Ward, Doctor of Philosophy

Utah State University, 2006

Major Professor: Dr. Charles M. Swenson

Department: Electrical and Computer Engineering

This dissertation presents a full-wave, self-consistent numerical model that enables a greater understanding of how an antenna interacts with warm, collisional, magnetized, multi-species plasma. The model focuses primarily on the frequency region around the critical electron resonances for ionospheric plasma conditions. At these resonances, the dielectric representation of the plasma can become complex or negative, and the current distribution strongly deviates from free space. These effects are difficult to model analytically, necessitating the use of numerical techniques. This dissertation develops a Finite Difference Time Domain model that includes the plasma fluid equations along with Maxwell's equations, and incorporates boundary conditions that address the various speeds of energy propagation. A linearized version of the model allows the simulation to run for hundreds of plasma periods. Simulation results show that the self-consistent current distributions differ from those assumed in analytical models. One outcome of this difference in current distributions is a shift of the zero-phase input impedance crossing of the upper hybrid to a lower frequency than predicted by analytic theories. Additional discrepancies in the input impedance between analytical and numerical models appear to be a consequence of more accurately modeling the near and far fields around an antenna. Qualitative comparisons between simulations of dipole and patch antennas in plasma, and experimental observations of ionospheric sounding

rockets and laboratory plasma chambers, demonstrate the improved accuracy and flexibility of the numerical model over analytical techniques. This model should enable the use of the input impedance of an antenna in plasma as a more complete diagnostic tool for measuring plasma environment.

(166 pages)

To my family.

Acknowledgments

This project has been funded in part by the following organizations:

Space Dynamics Laboratory (SDL)

National Aeronautics and Space Administration (NASA) Grant NAG5-13026

Air Force Research Laboratory (AFRL)

Jeffrey D. Ward

Contents

	Page
Abstract	iii
Acknowledgments	vi
List of Figures	x
Notations	xvii
Acronyms	xix
1 On the Shoulders of Giants	1
1.1 Antennas in a Plasma	2
1.2 C-Probes	3
1.3 Conservation of Energy Principal	8
1.3.1 The Induced Electromotive Force and Quasi-Static Model	10
1.3.2 A Plasma Dielectric Tensor	12
1.4 Analytical Theories of an Antenna Input Impedance in Plasma	16
1.4.1 Balmain	17
1.4.2 Varying the Current Distribution	19
1.4.3 Other Analytical Models	19
1.5 Numerical Modeling of Antennas in a Plasma	20
1.5.1 Recursive-Convolution Electromagnetic Simulations	21
1.5.2 Particle in Cell	23
1.5.3 The Fluid Equations	24
1.6 Thesis Overview	26
2 The Improved Plasma Fluid Finite Difference Time Domain (PF-FDTD) Model	29
2.1 Fundamental Equations	30
2.1.1 The Nonlinear Fluid Model	30
2.1.2 The Linear Fluid Model	31
2.2 Discretization	33
2.2.1 Spatial Discretization	34
2.2.2 Temporal Discretization	36
2.3 PF-FDTD Discrete Equations	37
2.3.1 Nonlinear Equations	37
2.3.2 Linear Equations	41
2.4 Boundary Condition	47
2.5 Defining the Antenna	49
2.5.1 Thin Wire Model	50

2.5.2	Microstrip Patch Model	51
2.6	Driving the Antenna	53
2.6.1	Multi-Frequency Analysis	55
2.6.2	Single-Frequency Analysis	56
2.7	Additional PF-FDTD Issues	57
2.7.1	Simulation Units and the Covrant Condition	57
2.7.2	Initial Conditions	57
3	Validating the Plasma Fluid Finite Difference Time Domain (PF-FDTD) Model	59
3.1	Free-Space Validation	60
3.2	Numerical Stability and Accuracy	64
3.2.1	Effects of the Decoupling Boundary Conditions	64
3.2.2	Bandwidth of Driving Source	68
3.2.3	Maximum Iteration	68
3.2.4	Nonlinear Versus Linear Models	71
3.3	Nonmagnetized Plasma Results	71
3.4	Magnetized Plasma with an Incident Angle of Zero	82
3.4.1	Plasma Frequency > Cyclotron Frequency	85
3.4.2	Plasma Frequency < Cyclotron Frequency	93
3.5	Magnetized Plasma with Various Incident Angles	97
3.5.1	Plasma Frequency > Cyclotron Frequency	97
3.5.2	Plasma Frequency < Cyclotron Frequency	101
3.6	Additional Observations	103
3.6.1	Varying the Electron Neutral Collision Frequency	107
3.6.2	Temperature and Sheath Effects	109
3.6.3	Ion Effects	110
3.6.4	Far Fields Effects	111
4	Specific Applications of the PF-FDTD	115
4.1	The Air Force Research Lab Experiment	115
4.1.1	The Experiment	115
4.1.2	The Data	117
4.1.3	The Models	118
4.2	EWIND's Ion Probe Data	119
4.3	A Microstrip RF Plasma Impedance Probe	121
4.3.1	The Design	121
4.3.2	The Analysis	122
4.3.3	The Flight	123
5	Conclusion	127
5.1	The PF-FDTD Summary	127
5.2	Future Work	130
References		132

Appendices	136
Appendix A Users Guide to the PF-FDTD Program and Supporting Software	137
A.1 The Fundamental Program (The PF-FDTD)	137
A.1.1 .STR File	138
A.1.2 .VC File	141
A.1.3 .FD File	141
A.2 Matlab Files	142
A.2.1 PF-FDTD_imp	142
A.2.2 PF-FDTD_field	143
Appendix B Index Of Attached CD	145
Vita	146

List of Figures

Figure	Page
1.1 Variations in the real and imaginary parts of the input impedance for a short dipole in a plasma according to Pfister's model.	6
1.2 A modified Clemmow-Mullaly-Allis (CMA) diagram	15
1.3 CMA diagram showing the simplified interpretation of the input impedance of a probe based upon the value of ϵ	16
1.4 Simplified version of the input impedance of a dipole parallel to the ambient magnetic field.	17
1.5 Various theoretical approximations for a dipole immersed in a plasma.	18
2.1 The PF-FDTD Yee cell.	35
2.2 The PF-FDTD leap frog technique.	36
2.3 Interdependency of fields for different spatial locations near the PF-FDTD boundary.	47
2.4 A representation of a thin wire dipole antenna.	50
2.5 A representation of a microstrip patch antenna.	52
2.6 Grid values used to calculate the feed terms.	54
3.1 The comparison of a 1-meter dipole in free-space and the PF-FDTD, for various L and R values.	62
3.2 The comparison of a 1-meter dipole in free-space and the PF-FDTD, for various dx values.	63
3.3 E_z with and without the decoupling boundary condition.	65
3.4 Effectiveness of warm plasma boundary conditions using different sized simulations.	66
3.5 Variations in density at different locations with a simulation space.	67
3.6 Various applied voltage sources for a 1-meter dipole in a magnetized cold plasma.	69

3.7 Maximum iterations in plasma cycles versus simulation size for various plasma environments ran using the nonlinear model.	70
3.8 A 1.1 m dipole antenna with in a cold collisional magnetized plasma simulated run for various maximum iterations.	72
3.9 The PF-FDTD versus Balmain for a 1.24 m x 0.004 m dipole for various plasma densities	73
3.10 The magnitude of the current distribution along a 1.24 m x 0.004 m dipole antenna immersed in plasma density of 1.24×10^6 1/cc($f_p = 10MHz$) for various drive frequencies.	74
3.11 The phase of the current distribution along a 1.24 m x 0.004 m dipole antenna immersed in plasma density of 1.24×10^6 1/cc($f_p = 10MHz$) for various drive frequencies	75
3.12 The magnitude and phase of the current distribution along a 1.24 m x 0.004 m dipole antenna immersed in plasma density of 1.24×10^6 1/cc($f_p = 10MHz$) for a few fixed drive frequencies.	75
3.13 Physical location of the density, kinetic energy, and Poynting vector measurements with respect to the probes' feed point.	78
3.14 Temporal and frequency fluctuations in the electron density, 1 m away from the feed point of a 1.24 m x 0.004 m dipole antenna immersed in plasma density of 1.24×10^6 1/cc($f_p = 10MHz$).	78
3.15 Temporal and frequency fluctuations in the radial instantaneous and average kinetic energy, 1 m away from the feed point of a 1.24 m x 0.004 m dipole antenna immersed in plasma density of 1.24×10^6 1/cc($f_p = 10MHz$).	80
3.16 Temporal and frequency fluctuations in the radial instantaneous and average Poynting vector, 1 m away from the feed point of a 1.24 m x 0.004 m dipole antenna immersed in plasma density of 1.24×10^6 1/cc($f_p = 10MHz$).	82
3.17 The PF-FDTD versus Balmain for a 1.24 m x 0.004 m dipole for weak various magnetic field strengths.	83
3.18 The PF-FDTD versus Balmain for a 1.24 m x 0.004 m dipole with a plasma density of 1.24×10^6 1/cc and two magnetic fields.	84
3.19 The magnitude of the current distribution along a 1.24 m x 0.004 m dipole antenna immersed in plasma density of 1.24×10^6 1/cc($f_p = 10MHz$) with a magnetic field of 2.5×10^{-4} Tesla ($f_g = 7MHz$) for various drive frequencies near the upper hybrid resonance.	86

3.20 The phase of the current distribution along a 1.24 m x 0.004 m dipole antenna immersed in plasma density of 1.24×10^6 1/cc($f_p = 10MHz$) with a magnetic field of 2.5×10^{-4} Tesla ($f_g = 7MHz$) for various drive frequencies near the upper hybrid resonance.	86
3.21 The magnitude and phase of the current distribution along a 1.24 m x 0.004 m dipole antenna immersed in plasma density of 1.24×10^6 1/cc($f_p = 10MHz$) with a magnetic field of 2.5×10^{-4} Tesla ($f_g = 7MHz$) for a select few drive frequencies around the upper hybrid frequency.	87
3.22 The magnitude and phase of the current distribution along a 1.24 m x 0.004 m dipole antenna immersed in plasma density of 1.24×10^6 1/cc($f_p = 10MHz$) with a magnetic field of 2.5×10^{-4} Tesla ($f_g = 7MHz$) for a select few drive frequencies around the plasma frequency.	88
3.23 The magnitude of the current distribution along a 1.24 m x 0.004 m dipole antenna immersed in plasma density of 1.24×10^6 1/cc($f_p = 10MHz$) with a magnetic field of 2.5×10^{-4} Tesla ($f_g = 7MHz$) for various drive frequencies near the gyro resonance.	89
3.24 The phase of the current distribution along a 1.24 m x 0.004 m dipole antenna immersed in plasma density of 1.24×10^6 1/cc($f_p = 10MHz$) with a magnetic field of 2.5×10^{-4} Tesla ($f_g = 7MHz$) for various drive frequencies near the gyro resonance.	89
3.25 The magnitude and phase of the current distribution along a 1.24 m x 0.004 m dipole antenna immersed in plasma density of 1.24×10^6 1/cc($f_p = 10MHz$) with a magnetic field of 2.5×10^{-4} Tesla ($f_g = 7MHz$) for a select few drive frequencies around the gyro frequency.	90
3.26 Fluctuations in the electron density 1 m away from the feed point of a 1.24 m x 0.004 m dipole antenna emersed in plasma density of 1.24×10^6 1/cc($f_p = 10MHz$) with a magnetic field of 2.5×10^{-4} Tesla ($f_g = 7MHz$).	91
3.27 Fluctuations in the radial instantaneous and average kinetic energy 1 m away from the feed point of a 1.24 m x 0.004 m dipole antenna immersed in plasma density of 1.24×10^6 1/cc($f_p = 10MHz$) with a magnetic field of 2.5×10^{-4} Tesla ($f_g = 7MHz$).	91
3.28 Fluctuations in the radial instantaneous and average Poynting vector 1 m away from the feed point of a 1.24 m x 0.004 m dipole antenna immersed in plasma density of 1.24×10^6 1/cc($f_p = 10MHz$) with a magnetic field of 2.5×10^{-4} Tesla ($f_g = 7MHz$).	92
3.29 The magnitude of the current distribution along a 1.24 m x 0.004 m dipole antenna immersed in plasma density of 1.24×10^6 1/cc($f_p = 10MHz$) with a magnetic field of 4.6×10^{-4} Tesla ($f_g = 13MHz$) for various drive frequencies.	94

3.30 The phase of the current distribution along a 1.24 m x 0.004 m dipole antenna immersed in plasma density of 1.24×10^6 1/cc($f_p = 10MHz$) with a magnetic field of 4.65×10^{-4} Tesla ($f_g = 13MHz$) for various drive frequencies.	94
3.31 The magnitude and phase of the current distribution along a 1.24 m x 0.004 m dipole antenna immersed in plasma density of 1.24×10^6 1/cc($f_p = 10MHz$) with a magnetic field of 4.65×10^{-4} Tesla ($f_g = 13MHz$) for a select few drive frequencies.	95
3.32 Fluctuations in the electron density 1 m away from the feed point of a 1.24 m x 0.004 m dipole antenna immersed in plasma density of 1.24×10^6 1/cc($f_p = 10MHz$) with a magnetic field of 4.6×10^{-4} Tesla ($f_g = 13MHz$).	96
3.33 Fluctuations in the radial instantaneous and average kinetic energy 1 m away from the feed point of a 1.24 m x 0.004 m dipole antenna immersed in plasma density of 1.24×10^6 1/cc($f_p = 10MHz$) with a magnetic field of 4.6×10^{-4} Tesla ($f_g = 13MHz$).	96
3.34 Fluctuations in the radial instantaneous and average Poynting vector 1 m away from the feed point of a 1.24 m x 0.004 m dipole antenna immersed in plasma density of 1.24×10^6 1/cc($f_p = 10MHz$) with a magnetic field of 4.6×10^{-4} Tesla ($f_g = 13MHz$).	97
3.35 The PF-FDTD versus Balmain for a 1.24 m x 0.004 m dipole for various magnetic field incident angles for $f_p > f_g$	98
3.36 The magnitude of the current distribution along a 1.24 m x 0.004 m dipole antenna immersed in plasma density of 1.24×10^6 1/cc($f_p = 10MHz$) with a magnetic field of 2.5×10^{-4} Tesla ($f_g = 7MHz$) at an incident angle of 90° for various drive frequencies.	99
3.37 The phase of the current distribution along a 1.24 m x 0.004 m dipole antenna immersed in plasma density of 1.24×10^6 1/cc($f_p = 10MHz$) with a magnetic field of 2.5×10^{-4} Tesla ($f_g = 7MHz$) at an incident angle of 90° for various drive frequencies.	100
3.38 The magnitude of the current distribution along a 1.24 m x 0.004 m dipole antenna immersed in plasma density of 1.24×10^6 1/cc($f_p = 10MHz$) with a magnetic field of 2.5×10^{-4} Tesla ($f_g = 7MHz$) at an incident angle of 90° for drive frequencies below $1/2f_p$	100
3.39 The phase of the current distribution along a 1.24 m x 0.004 m dipole antenna immersed in plasma density of 1.24×10^6 1/cc($f_p = 10MHz$) with a magnetic field of 2.5×10^{-4} Tesla ($f_g = 7MHz$) at an incident angle of 90° for drive frequencies below $1/2f_p$	101

3.40 Fluctuations in the electron density 1 m away from the feed point of a 1.24 m x 0.004 m dipole antenna immersed in plasma density of 1.24×10^6 1/cc($f_p = 10MHz$) with a magnetic field of 2.5×10^{-4} Tesla ($f_g = 7MHz$) at an incident angle of 90° .	102
3.41 Fluctuations in the radial instantaneous and average kinetic energy 1 m away from the feed point of a 1.24 m x 0.004 m dipole antenna immersed in plasma density of 1.24×10^6 1/cc($f_p = 10MHz$) with a magnetic field of 2.5×10^{-4} Tesla ($f_g = 7MHz$) at an incident angle of 90° .	102
3.42 Fluctuations in the radial instantaneous and average Poynting vector 1 m away from the feed point of a 1.24 m x 0.004 m dipole antenna immersed in plasma density of 1.24×10^6 1/cc($f_p = 10MHz$) with a magnetic field of 2.5×10^{-4} Tesla ($f_g = 7MHz$) at an incident angle of 90° .	103
3.43 The PF-FDTD versus Balmain for a 1.24 m x 0.004 m dipole for various magnetic field incident angles for $f_p > f_g$.	104
3.44 The magnitude of the current distribution along a 1.24 m x 0.004 m dipole antenna immersed in plasma density of 1.24×10^6 1/cc($f_p = 10MHz$) with a magnetic field of 4.6×10^{-4} Tesla ($f_g = 13MHz$) at an incident angle of 90° for various drive frequencies.	104
3.45 The phase of the current distribution along a 1.24 m x 0.004 m dipole antenna immersed in plasma density of 1.24×10^6 1/cc($f_p = 10MHz$) with a magnetic field of 4.6×10^{-4} Tesla ($f_g = 13MHz$) at an incident angle of 90° for various drive frequencies.	105
3.46 Fluctuations in the electron density 1 m away from the feed point of a 1.24 m x 0.004 m dipole antenna immersed in plasma density of 1.24×10^6 1/cc($f_p = 10MHz$) with a magnetic field of 4.6×10^{-4} Tesla ($f_g = 13MHz$) at an incident angle of 90° .	105
3.47 Fluctuations in the radial instantaneous and average kinetic energy 1 m away from the feed point of a 1.24 m x 0.004 m dipole antenna immersed in plasma density of 1.24×10^6 1/cc($f_p = 10MHz$) with a magnetic field of 4.6×10^{-4} Tesla ($f_g = 13MHz$) at an incident angle of 90° .	106
3.48 Fluctuations in the radial instantaneous and average Poynting vector 1 m away from the feed point of a 1.24 m x 0.004 m dipole antenna immersed in plasma density of 1.24×10^6 1/cc($f_p = 10MHz$) with a magnetic field of 4.6×10^{-4} Tesla ($f_g = 13MHz$) at an incident angle of 90° .	106
3.49 The PF-FDTD for a 1.24 m x 0.004 m dipole with a plasma density of 2.94×10^4 1/cc and a magnetic field of 3.2×10^{-4} Tesla for various electron-neutral collision rates.	108

3.50 The PF-FDTD for a $1.2 \text{ m} \times 0.01 \text{ m}$ dipole with a plasma density of $7.15 \times 10^4 \text{ 1/cc}$ ($f_p = 2.4 \text{ MHz}$), a magnetic field of $5.36 \times 10^{-5} \text{ Tesla}$ ($f_g = 1.5 \text{ MHz}$), and a electron neutral collision frequency of 0.1 MHz for various isotropic plasma temperatures.	109
3.51 A PF-FDTD simulation results showing the lower hybrid resonance frequency	110
3.52 Density fluctuations in the plane of the antenna for a $1.2 \text{ m} \times 0.03 \text{ m}$ dipole antenna immersed in plasma density of $1.24 \times 10^6 \text{ 1/cc}$ ($f_p = 10 \text{ MHz}$) with a magnetic field of $2.5 \times 10^{-4} \text{ Tesla}$ ($f_g = 7 \text{ MHz}$) at an incident angle of 0°	111
3.53 Radial kinetic energy fluctuations in the plane of the antenna for a $1.2 \text{ m} \times 0.03 \text{ m}$ dipole antenna immersed in plasma density of $1.24 \times 10^6 \text{ 1/cc}$ ($f_p = 10 \text{ MHz}$) with a magnetic field of $2.5 \times 10^{-4} \text{ Tesla}$ ($f_g = 7 \text{ MHz}$) at an incident angle of 0°	112
3.54 Radial Poynting vector fluctuations in the plane of the antenna for a $1.2 \text{ m} \times 0.03 \text{ m}$ dipole antenna immersed in plasma density of $1.24 \times 10^6 \text{ 1/cc}$ ($f_p = 10 \text{ MHz}$) with a magnetic field of $2.5 \times 10^{-4} \text{ Tesla}$ ($f_g = 7 \text{ MHz}$) at an incident angle of 0°	112
4.1 One of the space environment test chambers located at the Air Force Research Lab in Bedford, Massachusetts.	116
4.2 The physical dimensions of the mono pole antenna use for the AFRL experiments.	116
4.3 A picture of the RF and Langmuir probes placed with in the plasma stream.	116
4.4 The input impedance magnitude of the AFRL RF probe.	117
4.5 The input impedance phase of the AFRL RF probe.	118
4.6 The magnitude and phase of a 1.75 inch monopole (3.5 inch dipole) immersed in plasma density of $4.96 \times 10^6 \text{ 1/cc}$ ($F_p = 20 \text{ MHz}$) with a magnetic field of 3 gauss ($F_g = 0.8 \text{ MHz}$) according to Balmain and the PF-FDTD.	119
4.7 The trajectories of the EWind sounding rocket campaign.	120
4.8 Un-calibrated sweeps of the ion sweeping probe on board flight 41.037 of the EWinds sounding rocket campaign showing the possible presence of the lower hybrid resonance.	121
4.9 A free space FD simulation showing the various constant potential surface for a surface-mounted Debye Modified microstrip Patch (DMP).	123
4.10 The effects of a magnitized collisional plasma at various incident angles on the input impedance of the DMP PIP according to the PF-FDTD.	124

4.11 A surface-mounted Debye Modified microstrip Patch (DMP).	125
4.12 The location of the DMP PIP in reference to the dipole PIP for the EQUIS II sounding rocket campaign.	125
4.13 Uncalibrated magnitude data from the DMP PIP on one of the up leg flights showing the presents of the F-region with in the ionosphere.	126
5.1 Various approximations of the input impedance for a dipole immersed in a plasma, including the PF-FDTD.	129
A.1 A Matlab graphical user interface designed to aid in the analysis of the .vc files.	143
A.2 A Matlab graphical user interface designed to aid in the analysis of the .fd files.	144

Notations

Throughout this dissertation, all entities are assumed to be either scalars or vectors, unless otherwise mentioned. The following conventions will be used for typesetting mathematics.

- 1) Scalar: Can be in both lower and upper cases, such as α, k_1, C_1, G, M .
- 2) Vector: In lower and upper cases with a vector sign above the term, such as \vec{B} .
- 3) Unit Vector: In lower and upper case with at (^) above the term, such as $\hat{x}, \hat{y}, \hat{z}$.

In addition \hat{n} represents the unit vector normal to a surface.

- 4) Tensors: In lower and upper case with double bars above the term, such as $\bar{\epsilon}, \bar{\bar{A}}$.
- 5) Function: In both lower and upper cases with the functional variables in parentheses following the term, such as $w(\cdot), A(\cdot), \mathcal{F}(\cdot)$.
- 6) Constant components and or free space values of a vector: In lower and upper case with a zero subscript, such as n_o, \vec{B}_o .
- 7) Small perturbations of a vector: In lower and upper case with a one subscript, such as n_1, \vec{B}_1 .
- 8) Scalar components of a vector: In lower and upper case with a subscript denoting the direction (x, y , or z), such as E_x .

In the case of a constant or small perturbation, scalar components appear as subsubscript, such as V_{0_y}, B_{1_z}

- 9) Specific plasma species: In lower and upper case with a subscript denoting the species (s in general, e specifically for electrons), such as n_s, m_e, \vec{V}_s

In the case of a scalar component, plasma species appear as subsubscript, such as V_{z_s}

In the case of a constant or small perturbation of a scalar component, plasma species appear as subsubsubscript, such as $V_{0_{xs}}, V_{1_{zs}}$

- 10) Temporal instance: In lower and upper case with a superscript denoting the instance in time, such as $n^t, E_x^t, B_{0_y}^t, V_{0_{zs}}^t$
- 11) Spatial instance: In lower and upper case with spatial variables (i for \hat{x} , j for \hat{y} , and k for \hat{z}) in a function form, such as $n^t(i, j, k), E_x^t(i, j, k), B_{0_y}^t(i, j, k), V_{0_{zs}}^t(i, j, k)$

Unless otherwise mentioned, variables that maintain the same representation throughout this dissertation are listed below.

Variable	Description
c_0	Speed of light in free space, 2.9979×10^8 m/s
j	$\sqrt{-1}$
k_b	Boltzmann constant, 1.3807×10^{-23} J/K
m_e	Mass of electron, 9.1094×10^{-31} kg
q	Fundamental charge, 1.6022×10^{-19} C
ϵ	Permittivity
θ	Incident angle of the constant ambient magnetic field
λ	Wave length
μ	Permeability
ν	Collision frequency
ρ	Charge density
Φ	Electric scalar potential
A	Magnetic vector potential
B	Magnetic flux density
C	Capacitance
dx, dy, dz	spatial increment
dt	temporal increment
E	Electric field strength
H	Magnetic field strength
I	Electrical current
J	Current density
l	Physical location along a dipole antenna
L	Half length of a dipole antenna
m	Mass of particle
n	Density
R	Radius of a dipole antenna
s	Plasma species
sx, sy, sz	Simulation size
S	Poynting vector
t	Time
T	Temperature
U	Average velocity
\mathcal{V}	Instantaneous velocity
V	Electrical voltage
Z	Input impedance
k	Propagation constant ($k = \frac{2\pi}{\lambda}$)
λ_d	Debye length ($\lambda_d = \sqrt{\frac{\epsilon k_b T}{e q^2}}$)
ω, f	Frequency ($\omega = 2\pi f$)
ω_p, f_p	Plasma frequency ($\omega_p = \sqrt{\frac{nq^2}{\epsilon m}}$)
Ω, f_g, f_c	Gyro / Cyclotron frequency ($\Omega = \frac{ q B_o}{m}$)
ω_{uh}, f_{uh}	Upper hybrid resonance ($\omega_{uh}^2 = \omega_p^2 + \Omega^2$)
ω_{lh}, f_{lh}	Lower hybrid resonance ($\omega_{lh}^2 = \Omega_e \Omega_i$)

Acronyms

AC	Alternating Current
AFRL	Air Force Research Lab
BC	Boundary Conditions
CMA	Clemmow Mullaly Allis diagram
DC	Direct Current
DMP	Debye Modified Microstrip Patch
EM	Electromagnetics
FD	Finite Difference
FDTD	Finite Difference Time Domain Model
FE	Finite Element
FFT	Fast Fourier Transform
MOM	Method of Moments
PC	Personal Computer
PF-FDTD	Plasma Fluid Finite Difference Time Domain Model
PIC	Particle in Cell Simulation
PIP	Plasma Impedance Probe
PML	Perfectly Matched Layers
RF	Radio Frequency
USU	Utah State University

Chapter 1

On the Shoulders of Giants

The concept of performing measurements has always been a challenge. Something as simple as measuring the ambient temperature on a nice summer day can present countless complications. If a thermometer is in the Sun, the solar energy that impacts the mercury or other sensing fluid can easily yield a false high temperature reading of the ambient air. On the other hand, a nice breeze can yield an apparent temperature below the actual value. If one closely considers the various effects the environment can have on a simple thermometer and its operating principals, the study of measuring air temperature can become a science all of its own. This is true for many other types of environmental measurements. The term metrology is used to describe the science of measurements. One such field of study, for which this thesis has application, is the measurement of the plasma environment.

Plasma, often called the fourth state of matter, is a collection of both positively and negatively charged particles that exhibit collective effects. It is typically created from neutral atoms or molecules through the absorption of a high-energy photon or the collision with a high-energy particle. In these interactions, the energy that is imparted to the atom or molecule excites an electron causing it to leave its orbit around the nuclei. This process, which is akin to a satellite leaving the gravitational bounds of Earth, results in a collection of negatively charged free electrons and positively charged particles called ions. As the free electrons and ions recombine to form neutral atoms, the process releases a photon of light. This is part of the physics that results in the light we see from the sun or the glow of the aurora at night. The stability of a plasma environment depends on the production and recombination rates of electrons and ions.

The closest collection of sustained plasma to the surface of the Earth is the ionosphere. A region in the upper atmosphere starting at an altitude of about 90 km and continuing

outward. However, unsustainable plasma is a common everyday occurrence. The advent of fluorescent lighting, plasma televisions, and even the dry etching of silicon wafers to make today's integrated circuits all depend upon plasmas. In order to truly gain an understanding of a plasma environment one must be able to measure it.

Many methods can be used to measure the various plasma conditions. However, most if not all are limited by either the physics of constructing such a device or the understanding of the principles behind the probe plasma interaction. The most common method for diagnosing a plasma is a Langmuir probe [1]. Yet, when one dives into the metrology of Langmuir probes, one finds problems with effects that are not completely modeled in the basic theory of these probes. Contamination on the surface or work function variations across the material the probe is constructed of introduce errors in the actual plasma readings [2]. Other effects due to charging of nearby insulators or the reference point for the probes electronics, such as the spacecrafts skin, can make basic measurements problematic. Another technique commonly used to diagnose space plasmas is the Radio Frequency (RF) probe [3–7]. However, the major limiting problem in using RF probe techniques is the lack of a sufficiently rigorous theory of probe plasma interactions. It is here that this thesis begins. In that, this thesis will present a new tool that can more accurately analyze the RF probe plasma interaction when a small alternating current (AC) is applied to the antenna or probe.

1.1 Antennas in a Plasma

Ever since Jackson and Kane first recorded an unexpected feature on the input impedance of an antenna in the plasma environment [4, 8], researchers have attempted to quantify the interaction and make use of its effects as a plasma diagnostic. However, as Balmain noted in a literature review on this subject in 1979, the combination of decreased federal spending and increased theoretical difficulties forced many of the leading scientists to pursue more plausible plasma probe techniques [9]. Only a few institutions have continued to study the effects of plasma on an antenna, and its use as a plasma diagnostic. This trend continues to this day, with Utah State University being one of the few institutions that has had a

sustained program in using and advancing RF probe theories for space plasma diagnostics.

At the heart of most of this research has been the concept that an antenna is little more than a transformer. It transforms electrical signals (voltages and currents) into electromagnetic waves (electric and magnetic fields). And like most transformers, antennas can also relate the impedance on one side of the device to an effective impedance upon the other side of the device. However, this concept of impedance transformation is complicated by the fact that in the world of electromagnetics (EM) there are no real resistors, inductors, and capacitors. Instead, there are only the concepts of energy either radiating away, being dissipated in some media, or being temporary stored within fields near the antenna.

The addition of a plasma as the medium near the antenna complicates the electromagnetic theory. Energy radiated away from the antenna can take on new modes of propagation in the form of plasma waves and the energy stored in the near field is effected by the dynamics of the free charged particles. The antenna behavior originally seen by Jackson and Kane was the result of energy leaving the antenna and resonating with the plasma environment at frequencies that provide an efficient coupling to the movement of the free plasma particles. It is this coupling of energy between the electrical signals and the plasma through the geometry of the antenna, that enable the RF probe to be used as a measurement device. However, this can only be done if there exists a theory capable of adequately describing the interaction for the frequencies of interest and the range of plasma parameters encountered. What follows is a review of the different approaches to understanding the impedance characteristics of an antenna-like probe in a plasma.

1.2 C-Probes

In its simplest form, an electrically short antenna (physical lengths much smaller than the free space electromagnetic wave length) can be treated very much like a capacitor. Plasma probes based on this technique are generally called C-probes. Conceptually, these electrically short antennas have a fundamental impedance of

$$Z_{antenna} = \frac{-j}{\omega C_o} \quad (1.1)$$

where $\omega = 2\pi f$ is the radian drive frequency and f is the frequency in Hz. In other words, the characteristics of an antenna in free space can be entirely described by a simple capacitance (C_o). This capacitance is a good description until the frequency approaches the point where the antenna is no longer electrically short. As the drive frequency continues to increase and the free space wave length begins to approach the size of the antenna, the probe will begin to develop a resistive component at the antenna resonates as described by traditional electromagnetic antenna theory [10].

When the antenna is immersed in plasma, its electrical characteristics change due to being surrounded by highly mobile charged carriers and the ability of the plasma to support collective effects. Depending upon the conditions, the collective effects lead to various resonance frequencies within the plasma. The most basic of these resonances is the electron plasma frequency (ω_p), given as

$$\omega_p = \sqrt{\frac{n_e q^2}{\epsilon_0 m_e}} . \quad (1.2)$$

The plasma frequency depends upon the density of the free electrons (n_e), the fundamental charge (q), the free space permittivity (ϵ_0), and the mass of an electron (m_e). The simplest approximation of the effect of a plasma on an antenna is obtained by treating the plasma as a dielectric. For operating frequencies $\omega > \omega_p$, the relative permittivity (ϵ_r) of a plasma is given by

$$\epsilon_r = \left(1 - \frac{\omega_p^2}{\omega^2}\right) . \quad (1.3)$$

Limiting the discussion to electrically short antennas, the capacitance of the antenna can then be determined from the effects of immersing the antenna in a dielectric material. Conceptually, the antenna can be considered as if it were a parallel plate capacitor with some effective area and some effective separation between the plates. This gap between the plates can then be filled with the simple dielectric representation of a plasma

$$C = \epsilon_r C_0 = \left(1 - \frac{\omega_p^2}{\omega^2}\right) C_o . \quad (1.4)$$

If the plasma is modeled as a lossy dielectric, due to electron neutral collisions (ν_{en}), the relative permittivity becomes

$$\epsilon_r = 1 - \frac{\omega_p^2}{\omega^2 - j\omega\nu_{en}} . \quad (1.5)$$

The addition of a collision frequency converts the relative permittivity to a complex number that when combined with the impedance calculation of a capacitor, not only modifies the reactive component (X) of the impedance, but also adds a resistive component (R)

$$Z = \frac{1}{j\omega\epsilon_r C_0} = R + jX . \quad (1.6)$$

This resistive component captures the effect of energy lost as the electrons collide with the neutral particles.

It is possible to substitute 1.5 into 1.6 and solve for the plasma density and collision frequency, if the free space capacitance (C_0) of the antenna is known. Additional precision can be gained, given the inherent limitations in instrumentation, by measuring the difference from a free space value ($\Delta Z = Z_{total} - Z_{freespace} = \Delta R + j\Delta X$). These formulas are known as Pfister's theory [11]:

$$n_e = \frac{\omega^2 m_e \epsilon_0}{q^2} \left[\frac{\Delta X + \frac{\Delta R^2}{\Delta X}}{\Delta X + \frac{\Delta R^2}{\Delta X} + \frac{1}{\omega C_0}} \right] , \quad (1.7)$$

$$\nu = \frac{\omega \frac{\Delta R}{\Delta X}}{1 + \omega C_0 \left(\Delta X + \frac{\Delta R^2}{\Delta X} \right)} . \quad (1.8)$$

When Pfister's relationships are plotted, fig. 1.1, the effect of the plasma becomes apparent. However, fig. 1.1 also reveals that there are complicating factors limiting the application of this technique to actual measurement data from a capacitance probe in the Earth's lower ionosphere. For instance, the ratio of change in the resistive and the reactive components of the impedance are approximately the same. Like a true capacitor, the resistive component tends to be very small, making its measurement extremely difficult when compared to the large values of the reactive part. This causes $\frac{\Delta R}{\Delta X}$ and $\frac{\Delta R^2}{\Delta X}$ to approach zero. While this

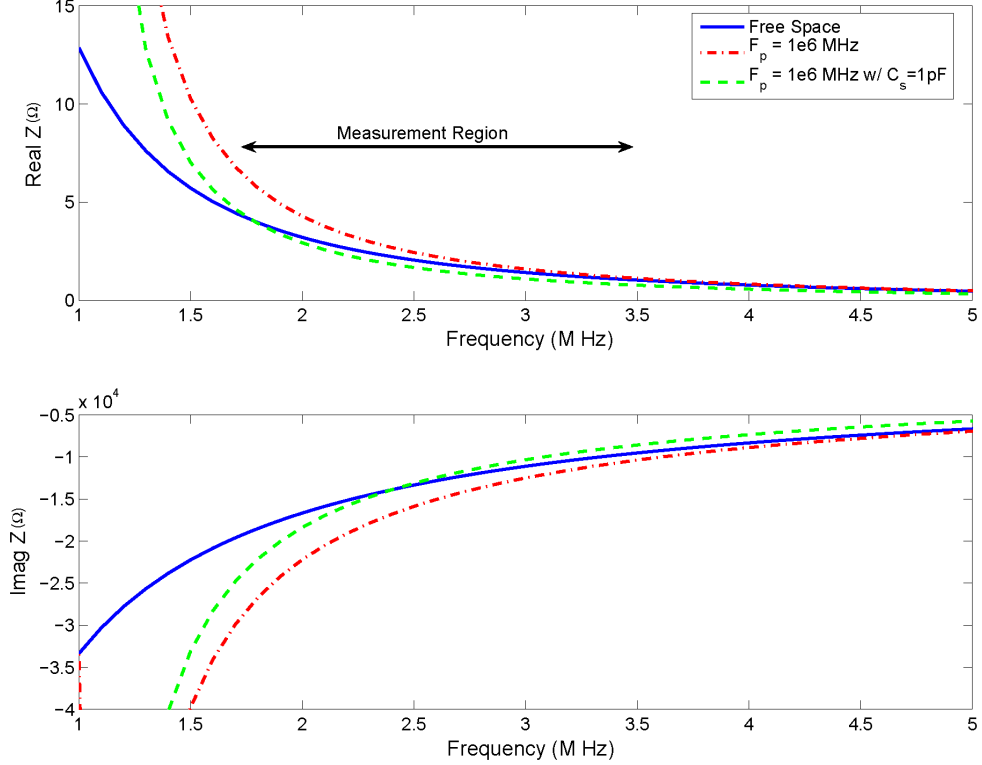


Fig. 1.1: Variations in the real and imaginary parts of the input impedance for a short dipole in a plasma according to Pfister's model.

fact simplifies equation 1.7 to

$$n_e = \frac{\omega^2 m_e \epsilon_0}{q^2} \left[\frac{\Delta X}{\Delta X + \frac{1}{\omega C_0}} \right] , \quad (1.9)$$

it also makes it impossible to determine the collision frequency, as equation 1.8 converges to zero [3]. This limits the application of this theory to cases of very high collisional rates or where only the electron density is desired.

The antennas typically used for C-probes tend to have a free space capacitance on the order of 5 pF or smaller, and typically are used to measure effective capacitance changes of about 10% – 20%, depending upon the operating frequency of the probe. In some cases, the antenna's natural capacitance can even be on the same order as capacitance of the

transmission line or some of the connectors used to attach the device to the measuring electronics. This combined unwanted shunt capacitance can be the dominant error in a poorly designed or poorly calibrated probe. Figure 1.1 also shows the effect that a single 1pF shunt capacitance can have on a C-probe. The fact that the shunt capacitance can shift the resulting curve makes it imperative that its effects be mitigated. One way to address shunt capacitance is to measure it prior to flight and incorporate the additional capacitance by modifying equations 1.7 and 1.8 with a known factor of

$$\left[\frac{C_{shunt} + C_0}{C_0} \right]. \quad (1.10)$$

A similar capacitance effect can also be seen when the floating potential of the probe varies far from the ambient plasma potential, creating a sheath region around the antenna. This sheath region evacuates the plasma from part of the area between the antenna elements, creating a purely free space capacitor in series with the plasma filled capacitor. This additional shunt capacitance can also occur if the space around the antenna is only partially filled with plasma due to the probe geometry. Unlike the transmission line shunt capacitance, which can be measured prior to launch, this sheath or geometrical shunt capacitance cannot be measured and can greatly affect the use of these probes. This is the predominant reason why many institutions have had difficulties in implementing RF probes for plasma diagnostics.

Finally, care must also be taken in choosing the frequency at which these measurements are made. If the operating frequency is too high in comparison to the plasma frequency the plasma effects are hard to qualitatively measure, see fig. 1.1, or if the frequencies are too close or less than ω_p the approximations, equations 1.3 and 1.5, become invalid and additional plasma physics can no longer be neglected. These facts limit the usefulness of the C-probe, due to the limitations of Pfister's theory and suggest the need for a more complete analysis technique.

1.3 Conservation of Energy Principal

While some insight can be gained from merely treating the antenna as a capacitor in a dielectric medium, even more can be gained by understanding the electromagnetic fields around the probe. To understand these fields one must consider Maxwell's equations:

$$\nabla \times \vec{E} = -\mu \frac{\partial \vec{H}}{\partial t}, \quad (1.11)$$

$$\nabla \times \vec{H} = \epsilon \frac{\partial \vec{E}}{\partial t} + \vec{J}_{int} + \vec{J}_{ext}, \quad (1.12)$$

$$\nabla \cdot \vec{H} = 0, \quad (1.13)$$

$$\epsilon_0 \epsilon_r \cdot \vec{E} = \rho_{ext}, \quad (1.14)$$

where \vec{E} represents the electric field, \vec{H} the magnetic field, t time, \vec{J} currents, ρ the free charge density, and ϵ and μ are the permittivity and permeability of the medium respectively. In addition, the currents in equation 1.12 are separated into the displacement current, the current within the plasma as a result of applied electric fields (\vec{J}_{int}), and the current supplied by the antenna (\vec{J}_{ext}).

An energy equation can be formed for the fields and currents associated with the antenna plasma system by summing the dot product of equation 1.11 with \vec{H} with the dot product of equation 1.12 with \vec{E} . Through the application of the vector identity

$$\nabla \cdot (\vec{A} \times \vec{B}) = \vec{B} \cdot (\nabla \times \vec{A}) - \vec{A} \cdot (\nabla \times \vec{B}), \quad (1.15)$$

the following conservation of energy law for a differential volume element is obtained

$$\nabla \cdot (\vec{E} \times \vec{H}) = -\vec{E} \cdot \vec{J}_{int} - \vec{E} \cdot \vec{J}_{ext} - \left(\vec{H} \cdot \mu \frac{\partial \vec{H}}{\partial t} + \vec{E} \cdot \epsilon \frac{\partial \vec{E}}{\partial t} \right). \quad (1.16)$$

The left-hand side of equation 1.16 is the divergence of the Poynting vector ($\vec{S} = \vec{E} \times \vec{H}$) and accounts for the energy flow transported by electromagnetic waves. The first term on right-hand side is the energy generated by currents internal to the medium. The second term is the energy generated on the surface of the antenna. By limiting the analysis to a

macroscopic discussion of a linear medium, the final term can be rewritten as

$$\frac{\partial}{\partial t} \left(\frac{\mu \vec{H}^2 + \epsilon \vec{E}^2}{2} \right). \quad (1.17)$$

This term represents the energy stored in the fields and is analogous to the energy stored within a capacitor or inductor.

A better physical understanding of the impedance of an antenna in a plasma medium can be obtained by integrating equation 1.16 over the volume (\mathbb{V}),

$$\int_{\mathbb{V}} \nabla \cdot (\vec{E} \times \vec{H}) d\mathbb{V} = - \int_{\mathbb{V}} \vec{E} \cdot \vec{J}_{int} d\mathbb{V} - \int_{\mathbb{V}} \vec{E} \cdot \vec{J}_{ext} d\mathbb{V} - \int_{\mathbb{V}} \frac{\partial}{\partial t} \left(\frac{\mu \vec{H}^2 + \epsilon \vec{E}^2}{2} \right) d\mathbb{V}, \quad (1.18)$$

external to the antenna surface, \mathbb{A} , and bounded by a far field surface, \mathbb{B} , that can be set to infinity.

The Divergence theorem can be used to rewrite the first term as the Poynting vector flow of energy away from the antenna, across surface \mathbb{B} . This is the well-known far field flow of energy. The second term collapses to a surface integral at \mathbb{A} , the antenna surface, because of the non existence of \vec{J}_{ext} throughout the rest of the volume. The other terms represent the energy dissipated in the plasma medium and stored in the fields near the antenna, respectfully. If one further assumes that all the fields vary sinusoidally in time as $e^{j\omega t}$, where $j = \sqrt{-1}$, and amplitudes (\vec{E} , \vec{J} , and \vec{H}) are peak value phasor quantities, then equation 1.18 becomes

$$- \int_{\mathbb{A}} \vec{E} \cdot \vec{J}_{ext} d\mathbb{S} = \int_{\mathbb{B}} (\vec{E} \times \vec{H}) \cdot \hat{n} d\mathbb{S} + \int_{\mathbb{V}} \vec{E} \cdot \vec{J}_{int} d\mathbb{V} + j\omega \int_{\mathbb{V}} \left(\frac{\mu \vec{H}^2 + \epsilon \vec{E}^2}{2} \right) d\mathbb{V} \quad (1.19)$$

where \hat{n} represents the normal vector to the surface \mathbb{B} at infinity.

In addition, by assuming no losses within the antenna structure itself, the power flow across the antenna's surface (\mathbb{A}) must be equal to the power input at the antenna's terminals. This conservation of power can be expressed as

$$\frac{1}{2} I_o \cdot I_o^* Z = - \int_{\mathbb{A}} \vec{E} \cdot \vec{J}_{ext} d\mathbb{S}. \quad (1.20)$$

Where the traditional electrical engineering concepts of an antenna impedance ($Z = R + jX$) and the peak phasor representation of the current (I_o) at the antennas terminals are used. Thus the resistive part of an antenna's impedance is related to the energy flow away from the antenna or dissipated in the medium,

$$I_o^2 R = 2 \int_{\mathbb{B}} (\vec{E} \times \vec{H}) \cdot \hat{n} dS + 2 \int_{\mathbb{V}} \vec{E} \cdot \vec{J}_{int} dV , \quad (1.21)$$

and the reactive part of the antenna's impedance is related to the energy stored in the fields and waves near the antenna

$$I_o^2 X = \omega \int_{\mathbb{V}} \mu \vec{H}^2 + \epsilon \vec{E}^2 dV . \quad (1.22)$$

1.3.1 The Induced Electromotive Force and Quasi-Static Model

The analytical solution of equation 1.20 requires the knowledge of both the electric field and current distribution along the antenna's surface. The approach that is commonly found in the literature is to prescribe a current distribution and then calculate the resulting electric field. This is the induced electromotive force (EMF) method.

The electric field can be represented as a combination of a scalar potential and a vector potential

$$\vec{E} = -\nabla\Phi - \frac{\partial \vec{A}}{\partial t} . \quad (1.23)$$

As the antenna becomes electrically short, free space theory predicts a significant decrease in the radiated energy ($\vec{S} \rightarrow 0$), allowing for the use of a quasi-static approximation ($\frac{\partial \vec{A}}{\partial t} \rightarrow 0$) for the electric field. By applying the quasi-static approximation for an electrically short antenna in a non-isotropic medium, Poisson's and Gauss's equations can be written as

$$\vec{E} = -\nabla\Phi , \quad (1.24)$$

$$\nabla \cdot (\bar{\epsilon} \cdot \vec{E}) = \rho , \quad (1.25)$$

where $\bar{\epsilon}$ is a tensor dielectric representation of the plasma environment.

Substituting 1.24 into 1.25 and performing a plane wave analysis ($\vec{E}(\vec{r}) = \vec{E}_0 e^{j(\vec{k}\vec{r} - \omega t)}$), an expression relating the scalar potential to the charged density can be obtained

$$-(\vec{k} \cdot \bar{\epsilon} \cdot \vec{k})\Phi = \rho . \quad (1.26)$$

The expression $\vec{k} \cdot \bar{\epsilon} \cdot \vec{k}$ is also called the dispersion relation for plasma waves, relating the state of energy propagation within waves to the material parameters.

A prescribed current distribution (\vec{J}_{ext}) will also stimulate the charges along the surface of the antenna according to the continuity equation,

$$-j\omega\rho + j\vec{k} \cdot \vec{J}_{ext}(\vec{k}) = 0 , \quad (1.27)$$

converted into \vec{k} space.

Substituting the charge density of equation 1.26 into 1.27, it becomes possible to relate the potential around the antenna to the current distribution along the conductors

$$\vec{k} \cdot \bar{\epsilon} \cdot \vec{k}\Phi = \frac{\vec{k} \cdot \vec{J}_{ext}(\vec{k})}{\omega} . \quad (1.28)$$

Solving for the scalar potential,

$$\Phi = -\frac{1}{\omega} \left(\frac{\vec{k} \cdot \vec{J}_{ext}(\vec{k})}{\vec{k} \cdot \bar{\epsilon} \cdot \vec{k}} \right) , \quad (1.29)$$

and inserting into the plane wave version of equation 1.24, it becomes possible to develop an expression relating the prescribed current distribution to the electric field perpendicular to the surface of the antenna,

$$\vec{E}_\perp = -\frac{j}{\omega} \left(\frac{\vec{k} [\vec{k} \cdot \vec{J}_{ext}(\vec{k})]}{\vec{k} \cdot \bar{\epsilon} \cdot \vec{k}} \right) , \quad (1.30)$$

since $\vec{E}_\parallel = 0$ for a perfectly conducting antenna.

Equation 1.30 can then be applied to equation 1.20 to develop a relationship for the input impedance of an antenna [12]

$$Z(\omega) = \frac{j}{2\pi\omega|I_o|^2} \int \frac{[\vec{k} \cdot \vec{J}_{ext}(\vec{k})] [\vec{k} \cdot \vec{J}_{ext}^*(\vec{k})]}{\vec{k} \cdot \bar{\epsilon} \cdot \vec{k}} d\vec{k}. \quad (1.31)$$

The 2π term results from using Parseval's theorem to convert the spatial integral of equation 1.20 to a k space integral.

Equation 1.31, while a simplified equation relating the input impedance of an antenna to the current distribution along the probe in a dielectric type material, introduces a subtlety that complicates the actual derivation process. As the dielectric representation of the plasma is frequency dependent, there exist critical frequencies, at which the dispersion relationship enters a cut-off ($\vec{k} \cdot \bar{\epsilon} \cdot \vec{k} = 0$) or resonance condition ($\vec{k} \cdot \bar{\epsilon} \cdot \vec{k} = \infty$) [13]. At the cut-off frequencies, poles are introduced in the equation, which symbolize a change in the mode of energy propagation. These sometimes complex poles, force the use of contour integration and the use of the residue theory. Even the derivation of an arbitrary dielectric tensor becomes problematic [14]. However, with advanced analytical techniques, as Nakatani and Kuehl demonstrated using a kinetic dielectric tensor for a warm collisional plasma, equation 1.31 can be evaluated for a few select orderings of plasma critical frequencies [15].

1.3.2 A Plasma Dielectric Tensor

The dielectric tensor contains essentially all of the information about the electromagnetic properties of a plasma. While many different dielectric representations of the plasma environment exist [13,16,17], the development of a dielectric representation becomes important in analytically analyzing the input impedance of equation 1.31. For a cold collisional, non-drifting plasma of electrons and immobile ions, the derivation of the dispersion relationship in equation 1.31, begins by solving the momentum equation for a relationship relating the particles instantaneous velocity (\vec{V}) to the applied fields,

$$m \frac{\partial \vec{V}}{\partial t} = q(\vec{E} + \vec{V} \times \vec{B}) - m\nu \vec{V}. \quad (1.32)$$

Transforming the time derivative to a frequency domain (Fourier transform) and orienting the system so that the ambient magnetic field is purely along the \hat{z} -axis, it becomes possible to equate the instantaneous velocities to the electric field components

$$\mathcal{V}_x = \frac{q}{m\omega} \frac{jE_x(1 - j\nu/\omega) - \Omega/\omega E_y}{(1 - j\nu/\omega)^2 - \Omega^2/\omega^2}, \quad (1.33)$$

$$\mathcal{V}_y = \frac{q}{m\omega} \frac{jE_y(1 - j\nu/\omega) - \Omega/\omega E_x}{(1 - j\nu/\omega)^2 - \Omega^2/\omega^2}, \quad (1.34)$$

$$\mathcal{V}_z = -\frac{jq}{m\omega} \frac{E_z}{1 - j\nu/\omega}, \quad (1.35)$$

where Ω represents the gyro frequency,

$$\Omega = \frac{qB_0}{m}. \quad (1.36)$$

Once these relationships are developed, Ohms law ($\vec{J} = qn\vec{\mathcal{V}}$) can be used to relate the velocity of the charged particles to the current within the plasma, \vec{J}_{int} in equation 1.12. Since it is now possible to express the internal plasma current as a function of the electric field, it can be combined with the displacement current ($j\omega\epsilon_0\vec{E}$), creating an effective displacement current and a relative dielectric tensor $\bar{\epsilon}_r$,

$$\nabla \times \vec{H} = j\omega\epsilon_0\vec{E} + \vec{J}_{int} = j\omega\epsilon_0\bar{\epsilon}_r \cdot \vec{E}. \quad (1.37)$$

The dielectric tensor for a cold, collisional, magnetized plasma typically is written as

$$\bar{\epsilon}_r = \begin{pmatrix} \epsilon_1 & -j\epsilon_2 & 0 \\ j\epsilon_2 & \epsilon_1 & 0 \\ 0 & 0 & \epsilon_3 \end{pmatrix}, \quad (1.38)$$

$$\epsilon_1 = 1 - \frac{\omega_p^2(1 - j\nu/\omega)}{\omega^2(1 - j\nu/\omega)^2 - \Omega^2}, \quad (1.39)$$

$$\epsilon_2 = \frac{\omega_p^2\Omega/\omega}{\omega^2(1 - j\nu/\omega)^2 - \Omega^2}, \quad (1.40)$$

$$\epsilon_3 = 1 - \frac{\omega_p^2}{\omega^2(1 - j\frac{\nu}{\omega})^2}, \quad (1.41)$$

which can then be used in evaluating the dispersion relationship, $\vec{k} \cdot \bar{\epsilon} \cdot \vec{k}$, in equation 1.31.

Limiting the discussion to collisionless plasma, equations 1.39-1.41 can be decomposed further into [13],

$$\epsilon_1 = \frac{1}{2}(\mathcal{R} + \mathcal{L}), \quad (1.42)$$

$$\epsilon_2 = \frac{1}{2}(\mathcal{R} - \mathcal{L}), \quad (1.43)$$

$$\epsilon_3 = 1 - \frac{\omega_p^2}{\omega^2}, \quad (1.44)$$

where

$$\mathcal{R} = 1 - \frac{\omega_p^2}{\omega(\omega + \Omega)}, \quad (1.45)$$

$$\mathcal{L} = 1 - \frac{\omega_p^2}{\omega(\omega - \Omega)}. \quad (1.46)$$

It is at this point that some of the singularities of the dielectric tensor that are problematic to the dispersion equation in 1.31 become apparent. One way to graphically interpret the results is through the use of a Clemmow-Mullaly-Allis (CMA) diagram. Typically used to identify the wave normal surface of the propagating plane wave, it can also represent the various states of the dielectric tensor and the dispersion relationship, see fig. 1.2. An antenna immersed in a cold collisionless magnetized plasma with free electrons and immobile ions, will launch various plane waves as its drive frequency is swept from a frequency above the plasma effects to Direct Current (DC). At high frequencies, the lower left corner of fig. 1.2, all of the components of the dielectric tensor are positive. This implies that energy can be radiated in all directions. As the drive frequency decreases and the probe moves to the upper right, following the dotted line path, various parts of the dielectric tensor become negative. A negative dielectric represents an evanescent type plane wave.

Qualitatively, if one limits the analysis to only the radial dielectric component with

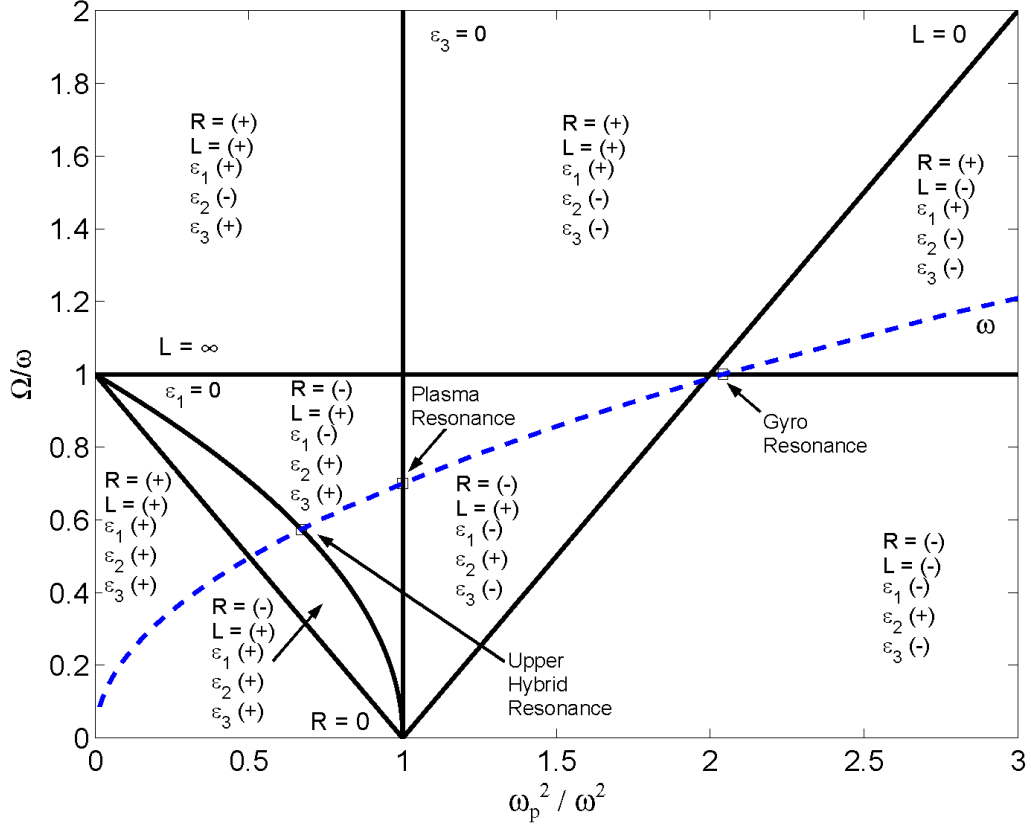


Fig. 1.2: A modified Clemmow-Mullaly-Allis (CMA) diagram for electrons with immobile ions. Solid lines represent boundaries at which part of the dielectric tensor either goes into cut-off (0) or resonance (∞). The areas between the lines represent a region with a common type of dielectric tensor. As the probes drive frequency is varied, it will sweep across the CMA diagram in a manner similar to the dotted line.

respect to the antenna, fig. 1.2 can be converted into fig. 1.3 [18]. For frequencies above the plasma resonance ($\omega_P^2/\omega^2 > 1$), the radial component parallel to the magnetic field (ϵ_3) is positive. This causes the reactance, from equation 1.31 to appear capacitive ($X = 1/j\omega\epsilon C$). Once the drive frequency is below the plasma resonance ($\omega_P^2/\omega^2 < 1$), ϵ_3 becomes negative, increasing the reactance, similar to an inductor ($X = j\omega\epsilon L$). A similar argument can also be presented concerning ϵ_1 , the radial component for the impedance perpendicular to the magnetic field. Z_{\perp} is inductive in nature for frequencies below the upper hybrid ($\omega_{uh}^2 = \omega_p^2 + \Omega^2$), but higher than the gyro frequency, and capacitive for all others. The transition from the capacitor to the inductor at the upper hybrid resonance is similar to an electrical parallel resonance circuit, see fig. 1.4. This is also true for the transition of the

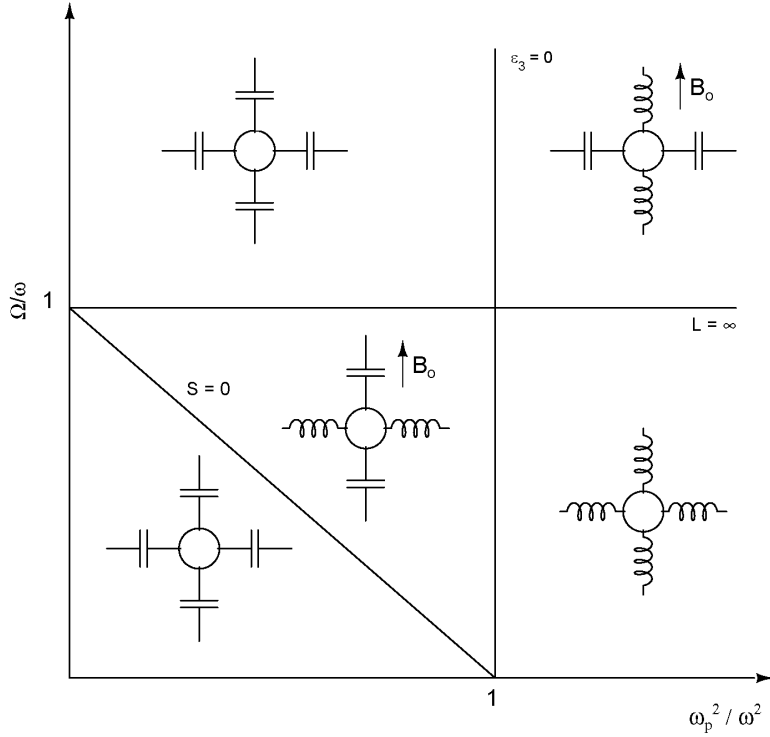


Fig. 1.3: CMA diagram showing the simplified interpretation of the input impedance of a probe based upon the value of the radial ϵ .

perpendicular inductor back to capacitor at the gyro frequency, akin to an electrical series resonance. There is also a minor effect as the parallel component transitions around the plasma resonance, as will be seen in Chapter 3.

1.4 Analytical Theories of an Antenna Input Impedance in Plasma

The scientific literature contains a number of theories for the properties of an antenna in a plasma. Various theories exist for antenna's in cold/warm, isotropic/anisotropic plasmas using fluid and kinetic models [14, 15, 19–28]. All of these theories generally share the limitations of equation 1.31, in that the derivations require both a prescribed current distribution along the antenna and a dielectric, or equivalent, representation of the plasma environment. The following is a review of some of the most important analytical methods used to date.

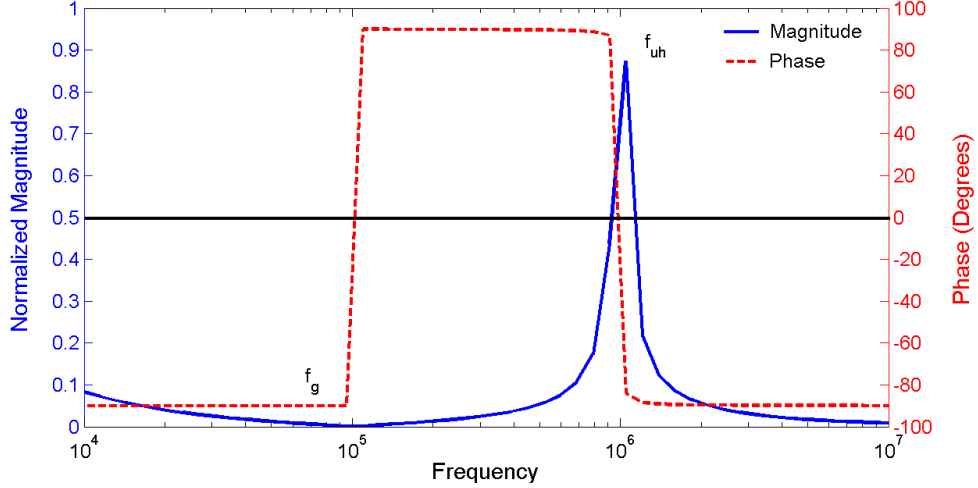


Fig. 1.4: Simplified version of the input impedance of a dipole parallel to the ambient magnetic field.

1.4.1 Balmain

K. G. Balmain was the first to develop a relatively simple expression for an antenna in a magnetized plasma. Limiting his analysis to the case of an electrically short dipole, Balmain was able assume a triangular current distribution along the length of an antenna immersed in a cold, collisional magnetized plasma [24, 29]. This assumption, when combined with the quasi-static analysis, enabled Balmain to convert the traditional free space impedance equation for a short dipole,

$$Z_{in} = \frac{1}{j\omega\pi\epsilon_0 L'} \left(\ln \frac{L'}{R'} - 1 \right), \quad (1.47)$$

into that of a short dipole in a plasma by only replacing the effective half length (L') and radius (R')

$$L' = L\sqrt{\epsilon_1 T}, \quad (1.48)$$

$$R' = \frac{R}{2} \left(\frac{\epsilon_1 \sqrt{\epsilon_3}}{\sqrt{T}} + \sqrt{\epsilon_1 \epsilon_3} \right), \quad (1.49)$$

$$T = \epsilon_0 \sin^2 \theta + \epsilon_1 \cos^2 \theta, \quad (1.50)$$

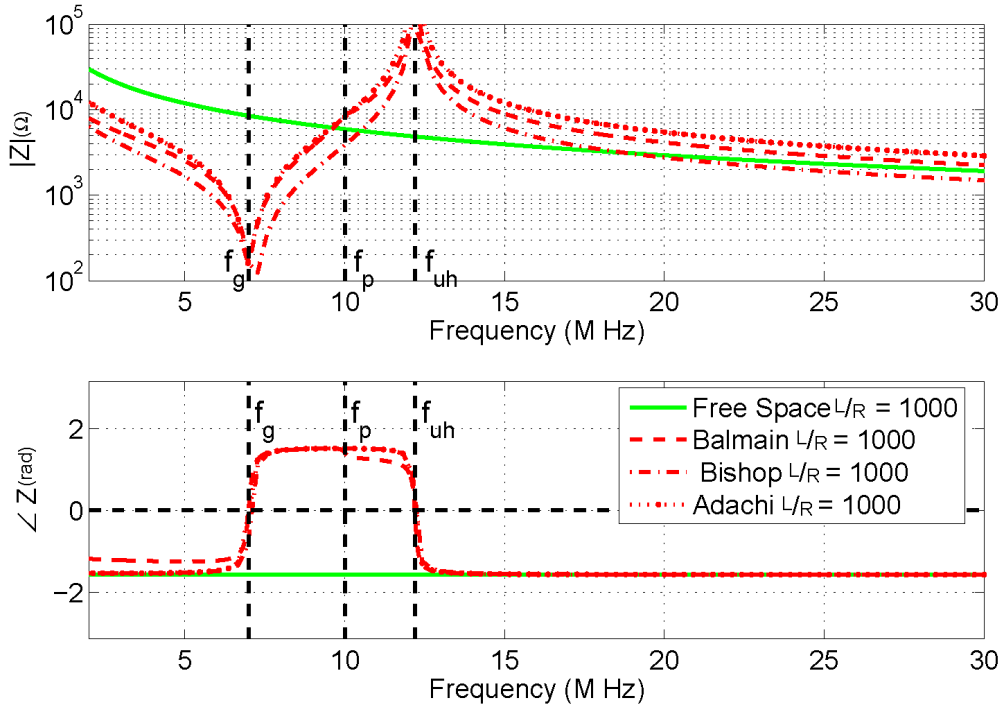


Fig. 1.5: Various theoretical approximations for a dipole immersed in a plasma.

that are dependent upon the tensor dielectric representation ($\bar{\epsilon}_r$ from 1.38) and the incident angle of the DC magnetic field (θ).

This yields vast improvements over the capacitive model of Pfister, specifically in the regions between the various critical plasma frequencies, where the simple scalar dielectric representation is no longer accurate. Figure 1.5 shows the effect that Balmain's theory has when compared to the free space impedance. The parallel (upper hybrid) and series (gyro) resonance, introduced in section 1.3.2, become apparent. A minor variation also can be noted at the plasma resonance. However, the concept of a resonance implies that the energy is effectively coupled from the antenna into the plasma. When this occurs the current distribution varies from the traditional triangular current, introducing errors in Balmain's model. In addition, at high frequencies the quasi-static analysis is unable to completely converge to the full wave analysis of Balanis [10].

1.4.2 Varying the Current Distribution

Realizing the dependence of Balmain's model on both the current distribution and the physical size of the antenna (electrically small), Adachi et al. developed a transmission line approximation of a dipole in a cold collisional magnetized plasma. Representing the antenna plasma interaction as a series inductor/shunt capacitor [26], Adachi enabled longer antennas to be modeled by daisy chaining additional transmission line segments together. This in effect, decreased the demand on prescribing the current distribution, since the resulting standing wave along the transmission line would self-consistently specify the current distribution. This effectively broadened the upper hybrid resonance, see fig. 1.5, which was more in line with experimental data [30].

The presence of Adachi's standing wave was also experimentally measured by Ishizone et al. [31] and later analytically explained by Singh [32]. Ishizone and Singh also noted the presence of an attenuation wave that at time superseded the standing wave. This was most noticeable at the upper hybrid and plasma resonances, where energy is reactively coupled.

If, instead of focusing on the traveling/standing wave, attention is devoted to the attenuating wave, the input impedance takes the form of Nikitin and Swenson. Nikitin and Swenson studied the effects of a 3D exponential current distribution upon an electrically short dipole [14]. This solution however, becomes the counter equation for Adachi's model. It more accurately matched the conditions near the upper hybrid, while sacrificing the regions where the traveling current distribution is dominate, the areas in between the resonance conditions.

1.4.3 Other Analytical Models

Modifications other than varying the current density, have also been presented in an attempt to accurately describe the antenna plasma interaction. One of the most notable was that of Andronov and Eidman. Realizing the limitations associated with prescribing the current distribution, Andronov and Eidman assumed the electric field distribution at the antenna's surface [23]. However, in order to make the solution tractable, Andronov and Eidman had to neglect the Joule losses, Landau damping and possible sheath effects. While

this, once again, increased the accuracy of the model near the resonance frequencies, the complexities of the solution combined with the added errors in the rest of the frequency spectrum made it difficult to apply to actual sounding rocket data sets.

Others such as Galejs [20], Kaiser and Tunaley [33], Bishop [34], Nakatani and Kuehl [15], and Meyer and Vernet [28] developed additional theories by varying either the current distribution, the analysis technique, or even the type of plasma being analyzed. However, the additional complexities in many cases cannot justify the improved accuracy over the simplistic theory of Balmain, equation 1.47. This is why to date, either Pfister's model (1.7) or Balmain's model are the primary techniques used for analyzing the input impedance of an antenna near or above the upper hybrid frequency at USU.

1.5 Numerical Modeling of Antennas in a Plasma

Numerical techniques are powerful methods for approaching problems where analytical methods have limitations. This is especially true for the impedance characteristics of an antenna in a plasma. The complexity of the plasma environment, gives researchers two choices; 1) make assumptions similar to those pointed out in the previous section, that limit the physics while allowing an analytical solution to be formulated, or 2) discretize the problem so that numerical modeling techniques can deal with the complexities of the real world. It should be noted however, that in the latter situation, the physical errors of the analytical methods are traded for the resolution limitations of the numerical models.

Many different numerical approaches exist, that could be applied to the problem of an antenna in the plasma environment, each with its own advantages and disadvantages [35].

1. The antenna can be divided into sections, each section or moment is then related to the environment by a resulting Green function. Combining all of the moments together in a set of linear equations, the Method of Moments (MOM) model can then be used to accurately determine the resulting current distribution, and the input impedance of the antenna. However, the approximations used in developing a Green function are similar to those used in developing the analytical models, resulting in a more complex

system that is incapable of significantly improving the results.

2. The space around the antenna, the plasma, can be decomposed into smaller blocks called cells. The parameters of interest are then assigned specific locations in the cell, and differential equations relating the parameters to each other are developed. Finite Differencing (FD) techniques are then used to spatially and temporally discretize the antenna/plasma environment according to the derivatives in the underlining equations. While this technique can greatly improve the modeled physics, it does so at the cost of additional computational resources, specifically one memory location for every parameter in every cell within the simulation space.
3. The Finite Element (FE) technique combines the spatial discretization of the FD method with the solving of linear equations from the MOM model. This method combines the accuracy of the physical model in the FD method, with the minimal resource requirements of the MOM. However, this is done at the cost of increased analytical derivations needed to relate the elements to each other.

While all of these techniques can be applied to a plasma environment, it is the combination of accuracy, and simplicity, which causes the Finite Difference Time Domain (FDTD) techniques to be used traditionally for numerical plasma models. As the plasma environment is changed to represent different situations, both the MOM and the FE underlying equations must be recalculated, while the simplicity of the FD method enables the plasma values to be directly input into the model. What follows is a dissection of several different FD numerical approaches that can be used to incorporate a plasma.

1.5.1 Recursive-Convolution Electromagnetic Simulations

One approach to include plasma effects in a FDTD model is to treat the plasma as a dielectric media. However, the dispersive nature of the plasma, $\epsilon(\omega)$, can in many ways be problematic for FDTD techniques. This is also compounded by the multiplication of the dielectric and the electric field in the frequency domain in Amperes equation (1.37). This

multiplication, when converted to the time domain, becomes a convolution of the electric field and the time domain representation of the dielectric [36, 37],

$$\nabla \times \vec{H} = \frac{\partial}{\partial t} \left(\int \vec{E}(t - \tau) \epsilon(\tau) d\tau \right) . \quad (1.51)$$

In the case of a cold collisional nonmagnetized plasma, the dielectric can be separated,

$$\epsilon(\omega) = \epsilon_0(1 + \chi(\omega)) , \quad (1.52)$$

into parts where the electrical susceptibility (χ) becomes

$$\chi(\omega) = \frac{\omega_p^2}{\omega^2(1 - j\frac{\nu}{\omega})^2} . \quad (1.53)$$

A Fourier transformation can be used to convert equation 1.53 in to

$$\chi(t) = \frac{\omega_p^2}{\nu} [1 - e^{-\nu t}] \mathcal{U}(t) , \quad (1.54)$$

where $\mathcal{U}(t)$ is the unit step function. This in turn allows the rewriting of Amperes equation (1.51) as

$$\nabla \times \vec{H} = \frac{\partial}{\partial t} \left(\epsilon_0 \vec{E} + \epsilon_0 \int_0^t \vec{E}(t - \tau) \chi(\tau) d\tau \right) . \quad (1.55)$$

By assuming \vec{E} is piece-wise constant, the integral of equation 1.55 can be converted into a summation,

$$\vec{E}^{t+1} = \alpha \vec{E}^{t+1} + \alpha \Psi^t + \frac{\alpha dt}{\epsilon_0} \nabla \times \vec{H}^{t+1/2} , \quad (1.56)$$

where

$$\alpha = \frac{1}{1 + \chi^0} , \quad (1.57)$$

$$\Psi^t = \sum_{\beta=0}^{t-1} \vec{E}^{t-\beta} \Delta \chi^\beta , \quad (1.58)$$

$$\Delta \chi^\beta = \chi^\beta - \chi^{\beta+1} , \quad (1.59)$$

$$\chi^0 = \frac{\omega_p^2 dt}{\nu} - \left(\frac{\omega_p^2}{\nu^2} \right) \left(1 - e^{-\nu dt} \right), \quad (1.60)$$

and dt represents the FDTD temporal increment.

It is also possible to reduce the computational load one step further, by realizing that the temporal electric susceptibility takes on an exponential form, and that the summation term,

$$\Psi^t = \Delta \chi^0 \sum_{\beta=0}^{t-1} \vec{E}^{t-\beta} e^{-\beta \nu dt}, \quad (1.61)$$

can be simplified to a simple recursive relationship,

$$\Psi^t = \Delta \chi^0 \vec{E}^t + e^{-\nu dt} \Psi^{t-1}. \quad (1.62)$$

While this is a relatively easy method of numerically representing the plasma environment surrounding a probe, it is only marginally better than Pfister's model, since it is incapable of anisotropy plasmas. Even after Hunsberger et al. extended this technique to magnetized plasma [38], it still only solves half of the problem with the analytical solutions. By using the complete set of Maxwell's equations, the recursive-convolution model is able to perform a full-wave analysis, enabling all of the energy that emanates from the antenna to be properly addressed. This also allows the model to yield a self-consistent solution for the current distribution along the antenna. However, this technique is highly dependent upon being able to calculate the temporal dependent dielectric constant for the plasma environment, a difficult task for multi-species warm collisional magnetized plasmas.

1.5.2 Particle in Cell

The most accurate of all numerical models is the Particle in Cell (PIC). This brute force technique is capable of modeling all of the plasma physics. PIC simulations, first calculate the fields emanating out of every individual particle, charge distribution, and current [39]. Second, these fields are then applied to the particles through the use of the Lorentz' force equation ($\vec{a}_s = \frac{q}{m_s}(\vec{E} + \vec{V}_s \times \vec{B})$). The PIC then displaces the particles by updating the

particles individual velocity and position. Once updated, the field effects of the new location are then calculated, as the simulation iteration repeats.

The resulting Particle in Cell (PIC) simulation can then be used to yield great insight into the actual effects external forces, such as an antenna, can have on the surrounding plasma. In fact, physical conditions such as sheath or particle acceleration are typically studied using PIC simulations [40, 41]. However, the fact that each individual particle, or small groups of particles, must be tracked, limits the physical size that PIC simulations can model. Current computer memory limitations force researchers to physically limit structures to less than a couple of Debye lengths, or a few mean free paths. This in turn, limits the usefulness of PIC simulations to regions such as the Solar Wind, where even a large antenna sees very few particles. Some researchers have also applied PIC models to other regions of space by approximating the antenna as an infinitely long conductor.

1.5.3 The Fluid Equations

Another complete set of equations that can describe the plasma environment is the Fluid equations. Derived from the moments of Vlasov's or Boltzmann's equation, the fluid model is an infinite series of moments, with each added equation adding additional physics to the model [42].

The first moment, or lowest order, of a Maxwellian distribution is the continuity equation,

$$\frac{\partial n_s}{\partial t} + \nabla \cdot (n_s \vec{U}_s) = \mathbf{P} - \mathbf{L} , \quad (1.63)$$

which states that any temporal or spatial change in a species density (n_s) resulting from an average velocity (\vec{U}_s), must be balanced by either a spatial change or a production (\mathbf{P}) or loss (\mathbf{L}) of the plasma.

The second moment, the conservation of momentum equation,

$$m_s n_s \left(\frac{\partial \vec{U}_s}{\partial t} + (\vec{U}_s \cdot \nabla) \vec{U}_s \right) = n_s q_s (\vec{E} + \vec{U}_s \times \vec{B}) - \nabla \cdot \vec{P}_s - m_s n_s \sum_{\alpha \neq \beta} \nu_{\alpha\beta} (\vec{U}_\alpha - \vec{U}_\beta) , \quad (1.64)$$

relates the velocity of the plasma species to a combination of the Lorentz force, external pressures (\vec{P}), and any collisions between species.

The third moment, the conservation of energy equations, balances out the energy sources and sinks. The Pressure Tensor equation, Heat Flow equation, and others each add additional accuracy to the fluid model, as higher and higher orders of physics are added. However, like most infinite series the fluid equations must be truncated by an equation of state. The point at which truncation occurs depends largely on the physics of interest. For the case of a plasma probe, the physical parameters of interest are the density, velocity, species, and temperature. The last one, the temperature (T), is the highest order of interest in many cases, enabling the fluid equations to be truncated with the ideal gas law,

$$\vec{P}_s = n_s k_b T , \quad (1.65)$$

where k_b is Boltzmann's constant ($1.3807 \times 10^{-23} J/K$).

These three partial differential equations 1.63-1.65 can then be used to calculate the induced current created by the plasma flow. Which, when incorporated into Maxwell's equations 1.11-1.14, yields the complete effects that an antenna can have on the plasma environment.

Young and Brueckner

Young and Brueckner were the first to present this technique for a free electron, stationary ion, plasma in one dimensional version to analyze wave propagation [43]. However, since they were not interested in plasma diagnostics, they combined the plasma temperature and density into a common pressure term (p), with the help of the ratio of specific heat (γ), causing the continuity equations to become

$$\frac{1}{\gamma p_0} \frac{\partial p}{\partial t} = -\nabla \cdot \vec{U} . \quad (1.66)$$

By also assuming a stationary ion and neutral fluid, only one momentum equation

was needed. Then, by limiting the model to the case of a single collision frequency for an incompressible flow, the momentum equation could be simplified to

$$mn_0 \frac{\partial \vec{U}}{\partial t} = n_0 q (\vec{E} + \vec{U} \times \vec{B}) - \nabla p - mn_0 \nu \vec{U}, \quad (1.67)$$

where n_0 represents the constant electron density.

The other equations; Maxwell's and Ohm's remained unchanged.

While Young and Brueckner showed great success for analyzing wave propagation at frequencies near the plasma resonance, their model oversimplified the plasma, limiting it's usefulness for studying the impedance of an antenna. In addition, by removing the density from the spatial derivative on the right hand side of equation 1.66, Young and Brueckner eliminated the possibility of modeling significant sheath effects and/or plasma drifts, both of which may have a factor in the input impedance of an antenna.

Olakangil

Olakangil independently developed a different Plasma Fluid Finite Difference Time Domain (PF-FDTD) model, and applied it directly to the characteristic impedance of an antenna in plasma [44]. However, due to the complexity of modeling the temperature, combined with developing a 3D version of the PF-FDTD with some type of boundary condition, Olakangil had to limit his model to cold collisional magnetized plasma. In addition, the boundary condition problems, which Young and Brueckner never addressed, cause Olagangil's PF-FDTD model to go unstable after just a few iterations, leading to highly suspectable results.

1.6 Thesis Overview

The input impedance on an electrically short antenna immersed in a plasma is an important topic for plasma diagnostics. The analytical theories that have been developed over the last 45 years have been successful in describing the antenna plasma interaction under a number of limiting assumptions and antenna geometries. This thesis develops and

reports on the results of a newly implemented Plasma Fluid Finite Difference Time Domain simulation. This simulation is capable of performing a fully three-dimensional, full-wave, self-consistent model that could potentially be used to model arbitrary antenna geometries.

This will be done by first analyzing and discretizing the fundamental equations. Specifically, the five moment Maxwellian incompressible isotropic plasma will be divided up into computational cells and combined with Maxwell's equations in such a way as to enable a computer to perform calculations for multiple cells and iterations. In fact, besides the limitation associated with the fundamental equations, the only additional limitation that will be applied to the PF-FDTD will be that of the computer memory and speed. While little can be done to maximize computational speed, the limitation of computer memory will be addressed by presenting a new set of decoupling boundary conditions. These new boundary conditions, when implemented properly, will enable the simulating of relatively complex structures for upwards of hundreds of plasma cycles. However, with the increased number of iterations comes the added error of rounding off the least significant digit, associated with each calculated data value. While traditionally ignored, for FDTD simulations that only run for hundreds of iterations, the PF-FDTD has to run for hundreds of thousands of iterations to maintain the required low frequency resolution around the plasma resonances. In fact, when these round off errors are multiplied against other sets of data with their own round-off errors, instabilities ensue. Besides developing the PF-FDTD, Chapter 2 will also address minimizing the effect of many of these round-off errors.

Once developed in Chapter 2, Chapter 3 will then apply the PF-FDTD to several specific plasma conditions, with the intent to completely characterize the antenna plasma interaction. The resulting input impedance curves, antenna current distributions, and near field variations will be analyzed as the PF-FDTD results are compared to the analytical theories. Where disagreements arise, Chapter 3 will also present logical arguments, backed by numerical data to prove the increased accuracy of the PF-FDTD.

Chapter 4 will then present a limited number of specific examples in which the PF-FDTD is used to shed additional light on the experiments, or used to improve the data

gathering capability of RF probes. Specifically, a laboratory experiment is used to verify some of the characteristics identified by the PF-FDTD, a set of sounding rocket data is used in conjunction with the PF-FDTD to open the door to the measurement of ion physics, and the PF-FDTD is used to aid in the development of a nondeployable RF plasma probe.

Throughout this thesis, the focus will be on developing a more accurate model of the antenna plasma interaction, which when applied to RF probes will enable scientists to gain a greater understanding of the plasma environment.

Chapter 2

The Improved Plasma Fluid Finite Difference Time Domain (PF-FDTD) Model

Two fundamental sets of Plasma Fluid Finite Difference Time Domain (PF-FDTD) equations will be presented in this chapter. The first, the “nonlinear” model, enables a way to perform a full wave self-consistent calculation of the input impedance of an antenna immersed within warm collisional multi-species magnetized plasma. A second model, with minor variations from the first, will also be developed in an attempt to improve the stability of the final simulation. This is done by linearizing terms in the plasma fluid continuity, momentum, and Ampere’s equations.

The addition of the fluid equations to the Finite Difference Time Domain (FDTD) model also introduces new forms of energy propagation traditionally not seen in classical FDTD simulations. As these “new” energy modes reach the simulations edge, traditional Electromagnetic (EM) Boundary Conditions (BC) are incapable of properly addressing this energy dissipation. As such, new decoupling BC are presented in an attempt to decrease the reflection of energy at the simulations edge. This enables the simulation to remain stable and allows it to be run long enough to simulate the antenna-plasma interaction.

This chapter also presents the modeling techniques needed to simulate two basic probe geometries; the thin wire and the microstrip patch, both of which have been used as experimental RF probe sensors. These geometries can be driven with either a broadband signal, to analyze the response of the antenna over a large range of frequencies, or a single sinusoid, to determine exact effects at a specific frequency. Once the antennas are defined and driven within the simulation space, the resulting fields can be monitored to determine the self consistent current distribution along the antenna. In the end, a fully described sim-

ulation, including units and the process for setting the initial conditions will be outlined. Throughout this chapter, the goal will be to present an accurate, full-wave self-consistent model for determining the antenna-plasma interaction.

2.1 Fundamental Equations

The PF-FDTD model is based upon Maxwell's equations and the 5-Moment Maxwellian fluid equations, with the ideal gas law used to truncate the series:

$$\nabla \times \vec{E} = -\frac{\partial \vec{B}}{\partial t}, \quad (2.1)$$

$$\nabla \times \vec{B} = \epsilon\mu \frac{\partial \vec{E}}{\partial t} + \mu \vec{J}, \quad (2.2)$$

$$\vec{J} = \sum_s q_s n_s \vec{U}_s, \quad (2.3)$$

$$\frac{\partial n_s}{\partial t} + \nabla \cdot (n_s \vec{U}_s) = \mathbf{P} - \mathbf{L}, \quad (2.4)$$

$$\begin{aligned} m_s n_s \left(\frac{\partial \vec{U}_s}{\partial t} + (\vec{U}_s \cdot \nabla) \vec{U}_s \right) &= n_s q_s (\vec{E} + \vec{U}_s \times \vec{B}) - \nabla \cdot \vec{P}_s \\ &\quad - m_s n_s \sum_{\alpha \neq s} \nu_{s\alpha} (\vec{U}_s - \vec{U}_\alpha), \end{aligned} \quad (2.5)$$

$$\vec{P}_s = n_s k_b T. \quad (2.6)$$

These equations are used to develop a model capable of simulating various plasma densities, temperatures, collision rates, magnetic fields, and even compositions (identified by the subscript s for species). The model to be presented is three dimensional and includes multiple sets of the fluid equations 2.4-2.6, one for each species. Thus it can be used to represent plasma environments ranging from pure electrons, with stationary ions and neutrals, to a full three fluid model with relative motion between the fluid species.

2.1.1 The Nonlinear Fluid Model

The 5-moment Maxwellian fluid model (2.1-2.6) is a simplification of the kinetic theory for plasma physics. In addition, three more minor approximations are made to the fundamental equations. It has been seen from current analytical theories, that each only present

a slight impact on the relevant antenna-plasma physics. The first approximation is that the plasma is subsonic, the compression term in the momentum equation ($(\vec{U}_s \cdot \nabla) \vec{U}_s$) is assumed to be small and ignored. Second, we assume that the production and loss terms are set to zero. Finally, the plasma will be treated as an isothermal medium with all species sharing a common temperature. After implementing these assumptions, with the fluid current rolled into Ampere's Law and the ideal gas law combined with the momentum equation, the model equations becomes;

$$\nabla \times \vec{E} = -\frac{\partial \vec{B}}{\partial t}, \quad (2.7)$$

$$\nabla \times \vec{B} = \epsilon\mu \frac{\partial \vec{E}}{\partial t} + \mu \sum_s q_s n_s \vec{U}_s, \quad (2.8)$$

$$\frac{\partial n_s}{\partial t} + \nabla \cdot (n_s \vec{U}_s) = 0, \quad (2.9)$$

$$\begin{aligned} m_s n_s \frac{\partial \vec{U}_s}{\partial t} &= n_s q_s (\vec{E} + \vec{U}_s \times \vec{B}) - k_b T \nabla n_s \\ &\quad - m_s n_s \sum_{\alpha \neq s} \nu_{s\alpha} (\vec{U}_s - \vec{U}_\alpha). \end{aligned} \quad (2.10)$$

This set of equations is used as the basis for the nonlinear PF-FDTD model. However, as will be discussed in later chapters, stability issues with the nonlinear model created the need for a further linearized model.

2.1.2 The Linear Fluid Model

The linear model was developed to increase the stability of the simulations over that of the nonlinear model. Many of the instabilities within the nonlinear model arise from numerical round off. It is a given that round off errors will occur within the field values. However, when these round off errors are multiplied by other round off errors, the insignificant rounding of a number can quickly control the stability of the simulation. This is especially true for the current term in Amperes Law, where the numerically calculated density is multiplied by the numerically calculated velocity. Two other areas of concern are the spatial variation in the continuity equation and the $\vec{U} \times \vec{B}$ in the Lorentz term of

the momentum equation. It is also possible for the density multiplication in the Lorentz force and collision terms in the momentum equation to be susceptible to round off errors. However, the latter can easily be remedied by normalizing the whole momentum equation by the density term, with the resulting division of densities in the ideal gas term actually minimizing the errors effect.

Another side effect of the round off errors is that the large DC biased magnetic field can cause the smaller time varying field to fall within the region of the least significant bit. To minimize this effect, a common linearizing technique can be employed. Common to wave analysis, the idea is to decompose a signal into a large constant (\mathbf{A}_0) and smaller time varying signal (\mathbf{A}_1). The total signal then becomes a linear combination of the two parts,

$$\mathbf{A} = \mathbf{A}_0 + \mathbf{A}_1 . \quad (2.11)$$

The multiplication of two of these signals,

$$\mathbf{AB} = \mathbf{A}_0\mathbf{B}_0 + \mathbf{A}_0\mathbf{B}_1 + \mathbf{A}_1\mathbf{B}_0 + \mathbf{A}_1\mathbf{B}_1 , \quad (2.12)$$

can be approximated as

$$\mathbf{AB} \simeq \mathbf{A}_0\mathbf{B}_0 + \mathbf{A}_0\mathbf{B}_1 + \mathbf{A}_1\mathbf{B}_0 . \quad (2.13)$$

Since the product of second order small terms are smaller then the originals, $\mathbf{A}_1\mathbf{B}_1 \ll \mathbf{A}_0\mathbf{B}_1$, it becomes possible to ignore $\mathbf{A}_1\mathbf{B}_1$.

In so doing, it becomes possible to rewrite the field values, by separating the various fields into a DC term and a small time varying component

$$\vec{E} = \vec{E}_0 + \vec{E}_1 , \quad (2.14)$$

$$\vec{B} = \vec{B}_0 + \vec{B}_1 , \quad (2.15)$$

$$\vec{U}_{xs} = \vec{U}_{0_{xs}} + \vec{U}_{1_{xs}} , \quad (2.16)$$

$$n_s = n_{0_s} + n_{1_s} . \quad (2.17)$$

The constant electric field is assumed to be zero since any constant term will drop from the calculations within Amperes and Faraday equations, while a constant electric field within the Lorentz term of the momentum is inseparable from a drift or constant magnetic field. This separation of fields also helps minimize the errors introduced within the multiplication of field values. Once the field values are separated into constant and small perturbation terms, the fundamental equations (2.7-2.10) become,

$$\nabla \times \vec{E}_1 = -\frac{\partial \vec{B}_1}{\partial t}, \quad (2.18)$$

$$\nabla \times \vec{B}_1 = \epsilon\mu \frac{\partial \vec{E}_1}{\partial t} + \mu \sum_s q_s (n_{0s} \vec{U}_{0s} + n_{1s} \vec{U}_{0s} + n_{0s} \vec{U}_{1s}), \quad (2.19)$$

$$0 = \frac{\partial n_{1s}}{\partial t} + \nabla \cdot (n_{1s} \vec{U}_{0s} + n_{0s} \vec{U}_{1s}), \quad (2.20)$$

$$\begin{aligned} m_s n_{0s} \left(\frac{\partial \vec{U}_{1s}}{\partial t} + (\vec{U}_{0s} \cdot \nabla) \vec{U}_{1s} \right) &= q_s n_{0s} (\vec{E}_1 + \vec{U}_{1s} \times \vec{B}_0 + \vec{U}_{0s} \times \vec{B}_1) \\ &\quad + q_s (n_{0s} + n_{1s}) (\vec{U}_{0s} \times \vec{B}_0) - k_b T \nabla n_{1s} \\ &\quad - m_s (n_{0s} + n_{1s}) \sum_{\alpha \neq s} \nu_{s\alpha} (\vec{U}_{0s} - \vec{U}_{0\alpha}) \\ &\quad - m_s n_{0s} \sum_{\alpha \neq s} \nu_{s\alpha} (\vec{U}_{1s} - \vec{U}_{1\alpha}). \end{aligned} \quad (2.21)$$

where $(\vec{U}_{0s} \cdot \nabla) \vec{U}_{0s}$ was neglected because the background flow is subsonic.

2.2 Discritization

Once the fundamental equations are derived, the next step in developing the model is to discritize the field values. In the case of the PF-FDTD, that means prescribing a physical location and a point in time at which the field values will be known. These spatial and temporal definitions then enable the derivatives of equations 2.7 - 2.10 or 2.18 - 2.21 to be converted into simple differences. For example, the temporal derivative of Faraday's equation can be written as the change of magnetic field from $t - \frac{dt}{2}$ to $t + \frac{dt}{2}$ divided by the time step dt ,

$$\frac{\partial \vec{B}}{\partial t} = \frac{\vec{B}^{t+1/2} - \vec{B}^{t-1/2}}{dt}, \quad (2.22)$$

or the spatial derivative of the pressure term of the momentum equation becomes,

$$\nabla n_{1s} = \hat{x} \frac{\partial n_{1s}}{\partial x} + \hat{y} \frac{\partial n_{1s}}{\partial y} + \hat{z} \frac{\partial n_{1s}}{\partial z} \quad (2.23)$$

$$\begin{aligned} &= \hat{x} \frac{n_{1s}(i+1/2, j, k) - n_{1s}(i-1/2, j, k)}{dx} \\ &\quad + \hat{y} \frac{n_{1s}(i, j+1/2, k) - n_{1s}(i, j-1/2, k)}{dy} \\ &\quad + \hat{z} \frac{n_{1s}(i, j, k+1/2) - n_{1s}(i, j, k-1/2)}{dz}, \end{aligned} \quad (2.24)$$

with the spatial derivative equaling the variation in density from point $i - \frac{dx}{2}$ to $i + \frac{dx}{2}$ divided by the spatial step dx . The same is also true for j/dy and k/dz .

The exact time t and place (i, j, k) of each field calculations is chosen to minimize computational load while maximizing physical meaning. The values of dt , dx , dy , and dz are also chosen to maximize the physical content of the problem at hand.

2.2.1 Spatial Discretization

In defining the spatial location of the various fields; plasma density, velocity, and temperature, as well as the electric and magnetic fields, the introduction of a Yee cell becomes beneficial [45]. Used to relate the physical locations of the field values, the Yee cell aids in discretizing the fundamental equations. Like traditional FDTD techniques the electric and magnetic fields are assigned along the edge of the cell, see fig. 2.1. This placement minimizes the errors introduced in performing the spatial derivatives in Maxwell's equations.

Once the electric and magnetic fields have been spatially specified, the issue then is that in the continuity equations (2.9 or 2.20) and Amperes law (2.8 or 2.19) the velocity and density must occupy the same location as the electric field, to minimize computational averaging. By collocating the velocity with the electric field, a spatial averaging must occur for the Lorentz's term in the momentum equation (2.10 or 2.21). If one locates the density along the cells edge, as has been done by others [43, 44, 46], the physical concept of the plasma within the cell is removed. The combination of required spatial averaging

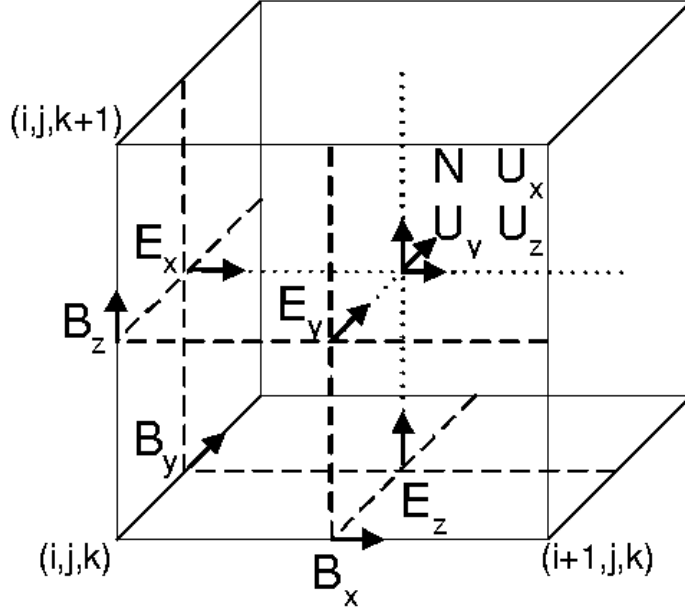


Fig. 2.1: The PF-FDTD Yee cell.

and physical meaning make this an unsatisfactory allocation to implement, in our opinion. If instead, the density is moved to the center of the cell, a concept in line with the idea of a center of mass, a physical meaning can be obtained, see fig. 2.1. Once the density is prescribed, an evaluation of the equations shows that, to minimize the spatial averaging within the equations, the velocity term must be collocated with the density or the electric field, because if the velocity is collocated with the magnetic field, it becomes difficult to develop a physical relationship between the velocity and the density.

Young and Olagangil collocated the velocity with the electric field where it can physically represent the particles that travel from one cell to the neighboring cell [44,46]. However using this technique, twenty-five averages must occur to guarantee that the discretized fields will be known where they are needed. Eighteen associated with the Lorentz force in the momentum equation (2.10 or 2.21), six for the continuity equation (2.9 or 2.20), and one for the current calculation (2.8 or 2.19). The total number may be decreased to seventeen, if the density and temperature are combined into a pressure, similar to Young and Brueckner [43].

Choosing to collocate the velocity with the density implies that the velocity is applied directly to the effective, centrally located, plasma particle. While this maintains a physical

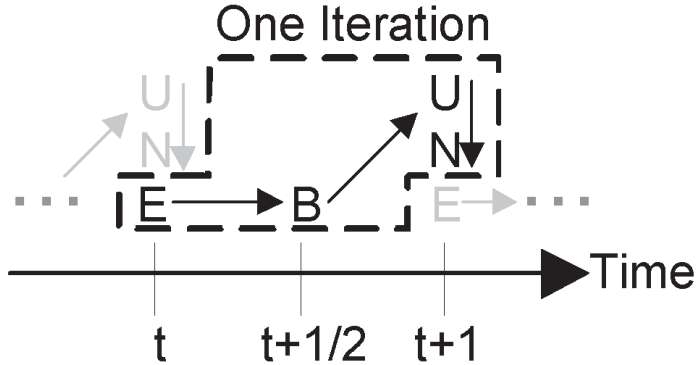


Fig. 2.2: The PF-FDTD leap frog technique.

meaning, it also decreases the total number of averages to twenty-two, without any limiting assumptions. Twenty one for the momentum equation (2.10 or 2.21), zero for the continuity equation (2.9 or 2.20), and one for Amperes equation (2.8 or 2.19). This representation decreases the total computations and maintains a good physical meaning, see fig. 2.1.

2.2.2 Temporal Discretization

The temporal discretization follows a similar process to the spatial discretization of the fields. To minimize the calculations, while taking advantage of the time derivative in Maxwell's equations, the electric and magnetic field values have to alternate half time steps, a technique similar to traditional FDTD models.

When it comes to the temporal location of the density and velocity, once again there are multiple ways of coping with the temporal derivatives. However, the only option without significant limitations, requires the prediction of the plasma state given the current electromagnetic effects, see fig. 2.2. This is both a possibility and a requirement since the velocity must be known at three instances in time for the momentum equations (2.10 or 2.21). The density must then coincide with the velocity, to calculate the spatial component of the continuity equation (2.9 or 2.20), it must also be predicted. The final result is that for any given iteration, the PF-FDTD calculates the electric field, then determines the resulting magnetic field. Once the electromagnetic effects are determined, the plasma effects can be predicted and applied to the electric field during the next iteration.

2.3 PF-FDTD Discrete Equations

With the definition of the fundamental equations and the development of the spatial and temporal discretizations, it becomes possible to derive the FDTD set of equations.

2.3.1 Nonlinear Equations

The component form of the nonlinear model is found from 2.7 through 2.10. In their vector components, Maxwell's equations become,

$$\epsilon_0 \mu_0 \frac{\partial E_x}{\partial t} = \frac{\partial B_z}{\partial y} - \frac{\partial B_y}{\partial z} - \mu_0 \sum_s q_s n_s U_{x_s}, \quad (2.25)$$

$$\epsilon_0 \mu_0 \frac{\partial E_y}{\partial t} = \frac{\partial B_x}{\partial z} - \frac{\partial B_z}{\partial x} - \mu_0 \sum_s q_s n_s U_{y_s}, \quad (2.26)$$

$$\epsilon_0 \mu_0 \frac{\partial E_z}{\partial t} = \frac{\partial B_y}{\partial x} - \frac{\partial B_x}{\partial y} - \mu_0 \sum_s q_s n_s U_{z_s}, \quad (2.27)$$

and

$$\frac{\partial B_x}{\partial t} = \frac{\partial E_y}{\partial z} - \frac{\partial E_z}{\partial y}, \quad (2.28)$$

$$\frac{\partial B_y}{\partial t} = \frac{\partial E_z}{\partial x} - \frac{\partial E_x}{\partial z}, \quad (2.29)$$

$$\frac{\partial B_z}{\partial t} = \frac{\partial E_x}{\partial y} - \frac{\partial E_y}{\partial x}. \quad (2.30)$$

Each species, s , also gets its own set of continuity equation,

$$\frac{\partial n_s}{\partial t} + \frac{\partial(n_s U_{x_s})}{\partial x} + \frac{\partial(n_s U_{y_s})}{\partial y} + \frac{\partial(n_s U_{z_s})}{\partial z} = 0, \quad (2.31)$$

and momentum equations,

$$m_s n_s \frac{\partial U_{x_s}}{\partial t} = n_s q_s (E_x + U_{y_s} B_z - U_{z_s} B_y) - k_b T \frac{\partial n_s}{\partial x} - n_s m_s \sum_{\alpha \neq s} \nu_{s\alpha} (U_{x_s} - U_{x_\alpha}), \quad (2.32)$$

$$m_s n_s \frac{\partial U_{y_s}}{\partial t} = n_s q_s (E_y + U_{z_s} B_x - U_{x_s} B_z) - k_b T \frac{\partial n_s}{\partial y} - n_s m_s \sum_{\alpha \neq s} \nu_{s\alpha} (U_{y_s} - U_{y_\alpha}), \quad (2.33)$$

$$m_s n_s \frac{\partial U_{z_s}}{\partial t} = n_s q_s (E_z + U_{x_s} B_y - U_{y_s} B_x) - k_b T \frac{\partial n_s}{\partial z} - n_s m_s \sum_{\alpha \neq s} \nu_{s\alpha} (U_{z_s} - U_{z_\alpha}). \quad (2.34)$$

When the PF-FDTD cell (fig. 2.1) and the time increments (fig. 2.2) are applied to Maxwell's equations (2.25-2.30), they can be rewritten in the discrete form,

$$\begin{aligned} E_x^t(i, j, k) = & E_x^{t-1}(i, j, k) + \frac{dt}{\epsilon_0 \mu_0} \left[\frac{B_z^{t-1/2}(i, j + 1/2, k) - B_z^{t-1/2}(i, j - 1/2, k)}{dy} \right. \\ & \left. - \frac{B_y^{t-1/2}(i, j, k + 1/2) - B_y^{t-1/2}(i, j, k - 1/2)}{dz} \right. \\ & \left. - \mu_0 \sum_s q_s \frac{n_s^t(i, j, k) U_{x_s}^t(i, j, k) + n_s^t(i - 1, j, k) U_{x_s}^t(i - 1, j, k)}{2} \right], \end{aligned} \quad (2.35)$$

$$\begin{aligned} E_y^t(i, j, k) = & E_y^{t-1}(i, j, k) + \frac{dt}{\epsilon_0 \mu_0} \left[\frac{B_x^{t-1/2}(i, j, k + 1/2) - B_x^{t-1/2}(i, j, k - 1/2)}{dz} \right. \\ & \left. - \frac{B_z^{t-1/2}(i + 1/2, j, k) - B_z^{t-1/2}(i - 1/2, j, k)}{dx} \right. \\ & \left. - \mu_0 \sum_s q_s \frac{n_s^t(i, j, k) U_{y_s}^t(i, j, k) + n_s^t(i, j - 1, k) U_{y_s}^t(i, j - 1, k)}{2} \right], \end{aligned} \quad (2.36)$$

$$\begin{aligned} E_z^t(i, j, k) = & E_z^{t-1}(i, j, k) + \frac{dt}{\epsilon_0 \mu_0} \left[\frac{B_y^{t-1/2}(i + 1/2, j, k) - B_y^{t-1/2}(i - 1/2, j, k)}{dx} \right. \\ & \left. - \frac{B_x^{t-1/2}(i, j + 1/2, k) - B_x^{t-1/2}(i, j - 1/2, k)}{dy} \right. \\ & \left. - \mu_0 \sum_s q_s \frac{n_s^t(i, j, k) U_{z_s}^t(i, j, k) + n_s^t(i, j, k - 1) U_{z_s}^t(i, j, k - 1)}{2} \right], \end{aligned} \quad (2.37)$$

and

$$\begin{aligned} B_x^{t+1/2}(i, j, k) = & B_x^{t-1/2}(i, j, k) + dt \left[\frac{E_y^t(i, j, k + 1/2) - E_y^t(i, j, k - 1/2)}{dz} \right. \\ & \left. - \frac{E_z^t(i, j + 1/2, k) - E_z^t(i, j - 1/2, k)}{dy} \right], \end{aligned} \quad (2.38)$$

$$B_y^{t+1/2}(i, j, k) = B_y^{t-1/2}(i, j, k) + dt \left[\frac{E_z^t(i + 1/2, j, k) - E_z^t(i - 1/2, j, k)}{dx} \right]$$

$$-\left. \frac{E_x^t(i, j, k + 1/2) - E_x^t(i, j, k - 1/2)}{dz} \right] , \quad (2.39)$$

$$\begin{aligned} B_z^{t+1/2}(i, j, k) = & B_z^{t-1/2}(i, j, k) + dt \left[\frac{E_x^t(i, j + 1/2, k) - E_x^t(i, j - 1/2, k)}{dy} \right. \\ & \left. - \frac{E_y^t(i + 1/2, j, k) - E_y^t(i - 1/2, j, k)}{dx} \right] . \end{aligned} \quad (2.40)$$

The momentum equation (2.32) can be converted into the following form,

$$\begin{aligned} m_s n_s^t(i, j, k) \left(\frac{U_{x_s}^{t+1}(i, j, k) - U_{x_s}^{t-1}(i, j, k)}{2dt} \right) = & q_s n_s^t(i, j, k) \left[\frac{E_x^t(i, j, k) + E_x^t(i + 1, j, k)}{2} \right. \\ & + U_{y_s}^t(i, j, k) \left(\frac{B_z^{t+1/2}(i, j, k) + B_z^{t+1/2}(i + 1, j, k) + B_z^{t+1/2}(i, j + 1, k) + B_z^{t+1/2}(i + 1, j + 1, k)}{8} \right. \\ & \left. + \frac{B_z^{t-1/2}(i, j, k) + B_z^{t-1/2}(i + 1, j, k) + B_z^{t-1/2}(i, j + 1, k) + B_z^{t-1/2}(i + 1, j + 1, k)}{8} \right) \\ & - U_{z_s}^t(i, j, k) \left(\frac{B_y^{t+1/2}(i, j, k) + B_y^{t+1/2}(i + 1, j, k) + B_y^{t+1/2}(i, j + 1, k) + B_y^{t+1/2}(i + 1, j + 1, k)}{8} \right. \\ & \left. + \frac{B_y^{t-1/2}(i, j, k) + B_y^{t-1/2}(i + 1, j, k) + B_y^{t-1/2}(i, j + 1, k) + B_y^{t-1/2}(i + 1, j + 1, k)}{8} \right) \right] \\ & - k_b T \frac{n_s^t(i + 1, j, k) - n_s^t(i - 1, j, k)}{2dx} - m_s n_s^t(i, j, k) \sum_{\alpha \neq s} \nu_{s\alpha} (U_{x_s}^t(i, j, k) - U_{x_\alpha}^t(i, j, k)) , \end{aligned} \quad (2.41)$$

with similar equations derived from equations 2.33 and 2.34. It should be pointed out at this time, that the temporal derivative of the velocity \vec{U} occurs over two time steps, as opposed to the single time step of Maxwell's equations. This enables the temporal derivative to be calculated at the same time that the current state of the velocity is used in the Lorentz and collision terms. These equations can then be solved for the future velocity,

$$\begin{aligned} U_{x_s}^{t+1}(i, j, k) = & U_{x_s}^{t-1}(i, j, k) + \frac{q_s dt}{m_s} \left[E_x^t(i, j, k) + E_x^t(i + 1, j, k) \right. \\ & + U_{y_s}^t(i, j, k) \left(\frac{B_z^{t+1/2}(i, j, k) + B_z^{t+1/2}(i + 1, j, k) + B_z^{t+1/2}(i, j + 1, k) + B_z^{t+1/2}(i + 1, j + 1, k)}{4} \right. \\ & \left. + \frac{B_z^{t-1/2}(i, j, k) + B_z^{t-1/2}(i + 1, j, k) + B_z^{t-1/2}(i, j + 1, k) + B_z^{t-1/2}(i + 1, j + 1, k)}{4} \right) \\ & - U_{z_s}^t(i, j, k) \left(\frac{B_y^{t+1/2}(i, j, k) + B_y^{t+1/2}(i + 1, j, k) + B_y^{t+1/2}(i, j + 1, k) + B_y^{t+1/2}(i + 1, j + 1, k)}{4} \right. \\ & \left. + \frac{B_y^{t-1/2}(i, j, k) + B_y^{t-1/2}(i + 1, j, k) + B_y^{t-1/2}(i, j + 1, k) + B_y^{t-1/2}(i + 1, j + 1, k)}{4} \right) \right] \end{aligned}$$

$$\begin{aligned}
& -\frac{k_b T dt}{m_s} \frac{n_s^t(i+1,j,k) - n_s^t(i-1,j,k)}{n_s^t(i,j,k) dx} \\
& -2dt \sum_{\alpha \neq s} \nu_{s\alpha} (U_{x_\alpha}^t(i,j,k) - U_{x_\alpha}^t(i,j,k)) , \tag{2.42}
\end{aligned}$$

$$\begin{aligned}
U_{y_s}^{t+1}(i,j,k) &= U_{y_s}^{t-1}(i,j,k) + \frac{q_s dt}{m_s} \left[E_y^t(i,j,k) + E_y^t(i,j+1,k) \right. \\
&\quad + U_{z_s}^t(i,j,k) \left(\frac{B_x^{t+1/2}(i,j,k) + B_x^{t+1/2}(i,j+1,k) + B_x^{t+1/2}(i,j,k+1) + B_x^{t+1/2}(i,j+1,k+1)}{4} \right. \\
&\quad \left. + \frac{B_x^{t-1/2}(i,j,k) + B_x^{t-1/2}(i,j+1,k) + B_x^{t-1/2}(i,j,k+1) + B_x^{t-1/2}(i,j+1,k+1)}{4} \right) \\
&\quad - U_{x_s}^t(i,j,k) \left(\frac{B_z^{t+1/2}(i,j,k) + B_z^{t+1/2}(i+1,j,k) + B_z^{t+1/2}(i,j+1,k) + B_z^{t+1/2}(i+1,j+1,k)}{4} \right. \\
&\quad \left. + \frac{B_z^{t-1/2}(i,j,k) + B_z^{t-1/2}(i+1,j,k) + B_z^{t-1/2}(i,j+1,k) + B_z^{t-1/2}(i+1,j+1,k)}{4} \right) \left. \right] \\
&\quad - \frac{k_b T dt}{m_s} \frac{n_s^t(i,j+1,k) - n_s^t(i,j-1,k)}{n_s^t(i,j,k) dy} \\
&\quad -2dt \sum_{\alpha \neq s} \nu_{s\alpha} (U_{y_\alpha}^t(i,j,k) - U_{y_\alpha}^t(i,j,k)) , \tag{2.43}
\end{aligned}$$

$$\begin{aligned}
U_{z_s}^{t+1}(i,j,k) &= U_{z_s}^{t-1}(i,j,k) + \frac{q_s dt}{m_s} \left[E_z^t(i,j,k) + E_z^t(i,j,k+1) \right. \\
&\quad + U_{x_s}^t(i,j,k) \left(\frac{B_y^{t+1/2}(i,j,k) + B_y^{t+1/2}(i+1,j,k) + B_y^{t+1/2}(i,j,k+1) + B_y^{t+1/2}(i+1,j,k+1)}{4} \right. \\
&\quad \left. + \frac{B_y^{t-1/2}(i,j,k) + B_y^{t-1/2}(i+1,j,k) + B_y^{t-1/2}(i,j,k+1) + B_y^{t-1/2}(i+1,j,k+1)}{4} \right) \\
&\quad - U_{y_s}^t(i,j,k) \left(\frac{B_x^{t+1/2}(i,j,k) + B_x^{t+1/2}(i,j+1,k) + B_x^{t+1/2}(i,j,k+1) + B_x^{t+1/2}(i,j+1,k+1)}{4} \right. \\
&\quad \left. + \frac{B_x^{t-1/2}(i,j,k) + B_x^{t-1/2}(i,j+1,k) + B_x^{t-1/2}(i,j,k+1) + B_x^{t-1/2}(i,j+1,k+1)}{4} \right) \left. \right] \\
&\quad - \frac{k_b T dt}{m_s} \frac{n_s^t(i,j,k+1) - n_s^t(i,j,k-1)}{n_s^t(i,j,k) dz} \\
&\quad -2dt \sum_{\alpha \neq s} \nu_{s\alpha} (U_{z_\alpha}^t(i,j,k) - U_{z_\alpha}^t(i,j,k)) . \tag{2.44}
\end{aligned}$$

Applying the FD techniques to the continuity equation (2.31), with the temporal derivative occurring over two time steps similar to the momentum equation 2.41, yields,

$$\begin{aligned} & \frac{n_s^{t+1}(i, j, k) - n_s^{t-1}(i, j, k)}{2dt} + n_s^t(i, j, k) \frac{Ux_s^t(i+1, j, k) - Ux_s^t(i-1, j, k)}{2dx} \\ & + U_{x_s}^t(i, j, k) \frac{n_s^t(i+1, j, k) - n_s^t(i-1, j, k)}{2dx} + n_s^t(i, j, k) \frac{Uy_s^t(i, j+1, k) - Uy_s^t(i, j-1, k)}{2dy} \\ & + U_{y_s}^t(i, j, k) \frac{n_s^t(i, j+1, k) - n_s^t(i, j-1, k)}{2dy} + n_s^t(i, j, k) \frac{Uz_s^t(i, j, k+1) - Uz_s^t(i, j, k-1)}{2dz} \\ & + U_{z_s}^t(i, j, k) \frac{n_s^t(i, j, k+1) - n_s^t(i, j, k-1)}{2dz} = 0 . \quad (2.45) \end{aligned}$$

This can then be solved for the future density,

$$\begin{aligned} n_s^{t+1}(i, j, k) &= n_s^{t-1}(i, j, k) - dt \left[\begin{aligned} & n_s^t(i, j, k) \left(\frac{Ux_s^t(i+1, j, k) - Ux_s^t(i-1, j, k)}{dx} \right. \right. \\ & + \frac{Uy_s^t(i, j+1, k) - Uy_s^t(i, j-1, k)}{dy} \\ & \left. \left. + \frac{Uz_s^t(i, j, k+1) - Uz_s^t(i, j, k-1)}{dz} \right) \right. \\ & + U_{x_s}^t(i, j, k) \frac{n_s^t(i+1, j, k) - n_s^t(i-1, j, k)}{dx} \\ & + U_{y_s}^t(i, j, k) \frac{n_s^t(i, j+1, k) - n_s^t(i, j-1, k)}{dy} \\ & \left. \left. + U_{z_s}^t(i, j, k) \frac{n_s^t(i, j, k+1) - n_s^t(i, j, k-1)}{dz} \right] , \right. \quad (2.46) \end{aligned}$$

completing the final set of equations.

These equations (2.35-2.40, 2.42-2.44, and 2.46) once coded, can then be used to model any geometric probe submersed in any incompressible isotropically warm collisional magnetized multi-species plasma, assuming one can find enough memory and computational power.

2.3.2 Linear Equations

The derivation of the linear set of equations follows the same procedure as the nonlinear set. Equations 2.18 through 2.21 can be divided up into their vector form, with the temporal

and spatial derivative of the constant component equal to zero (i.e. $\frac{\partial E_{0x}}{\partial t} = 0, \frac{\partial B_{0z}}{\partial y} = 0$).

With this in mind, Maxwell's equations become,

$$\epsilon_0 \mu_0 \frac{\partial E_{1x}}{\partial t} = \frac{\partial B_{1z}}{\partial y} - \frac{\partial B_{1y}}{\partial z} - \mu_0 \sum_s q_s (n_{0s} U_{1xs} + n_{1s} U_{0xs} + n_{0s} U_{0xs}) , \quad (2.47)$$

$$\epsilon_0 \mu_0 \frac{\partial E_{1y}}{\partial t} = \frac{\partial B_{1x}}{\partial z} - \frac{\partial B_{1z}}{\partial x} - \mu_0 \sum_s q_s (n_{0s} U_{1ys} + n_{1s} U_{0ys} + n_{0s} U_{0ys}) , \quad (2.48)$$

$$\epsilon_0 \mu_0 \frac{\partial E_{1z}}{\partial t} = \frac{\partial B_{1y}}{\partial x} - \frac{\partial B_{1x}}{\partial y} - \mu_0 \sum_s q_s (n_{0s} U_{1zs} + n_{1s} U_{0zs} + n_{0s} U_{0zs}) , \quad (2.49)$$

and

$$\frac{\partial B_{1x}}{\partial t} = \frac{\partial E_{1y}}{\partial z} - \frac{\partial E_{1z}}{\partial y} , \quad (2.50)$$

$$\frac{\partial B_{1y}}{\partial t} = \frac{\partial E_{1z}}{\partial x} - \frac{\partial E_{1x}}{\partial z} , \quad (2.51)$$

$$\frac{\partial B_{1z}}{\partial t} = \frac{\partial E_{1x}}{\partial y} - \frac{\partial E_{1y}}{\partial x} . \quad (2.52)$$

Each species, s , also gets its own set of continuity equation, with the chain rule expanding the spatial derivatives of equation 2.31 with respect to the density and velocity,

$$\frac{\partial n_s}{\partial t} + n_{0s} \left(\frac{\partial U_{1xs}}{\partial x} + \frac{\partial U_{1ys}}{\partial y} + \frac{\partial U_{1zs}}{\partial z} \right) + U_{0xs} \frac{\partial n_{1s}}{\partial x} + U_{0ys} \frac{\partial n_{1s}}{\partial y} + U_{0zs} \frac{\partial n_{1s}}{\partial z} = 0 . \quad (2.53)$$

A similar process can also be applied to the momentum equation,

$$\begin{aligned} m_s n_{0s} \left(\frac{\partial U_{1xs}}{\partial t} + U_{0xs} \frac{\partial U_{1xs}}{\partial x} \right) &= q_s n_{0s} (E_{1x} + U_{0ys} B_{1z} - U_{0zs} B_{1y} + U_{1ys} B_{0z} - U_{1zs} B_{0y}) \\ &\quad + q_s (n_{0s} + n_{1s}) (U_{0ys} B_{0z} - U_{0zs} B_{0y}) - k_b T \frac{\partial n_{1s}}{\partial x} \\ &\quad - m_s (n_{0s} + n_{1s}) \sum_{\alpha \neq s} \nu_{s\alpha} (U_{0xs} - U_{0x\alpha}) \\ &\quad - m_s n_{0s} \sum_{\alpha \neq s} \nu_{s\alpha} (U_{1xs} - U_{1x\alpha}) , \end{aligned} \quad (2.54)$$

$$\begin{aligned} m_s n_{0s} \left(\frac{\partial U_{1ys}}{\partial t} + U_{0ys} \frac{\partial U_{1ys}}{\partial y} \right) &= q_s n_{0s} (E_{1y} + U_{0zs} B_{1x} - U_{0xs} B_{1z} + U_{1zs} B_{0x} - U_{1xs} B_{0z}) \\ &\quad + q_s (n_{0s} + n_{1s}) (U_{0zs} B_{0x} - U_{0xs} B_{0z}) - k_b T \frac{\partial n_{1s}}{\partial y} \end{aligned}$$

$$\begin{aligned}
& -m_s(n_{0_s} + n_{1_s}) \sum_{\alpha \neq s} \nu_{s\alpha}(U_{0_{ys}} - U_{0_{y\alpha}}) \\
& -m_s n_{0_s} \sum_{\alpha \neq s} \nu_{s\alpha}(U_{1_{ys}} - U_{1_{y\alpha}}) , \tag{2.55}
\end{aligned}$$

$$\begin{aligned}
m_s n_{0_s} \left(\frac{\partial U_{1_{zs}}}{\partial t} + U_{0_{zs}} \frac{\partial U_{1_{zs}}}{\partial z} \right) &= q_s n_{0_s} (E_{1z} + U_{0_{xs}} B_{1y} - U_{0_{ys}} B_{1x} + U_{1_{xs}} B_{0y} - U_{1_{ys}} B_{0x}) \\
&\quad + q_s (n_{0_s} + n_{1_s})(U_{0_{xs}} B_{0y} - U_{0_{ys}} B_{0x}) - k_b T \frac{\partial n_{1_s}}{\partial z} \\
&\quad - m_s (n_{0_s} + n_{1_s}) \sum_{\alpha \neq s} \nu_{s\alpha}(U_{0_{zs}} - U_{0_{z\alpha}}) \\
&\quad - m_s n_{0_s} \sum_{\alpha \neq s} \nu_{s\alpha}(U_{1_{zs}} - U_{1_{z\alpha}}) . \tag{2.56}
\end{aligned}$$

These equations (2.47-2.56) can then be discretized using the PF-FDTD cell (fig. 2.1) and the time increments (fig. 2.2) to get,

$$\begin{aligned}
E_{1_x}^t(i, j, k) &= E_{1_x}^{t-1}(i, j, k) + \frac{dt}{\epsilon_0 \mu_0} \left[\frac{B_{1_z}^{t-1/2}(i, j + 1/2, k) - B_{1_z}^{t-1/2}(i, j - 1/2, k)}{dy} \right. \\
&\quad \left. - \frac{B_{1_y}^{t-1/2}(i, j, k + 1/2) - B_{1_y}^{t-1/2}(i, j, k - 1/2)}{dz} \right. \\
&\quad - \mu_0 \sum_s q_s \left(n_{0_s} \frac{U_{1_{xs}}^t(i, j, k) + U_{1_{xs}}^t(i - 1, j, k)}{2} \right. \\
&\quad \left. + U_{0_{xs}} \frac{n_{1_s}^t(i, j, k) + n_{1_s}^t(i - 1, j, k)}{2} \right. \\
&\quad \left. + n_{0_s} U_{0_{xs}} \right) \right] , \tag{2.57}
\end{aligned}$$

$$\begin{aligned}
E_{1_y}^t(i, j, k) &= E_{1_y}^{t-1}(i, j, k) + \frac{dt}{\epsilon_0 \mu_0} \left[\frac{B_{1_x}^{t-1/2}(i, j, k + 1/2) - B_{1_x}^{t-1/2}(i, j, k - 1/2)}{dz} \right. \\
&\quad \left. - \frac{B_{1_z}^{t-1/2}(i + 1/2, j, k) - B_{1_z}^{t-1/2}(i - 1/2, j, k)}{dx} \right. \\
&\quad - \mu_0 \sum_s q_s \left(n_{0_s} \frac{U_{1_{ys}}^t(i, j, k) + U_{1_{ys}}^t(i, j - 1, k)}{2} \right. \\
&\quad \left. + U_{0_{ys}} \frac{n_{1_s}^t(i, j, k) + n_{1_s}^t(i, j - 1, k)}{2} \right. \\
&\quad \left. + n_{0_s} U_{0_{ys}} \right) \right] , \tag{2.58}
\end{aligned}$$

$$\begin{aligned}
E_{1_z}^t(i, j, k) = & E_{1_z}^{t-1}(i, j, k) + \frac{dt}{\epsilon_0 \mu_0} \left[\frac{B_{1_y}^{t-1/2}(i+1/2, j, k) - B_{1_y}^{t-1/2}(i-1/2, j, k)}{dx} \right. \\
& - \frac{B_{1_x}^{t-1/2}(i, j+1/2, k) - B_{1_x}^{t-1/2}(i, j-1/2, k)}{dy} \\
& - \mu_0 \sum_s q_s \left(n_{0_s} \frac{U_{1_{zs}}^t(i, j, k) + U_{1_{zs}}^t(i, j, k-1)}{2} \right. \\
& \quad \left. \left. + U_{0_{zs}} \frac{n_{1_s}^t(i, j, k) + n_{1_s}^t(i, j, k-1)}{2} \right. \right. \\
& \quad \left. \left. + n_{0_s} U_{0_{zs}} \right) \right], \tag{2.59}
\end{aligned}$$

$$\begin{aligned}
B_{1_x}^{t+1/2}(i, j, k) = & B_{1_x}^{t-1/2}(i, j, k) + dt \left[\frac{E_{1_y}^t(i, j, k+1/2) - E_{1_y}^t(i, j, k-1/2)}{dz} \right. \\
& \left. - \frac{E_{1_z}^t(i, j+1/2, k) - E_{1_z}^t(i, j-1/2, k)}{dy} \right], \tag{2.60}
\end{aligned}$$

$$\begin{aligned}
B_{1_y}^{t+1/2}(i, j, k) = & B_{1_y}^{t-1/2}(i, j, k) + dt \left[\frac{E_{1_z}^t(i+1/2, j, k) - E_{1_z}^t(i-1/2, j, k)}{dx} \right. \\
& \left. - \frac{E_{1_x}^t(i, j, k+1/2) - E_{1_x}^t(i, j, k-1/2)}{dz} \right], \tag{2.61}
\end{aligned}$$

$$\begin{aligned}
B_{1_z}^{t+1/2}(i, j, k) = & B_{1_z}^{t-1/2}(i, j, k) + dt \left[\frac{E_{1_x}^t(i, j+1/2, k) - E_{1_x}^t(i, j-1/2, k)}{dy} \right. \\
& \left. - \frac{E_{1_y}^t(i+1/2, j, k) - E_{1_y}^t(i-1/2, j, k)}{dx} \right], \tag{2.62}
\end{aligned}$$

$$\begin{aligned}
n_{1_s}^{t+1}(i, j, k) = & n_{1_s}^{t-1}(i, j, k) - dt \left[n_{0_s} \left(\frac{U_{1_{x0}}^t(i+1, j, k) - U_{1_{xs}}^t(i-1, j, k)}{dx} \right. \right. \\
& \quad \left. \left. + \frac{U_{1_{ys}}^t(i, j+1, k) - U_{1_{ys}}^t(i, j-1, k)}{dy} \right. \right. \\
& \quad \left. \left. + \frac{U_{1_{zs}}^t(i, j, k+1) - U_{1_{zs}}^t(i, j, k-1)}{dz} \right) \right]
\end{aligned}$$

$$\begin{aligned}
& + U_{0_{xs}} \frac{n_{1s}^t(i+1,j,k) - n_{1s}^t(i-1,j,k)}{dx} \\
& + U_{0_{ys}} \frac{n_{1s}^t(i,j+1,k) - n_{1s}^t(i,j-1,k)}{dy} \\
& + U_{0_{zs}} \frac{n_{1s}^t(i,j,k+1) - n_{1s}^{t_1}(i,j,k-1)}{dz} \Big] ,
\end{aligned} \tag{2.63}$$

$$\begin{aligned}
U_{1_{xs}}^{t+1}(i,j,k) = & U_{1_{xs}}^{t-1}(i,j,k) - dt U_{0_{xs}} \frac{U_{1_{xs}}^t(i+1,j,k) - U_{1_{xs}}^t(i-1,j,k)}{dx} \\
& + \frac{q_s dt}{m_s} \left[E_{1_x}^t(i,j,k) + E_{1_x}^t(i+1,j,k) \right. \\
& + U_{0_{ys}} \left(\frac{B_{1z}^{t+1/2}(i,j,k) + B_{1z}^{t+1/2}(i+1,j,k) + B_{1z}^{t+1/2}(i,j+1,k) + B_{1z}^{t+1/2}(i+1,j+1,k)}{4} \right. \\
& \quad \left. + \frac{B_{1z}^{t-1/2}(i,j,k) + B_{1z}^{t-1/2}(i+1,j,k) + B_{1z}^{t-1/2}(i,j+1,k) + B_{1z}^{t-1/2}(i+1,j+1,k)}{4} \right) \\
& - U_{0_{zs}} \left(\frac{B_{1y}^{t+1/2}(i,j,k) + B_{1y}^{t+1/2}(i+1,j,k) + B_{1y}^{t+1/2}(i,j,k+1) + B_{1y}^{t+1/2}(i+1,j,k+1)}{4} \right. \\
& \quad \left. + \frac{B_{1y}^{t-1/2}(i,j,k) + B_{1y}^{t-1/2}(i+1,j,k) + B_{1y}^{t-1/2}(i,j,k+1) + B_{1y}^{t-1/2}(i+1,j,k+1)}{4} \right) \\
& \quad \left. + 2U_{1_{ys}}^t(i,j,k)B_{0z} - 2U_{1_{zs}}^t(i,j,k)B_{0y} \right] \\
& + \frac{2q_s dt}{m_s} \left(1 + \frac{n_{1s}^t(i,j,k)}{n_{0s}} \right) \left(U_{0_{ys}} B_{0z} - U_{0_{zs}} B_{0y} \right) \\
& - \frac{k_b T dt}{m_s n_{0s}} \frac{n_{1s}^t(i+1,j,k) - n_{1s}^t(i-1,j,k)}{dx} \\
& - 2dt \left(1 + \frac{n_{1s}^t(i,j,k)}{n_{0s}} \right) \sum_{\alpha \neq s} \nu_{s\alpha} (U_{0_{xs}} - U_{0_{x\alpha}}) \\
& - 2dt \sum_{\alpha \neq s} \nu_{s\alpha} (U_{1_{xs}}^t(i,j,k) - U_{1_{x\alpha}}^t(i,j,k)) ,
\end{aligned} \tag{2.64}$$

$$\begin{aligned}
U_{1_{ys}}^{t+1}(i,j,k) = & U_{1_{ys}}^{t-1}(i,j,k) - dt U_{0_{ys}} \frac{U_{1_{ys}}^t(i,j+1,k) - U_{1_{ys}}^t(i,j-1,k)}{dy} \\
& + \frac{q_s dt}{m_s} \left[E_{1_y}^t(i,j,k) + E_{1_y}^t(i,j+1,k) \right]
\end{aligned}$$

$$\begin{aligned}
& + U_{0_{zs}} \left(\frac{B_{1x}^{t+1/2}(i,j,k) + B_{1x}^{t+1/2}(i,j+1,k) + B_{1x}^{t+1/2}(i,j,k+1) + B_{1x}^{t+1/2}(i,j+1,k+1)}{4} \right. \\
& \quad + \frac{B_{1x}^{t-1/2}(i,j,k) + B_{1x}^{t-1/2}(i,j+1,k) + B_{1x}^{t-1/2}(i,j,k+1) + B_{1x}^{t-1/2}(i,j+1,k+1)}{4} \Big) \\
& - U_{0_{xs}} \left(\frac{B_{1z}^{t+1/2}(i,j,k) + B_{1z}^{t+1/2}(i+1,j,k) + B_{1z}^{t+1/2}(i,j+1,k) + B_{1z}^{t+1/2}(i+1,j+1,k)}{4} \right. \\
& \quad + \frac{B_{1z}^{t-1/2}(i,j,k) + B_{1z}^{t-1/2}(i+1,j,k) + B_{1z}^{t-1/2}(i,j+1,k) + B_{1z}^{t-1/2}(i+1,j+1,k)}{4} \Big) \\
& \quad \left. + 2U_{1_{zs}}^t(i,j,k)B_{0_x} - 2U_{1_{xs}}^t(i,j,k)B_{0_z} \right] \\
& + \frac{2q_s dt}{m_s} \left(1 + \frac{n_{1s}^t(i,j,k)}{n_{0s}} \right) \left(U_{0_{zs}} B_{0_x} - U_{0_{xs}} B_{0_z} \right) \\
& - \frac{k_b T dt}{m_s n_{0s}} \frac{n_{1s}^t(i,j+1,k) - n_{1s}^t(i,j-1,k)}{dy} \\
& - 2dt \left(1 + \frac{n_{1s}^t(i,j,k)}{n_{0s}} \right) \sum_{\alpha \neq s} \nu_{s\alpha} \left(U_{0_{ys}} - U_{0_{y\alpha}} \right) \\
& - 2dt \sum_{\alpha \neq s} \nu_{s\alpha} \left(U_{1_{ys}}^t(i,j,k) - U_{1_{y\alpha}}^t(i,j,k) \right), \tag{2.65}
\end{aligned}$$

$$\begin{aligned}
U_{1_{zs}}^{t+1}(i,j,k) &= U_{1_{zs}}^{t-1}(i,j,k) - dt U_{0_{zs}} \frac{U_{1_{zs}}^t(i,j,k+1) - U_{1_{zs}}^t(i,j,k-1)}{dz} \\
& + \frac{q_s dt}{m_s} \left[E_{1z}^t(i,j,k) + E_{1z}^t(i,j,k+1) \right. \\
& \quad + U_{0_{xs}} \left(\frac{B_{1y}^{t+1/2}(i,j,k) + B_{1y}^{t+1/2}(i+1,j,k) + B_{1y}^{t+1/2}(i,j,k+1) + B_{1y}^{t+1/2}(i+1,j,k+1)}{4} \right. \\
& \quad \left. + \frac{B_{1y}^{t-1/2}(i,j,k) + B_{1y}^{t-1/2}(i+1,j,k) + B_{1y}^{t-1/2}(i,j,k+1) + B_{1y}^{t-1/2}(i+1,j,k+1)}{4} \right) \\
& \quad - U_{0_{ys}} \left(\frac{B_{1x}^{t+1/2}(i,j,k) + B_{1x}^{t+1/2}(i,j+1,k) + B_{1x}^{t+1/2}(i,j,k+1) + B_{1x}^{t+1/2}(i,j+1,k+1)}{4} \right. \\
& \quad \left. + \frac{B_{1x}^{t-1/2}(i,j,k) + B_{1x}^{t-1/2}(i,j+1,k) + B_{1x}^{t-1/2}(i,j,k+1) + B_{1x}^{t-1/2}(i,j+1,k+1)}{4} \right) \\
& \quad \left. + 2U_{1_{xs}}^t(i,j,k)B_{0_y} - 2U_{1_{ys}}^t(i,j,k)B_{0_x} \right] \\
& + \frac{2q_s dt}{m_s} \left(1 + \frac{n_{1s}^t(i,j,k)}{n_{0s}} \right) \left(U_{0_{xs}} B_{0_y} - U_{0_{ys}} B_{0_x} \right) \\
& - \frac{k_b T dt}{m_s n_{0s}} \frac{n_{1s}^t(i,j,k+1) - n_{1s}^t(i,j,k-1)}{dz} \\
& - 2dt \left(1 + \frac{n_{1s}^t(i,j,k)}{n_{0s}} \right) \sum_{\alpha \neq s} \nu_{s\alpha} \left(U_{0_{zs}} - U_{0_{z\alpha}} \right) \tag{2.66}
\end{aligned}$$

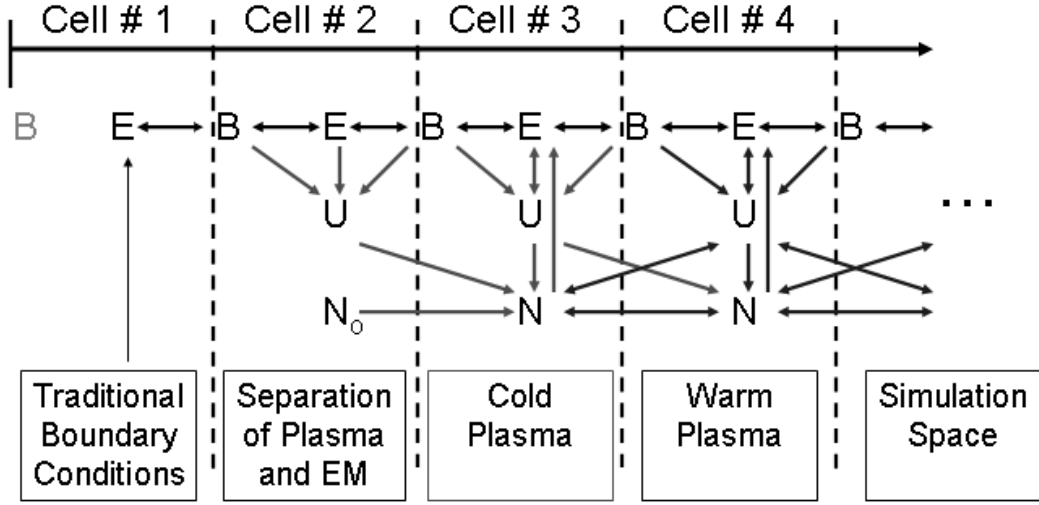


Fig. 2.3: Interdependency of fields for different spatial locations near the PF-FDTD boundary.

$$-2dt \sum_{\alpha \neq s} \nu_{s\alpha} \left(U_{1z_s}^t(i, j, k) - U_{1z_\alpha}^t(i, j, k) \right) ,$$

with the temporal derivative in the continuity and momentum equations occurring over two time steps, similar to the nonlinear case.

2.4 Boundary Condition

Numerical codes and models are used to simulate a near infinite space within the confines of the limited computational memory. However in the case of the PF-FDTD model, the various modes of propagation complicate traditional EM boundary conditions (BC). The problem is that most of the BC applied to EM FDTD models are incapable of multiple modes of propagation. In order to resolve this problem, a technique similar to the effective BC applied to the free space magnetic field is developed. In that if a ideal BC is applied to the electric field, the spatial derivative of Faraday's law effectively applies the ideal BC to the magnetic field, see fig. 2.3.

EM models traditionally apply one of three boundary conditions (BC). The first, a conductive boundaries reflects all of the impacting energy that reaches the edge back into the simulation space [47]. Retarding boundaries calculate what the field value will be

next to the simulation edge, assuming that all of the energy is propagating out of the simulation space at a single speed or mode [48]. Finally, the Perfectly Matched Layers (PML) inserts a layer of absorbent type material designed to match the dielectric properties of the simulation space while attenuating the radiated energy [49]. However both the retarded and PML BC's depend upon a single fixed speed of energy propagation impinging upon the boundaries. While this limitation is true for EM waves, these techniques are difficult to implement for the multiple speeds of energy propagation with a plasma. Plasma can support energy traveling at the speed of light, or slower depending on the wave frequency relative to the plasmas critical frequencies. This discrepancy of the BC's only being able to handle a single propagation speed was one of the leading cause of instabilities in Olakongal's model [44]. As the "slower" moving plasma waves impact the edge, the traditional EM BC's accelerate the energy to the speed of light. This discontinuity then acts like a secondary drive source, radiating energy back into the simulation space according to Huygens principle which disrupts the "infinite" space effect [10, 13, 47–49]. To make matters worse, ignoring the fast waves and redesigning the BC's for the "slower" plasma waves will also create a discontinuity for the "faster" pure electromagnetic waves.

A close evaluation of equations 2.42-2.44 or 2.64-2.66 shows that if the plasma is cold ($T = 0$), the velocity is only dependent upon the electric and magnetic fields in adjacent cells, and past instances of the velocity within the same cell. So long as the velocity is never calculated in the same cell that the EM BC is applied, the velocity for cold plasma will remain accurate, regardless of the density and/or ambient magnetic field, see fig. 2.3.

However, the calculation of the density of the plasma is not as easy to address. Equation 2.46 or 2.63, is dependent upon both the velocity and density in adjacent cells, see fig. 2.3. Since the velocity can be validated for cold plasma in the adjacent cell, the limiting factor upon the PF-FDTD BC becomes the difficulty in forcing the density to remain constant along the edge of the simulation. In essence, this technique will remain accurate as long as the compressional acoustic waves do not impact the boundary, and the density variations of the EM generated plasma waves remain small. Chapter 3 will show that this is an

acceptable approximation for small signal drive sources.

Once the velocity and density are accurately calculated, they can be applied to the electric field via the induced current in Maxwell's equations 2.35-2.37 or 2.57-2.59. This gradual stepping of the simulation parameters, from the simulation edge, enables a cold collisional magnetized plasma to be modeled two cells inside the application of traditional EM BC.

The transformation from cold to warm/hot plasma follows a similar process of reanalyzing the equations (2.42-2.44 or 2.64-2.66). This time, however, the velocity calculation becomes dependent upon the density in the adjacent cells, implying that the warm plasma cannot be simulated until the cold plasma has been accounted for, see fig 2.3. Once the warm plasma has been phased in, four plus cells from the simulation edge, the remaining simulation space will see an infinitely warm collisional magnetized multi-species plasma environment. This lasts until the slow moving compressional plasma waves impact the boundary, violating the constant density assumptions and reflecting some of the energy back to the driving source.

2.5 Defining the Antenna

One of the greatest benefits in implementing the PF-FDTD for antenna-plasma studies is that any antenna geometry can potentially be modeled. The only limiting factor becomes the discretization of the actual antenna using the PF-FDTD cells, see fig. 2.1, and how the various fields are treated at the boundary of the antenna. Simply stated, any antenna that is made out of a good conductor can capitalize on the fact that all tangential electric fields must equal zero. Any dielectric material can be modeled by changing the free space permittivity of Ampere's equations 2.35-2.37 or 2.57-2.59 to a free space permittivity times the effective permittivity of the dielectric ($\epsilon_0 \Rightarrow \epsilon_0 \epsilon_r$).

The only new complexity in modeling an antenna in a PF-FDTD becomes dealing with the plasma fluid variables and determining if the plasma should be allowed to enter the antenna structure or should any impacting particle be reflected away from the surface of the probe. The following section will outline two different antenna geometries; the thin

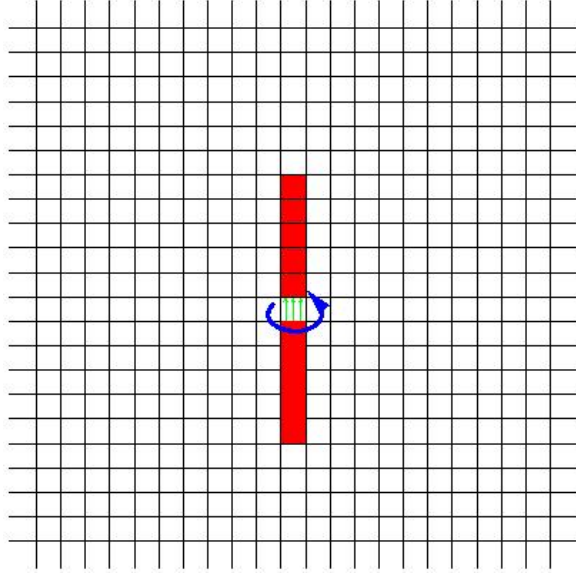


Fig. 2.4: A representation of a thin wire dipole antenna. E_z is set to zero within each red cell and a voltage feed gap is applied at the center.

wire model and the microstrip patch model. Both models have been used in PF-FDTD simulations runs and results are shown in Chapters 3 and 4.

2.5.1 Thin Wire Model

The easiest antenna to implement in the PF-FDTD is the thin wire probe. The definition and placement of the electric field within the PF-FDTD cell, see fig. 2.1, provides a natural thin wire model. A \hat{z} -axis oriented antenna, needs only to set the E_z term to zero while allowing all other field values to be self-consistently calculated, see fig. 2.4. Even the plasma density and velocity, which also exist at the center of the cell, are left to float to whatever value the initial conditions/equations specify. Conceptually the actual antenna occupies only a small portion of the actual cell, while plasma occupies the remainder. The values specified by the centrally located density and velocity, represent an average over the entire cell.

However, one important difference exists between the PF-FDTD and analytical model in how a thin wire is defined. Analytical models assume an infinitely thin wire and force only the tangential fields at the wire to be zero, while allowing the fields next to the wire

to vary freely. The PF-FDTD however, models all of the fields with the same polarity, in the given cell, as being forced to zero. This subtle difference yields an effective diameter to the actual modeled wire. In fact, the only way to truly model an analytical thin wire probe is to decrease the size of the cell to zero. As a result, the wording “thin wire” becomes very subjective. In fact any monopole or dipole that can be modeled with only a single column of vertical cells can be call a thin wire, with the actual physical diameter of the wire being determined by the averaging of the electric fields from one cell to the next, within the equations.

2.5.2 Microstrip Patch Model

The PF-FDTD is not limited to simple dipole, monopole, or loop probe geometries. In fact, any geometry can be investigated, so long as it can be represented by a combination of PF-FDTD cells. This enables the study of microstrip patches and other more complex structures.

To properly model a microstrip antenna in the PF-FDTD, all of the field values must be properly addressed. The electric and magnetic fields can be specified using a combination of conducting and insulating surfaces, see fig. 2.5. Any metalic surface is represented by setting the tangential electric field, within the cell of interest, to zero. Insulators are defined by introducing an an effective dielectric constant within Ampere’s equation (2.2) for the chosen cell. It is even possible to represent a ground plane as a perfectly conducting simulation boundary condition, in place of the decoupled simulation edge. In general, any traditional EM FDTD technique can be used to define the electric and magnetic field antenna boundary conditions [50, 51].

Since the antenna is composed of PF-FDTD cells, which consist of both a density and velocity component, antennas have one of three options. The first is to do nothing and let the plasma invade the antenna structure. This type of treatment is similar to the treatment of the plasma in the thin wire antenna simulation, outlined above. The second is to reflect any impacting particle on the antenna with the same but opposite velocity, similar to a tennis ball hitting a wall. While this is relatively easy to do and only requires

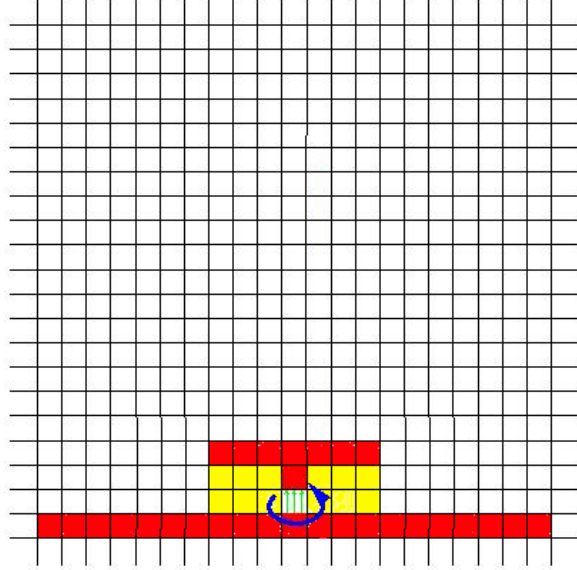


Fig. 2.5: A representation of a microstrip patch antenna. E tangential is set to zero within each red cell and a voltage feed gap is applied at the base. An electrical dielectric can be inserted between the top plate and the conductive BC.

negating the calculated velocity at the surface of the antenna, it assumes that no charges are transferred to the structure. The third approach, is to create an additional variable similar to a conductance term (σ) that can be inserted into Amperes equation,

$$\nabla \times \vec{B} = \epsilon\mu \frac{\partial \vec{E}}{\partial t} + \sigma\mu \sum_s q_s n_s \vec{U}_s . \quad (2.67)$$

This sigma can then be used, like a flag, to enable and disable the coupling between the plasma and EM waves. This same flag can also be used to turn off the velocity vector that represents the plasma entering the antenna. This enables the approximate modeling of a sheath region around the probe's surface. The plasma that is attracted to the antenna, due to the variations in the electric field, is then able to collect along the surface of the probe. It is this third option that will be implemented in the discussion of microstrip patch plasma impedance probes in Chapter 4. However, the increase in simulation memory requirements and the limited computational resources available, prevented a complete investigation into this third method in the course of this dissertation.

2.6 Driving the Antenna

In order to properly determine the input impedance of an antenna, it must be driven with a source capable of stimulating the plasma environment. The most common way of driving an antenna, in traditional FDTD models, is through the use of a feed gap [47]. Based upon the integral form of Gauss's Law,

$$V(t) = \int \vec{E}(t) \cdot dl = E_z^t(i, j, k) dz , \quad (2.68)$$

an antenna aligned with the \hat{z} axis, is driven with a voltage, V , at its input by forcing the electric field to be $E_z = V/dz$. This enables the user to relate a given drive voltage to a prescribed electric field within a PF-FDTD cell. This cell or others like it, can then be placed within the antenna structure to represent the probes physical feed point. The potential difference created between the neighboring cells act very similar to the feed point in a waveguide, with electromagnetic waves launched along the confines of the antenna geometry.

One must be careful however when dealing with complicated structures, like a microstrip patch, as it is possible to inadvertently provide an improper conductive path ($\vec{E}_{\text{tangential}} = 0$) between the two neighboring cells of the feed gap source. If such a conductive path were to occur, the source would effectively be shorted and little to no energy would enter the plasma environment.

Once the voltage is applied, the resulting feed current can be monitored. This is done through the integral version of Ampere's equation, which when converted to the discrete from becomes, see fig. 2.6,

$$\begin{aligned} I(t) &= \oint \vec{H}(t) dl \\ &= \frac{dx}{2\mu_0} [B_x^{t-1/2}(i, j, k) - B_x^{t-1/2}(i, j + 1, k) + B_x^{t+1/2}(i, j, k) - B_x^{t+1/2}(i, j + 1, k)] \\ &\quad + \frac{dy}{2\mu_0} [B_y^{t-1/2}(i + 1, j, k) - B_y^{t-1/2}(i, j, k) + B_y^{t+1/2}(i, j, k) - B_y^{t+1/2}(i, j + 1, k)] , \end{aligned} \quad (2.69)$$

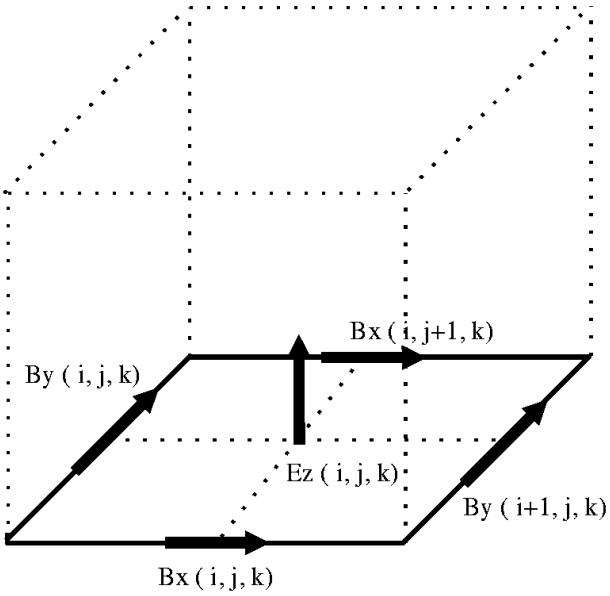


Fig. 2.6: Grid values used to calculate the feed terms.

with the temporal averaging occurs so that the feed voltage and current can be known at the same instant in time, see fig. 2.2.

After the voltage and current are found in the time domain, equations 2.68 and 2.69 respectfully, they must be converted into the frequency domain to calculate the impedance. The Discrete Fourier Transform (DFT), or Fast Fourier Transform (FFT) can be used to perform the time to frequency domain transformation (\mathcal{F}). Once in the frequency domain, Ohm's law can then be used to calculate the input impedance of the feed point,

$$Z(\omega) = \frac{\mathcal{F}(V(t))}{\mathcal{F}(I(t))} . \quad (2.70)$$

However, care must be taken if there is any phase variations associated with the drive source. If these phase variations extend past π and 2π , it is possible to introduce branch points that can create false resonance conditions.

In addition, it is possible to reverse the order by applying a current and measuring the forced voltage. In doing so, care must be taken not to physically constrain the feed voltage, by setting it to zero along with the other tangential electric fields.

One final point of interest is that by monitoring the current, equation 2.69, elsewhere along the antenna, the probes self-consistent current distribution can be determined, see Chapter 3.

2.6.1 Multi-Frequency Analysis

To produce a numerical analysis similar to the analytical techniques of Balmain and others, multiple frequencies are needed. This leaves the researchers to either perform multiple single frequency simulations or implement a multi-frequency analysis. The fundamental concept of the multi-frequency source is based upon finding the impulse response of the system. While in reality, a impulse function is difficult to create, raised cosines and gaussian pulses yield similar results. These time domain varying sources enables the modeling of a broad range of frequencies all within the confines of a single iteration.

While this is the standard method for finding free space input impedances for ordinary FDTD models [47], there are three significant limitations of this method when applied to the PF-FDTD. First, since this method is based upon the impulse response of the system, all voltages and currents must be recorded over the entire transient responses. This can take considerable time and iterations considering the broadband nature of the drive signal. Second, as Nyquist put it, in order to resolve a single frequency you must have two data points per cycle [52]. In other words, in order to obtain a reasonable low frequency resolution of the input impedance, the simulation must be ran for at least half the cycle of the lowest frequency of interest. This can be problematic as the nature of the simulation is dictated by the physical make up of the antenna and not the desired frequency range. Finally, since the plasma itself is to be measured, any signal with a net DC component will either drive the plasma away from the antenna or attract the plasma to the it. The generations or sink that must occur at the simulation edge, to provide the needed plasma or remove it, can easily overwhelm the BC. As the BC fail, so to does the rest of the simulation. As a result a source like a gaussian derivative should be used,

$$V = \frac{t - \delta}{\sigma^2} e^{-(t-\delta)^2/2\sigma^2}, \quad (2.71)$$

where σ^2 is the variance and δ is the median of the function. The natural restoring nature of this signal removes the burden from the BC while still enabling the simulation of a broadband source [47].

2.6.2 Single-Frequency Analysis

If results of the PF-FDTD are only needed at a single fixed frequency, then the 2 equation - 2 unknown method proposed by Furse is more than adequate [53]. The 2 equation - 2 unknown method is based upon the concept that only two values are needed to resolve a sine wave, in both amplitude (A) and phase (ϕ), assuming that the time between the points (Δt) and the frequency of the sine wave (f) are known:

$$V_1 = A \sin(2\pi f t_1 + \phi) , \quad (2.72)$$

$$V_2 = A \sin(2\pi f t_2 + \phi) , \quad (2.73)$$

$$\Delta t = t_2 - t_1 . \quad (2.74)$$

When this technique is applied to a feed voltage and resulting current, the calculated amplitude and phase of the sinusoidal signal must be converted into the electrical engineering phasor form ($A\angle\phi$), similar to the Fourier transform method (2.70), in order to calculate the effective input impedance.

This method is a quick way to gain a frequency response, as the signals only have to reach steady state. In fact, by properly choosing the frequency and phase of the driving source, so as to minimize transient effects, it becomes possible to resolve the input impedance of an antenna within a few hundred iterations, as opposed to the thousands required for the broadband source. However, care must be taken in assigning the two points needed, so that enough time and variation has occurred to properly resolve the amplitude and phase. The only real drawback to this method is that it only yields results at a single frequency, and one frequency value is not enough to resolve all of the plasma physics, see Pfister's model in Chapter 1. As a result, a complete set of single frequency simulations must be run, counteracting the decreased time to complete a single simulation over that of the extensive

iterations required for the multi-frequency method.

2.7 Additional PF-FDTD Issues

Two final issues must still be addressed concerning the development of the PF-FDTD. The simulation units must be defined, which includes a discussion on the Covrant condition, and method of implementing the initial conditions of the differential equations, Maxwell's and the Fluid equations, must be presented.

2.7.1 Simulation Units and the Covrant Condition

Like many numerical models, the development of the PF-FDTD has remained relatively unit less and dependent upon the definition of the fundamental variables. In fact, with a simple change of constant values; c_0 , ϵ_0 , μ_0 , q , m_e , and k_b , the fundamental equations will hold true for either Centimeters-Grams-Seconds (CGS) or Meters-Kilograms-Seconds (MKS) unit schemes. The only limiting factors become the amount of time that each iteration represents (dt) and the spatial size that each cell represents (dx, dy, dz). These two factors however, are intertwined with each other, in that, the simulation can only temporally progress as fast as it takes the energy to spatially propagate the smallest length of one PF-FDTD cell. This condition, the Covrant condition, assumes that the fastest mode of transportation is the speed of light [47, 50],

$$dt \leq \frac{\min(dx, dy, dz)}{c_0 \sqrt{3}} . \quad (2.75)$$

Any violation of this condition will introduce significant errors and instabilities.

Because of the cyclical nature of the units, it is best to leave the final assigned values to the type of problem to be addressed. However for clarity, the remainder of the dissertation will use MKS units.

2.7.2 Initial Conditions

The definition of initial conditions is critical in solving any differential equation. The

PF-FDTD is no different. Initial conditions are required for all of the various field values, \vec{E} , \vec{B} , \vec{U} , n , and scalar quantities T , ν . For the nonlinear model, this is done by predefining each field value within each PF-FDTD cell for the various arrays. The linear model can also accept initial conditions within each array, but the presents of the scalar qualities E_{0x} , E_{0y} , E_{0z} , B_{0x} , B_{0y} , B_{0z} , U_{0xs} , U_{0ys} , U_{0zs} , n_0 , T , and ν is a natural way of inputting the initial conditions. While the later technique eases the overall memory load of a single simulation, individually assigning each PF-FDTD cell can enable the modeling of large-scale sheaths, plasma bubbles, and localized drifts. The implementation of these additional effects can more accurately model the physics associated with satellites and sounding rockets. However, the runs presented in later chapters have considered only initial magnetic fields and densities, with density gradients and drift effects beyond the scope of this dissertation.

As pointed out in Chapter 1, the presents of charged particles and an ambient magnetic field create natural oscillations within the plasma environment. These oscillations in turn couple with the antenna to yield distinctive resonances. Because of these resonance frequencies, and the ability to measure them with RF probes, it becomes natural to use them as the initial conditions. The plasma density can be specified with a plasma frequency, equation 1.2, while the gyro frequency specifies the magnitude of the ambient magnetic field, equation 1.36. To decompose the magnitude of the magnetic field into the vector components of the PF-FDTD cell, one must also define an angle of incidents in both elevation (ϕ) and azimuth (θ),

$$B_{0x} = B_0 \cos(\theta) \sin(\phi) , \quad (2.76)$$

$$B_{0y} = B_0 \sin(\theta) \sin(\phi) , \quad (2.77)$$

$$B_{0z} = B_0 \cos(\phi) . \quad (2.78)$$

It is the definition of these initial conditions, in conjunction with the boundary conditions at the simulation edge and the antenna, which enable the PF-FDTD to model countless antenna plasma interactions. This simple fact opens the door to a world of possible plasma probes that before could only be imagined.

Chapter 3

Validating the Plasma Fluid Finite Difference Time Domain (PF-FDTD) Model

The problem at hand, how to relate the input impedance of an antenna immersed in plasma to the plasma environment, can be an overwhelming task. The combination of the countless variations of the plasma environments and the countless possible probe conditions can make it difficult to distinguish which input impedance features are caused by the plasma and which are caused by the antenna. This chapter will attempt to break down the various conditions into manageable groups. All of the figures in this chapter can be obtained using the PF-FDTD program and its supporting software outlined in Appendix A and found on the accompany compact disk, see Appendix B.

Initially, the free space responses of a dipole antenna will be analyzed using the PF-FDTD in an attempt to determine a mapping technique between the real world and the numerical model. This mapping will enable the physical antenna dimensions to be converted over directly to the number of cells and the size of the spatial increments used to represent the probe within the PF-FDTD. This will then allow for a direct comparison between the PF-FDTD and analytical theory.

After presenting many of the stability issues associated with the PF-FDTD, the plasma environment will be introduced, one parameter at a time. First, the effects of the plasma density will be analyzed, specifically the effects that plasma has on the input impedance of a dipole, the current distribution along a dipole, and the radiated energy away from a dipole. Second, a parallel DC magnetic field, which adds a gyro/cyclotron resonance, will be simulated using the PF-FDTD. This discussion will follow the same format as the discussion of nonmagnetized plasma. Then there will be a discuss on the effects that a non-parallel

ambient magnetic field would have on a dipole, as seen by the PF-FDTD. Finally after the PF-FDTD results are verified to Balmain's model, additional plasma parameters will be analyzed. This will include the effects of varying the collision frequency, possible effects of varying the temperature, and even the effects of a multi-species plasma.

3.1 Free-Space Validation

The first task in validating the PF-FDTD model is to reproduce the well-known free-space impedance characteristics of a dipole antenna. In the absence of plasma, a dipole antenna should be capacitive at low frequency where wavelengths are large compared the physical dimensions of the antenna. At higher frequencies, the simulation should reproduce the geometrical half and full wavelength antenna resonance and the impedance characteristics associated with them.

A direct comparison of simulation results for an antenna of a given length and diameter is problematic for any FDTD simulation. The simulation grid cell dimensions are well known but they are discrete and limit the resolution with which an antenna's physical dimensions can be specified. The nature of simulating fields and boundary conditions over discrete spatial and temporal steps further blurs the exact physical dimension interpretation for an antenna represented by a few simulation cells. This is because the fields represent a spatial average across a cell. If the grid size was made very small relative to the antenna dimensions all of these effects should disappear, but the simulation memory requirements would become too large to deal with using current computers. The approach commonly taken in FDTD simulations of antennas is to calibrate the simulations effective antenna dimensions against an analytical theory [47]. We take a similar approach and use the analytic formula for a dipole antenna of arbitrary length and diameter from Balanis [10]. The resistive and reactive components are given by:

$$Z_{in} = R_{in} + jX_{in} , \quad (3.1)$$

where

$$R_{in} = \frac{R_r}{\sin^2(kL)}, \quad (3.2)$$

$$X_{in} = \frac{X_r}{\sin^2(kL)}, \quad (3.3)$$

$$\begin{aligned} R_r &= \frac{\eta_0}{2\pi} \left\{ \mathcal{C} + \ln(2kL) - C_i(2kL) + \frac{1}{2} \sin(2kL) [S_i(4kL) - 2S_i(2kL)] \right. \\ &\quad \left. + \frac{1}{2} \cos(2kL) [\mathcal{C} + \ln(kL) + C_i(4kL) - 2C_i(2kL)] \right\}, \end{aligned} \quad (3.4)$$

$$\begin{aligned} X_r &= \frac{\eta_0}{2\pi} \left\{ 2S_i(2kL) + \cos(2kL) [2S_i(2kL) - S_i(4kL)] \right. \\ &\quad \left. - \sin(2kL) \left[2C_i(2kL) - C_i(4kL) - C_i\left(\frac{kR^2}{L}\right) \right] \right\}, \end{aligned} \quad (3.5)$$

and where $S_i(x)$ and $C_i(x)$ are the sine and cosine integrals, η_0 is the intrinsic impedance of free-space ($\simeq 120\pi$), \mathcal{C} is Euler's constant (0.5772), k is the wave number ($k = \frac{2\pi}{\lambda}$) where λ is the wave length of the driving source, and L and R are the half length and radius of the dipole.

Figure 3.1 is the results of a PF-FDTD simulation run with a Gaussian pulse derivative source driving a center fed antenna of 11 by 1 cells with no plasma ($\omega_p \rightarrow 0$). The simulation grid size was $dx = dy = dz = 0.1$ m, giving a nominal antenna dimensions of $2L = 1.1$ m and $2R = 0.1$ m. The impulse current response was recorded over 2^{14} simulation time steps, equivalent to 2.73 micro seconds, and transformed to the frequency domain from which the antenna impedance was calculated. The top panels of fig. 3.1 show simulation input impedances results, in magnitude and phase, in comparison with Balanis's analytical theory for $2L = 1.1$ m and $R = 0.1, 0.05$, and 0.01 m, the bottom panel is for $2L = 1.2$ m and the same diameters. A good qualitative agreement is found between the simulation ($2L = 1.1$ m, $2R = 0.1$ m) and the analytic theory $2L = 1.2$ m and $R = 0.01$ m. This leads to an approximate PF-FDTD calibration equation,

$$2L = (\# \text{ cells} + 1)dx \quad (3.6)$$

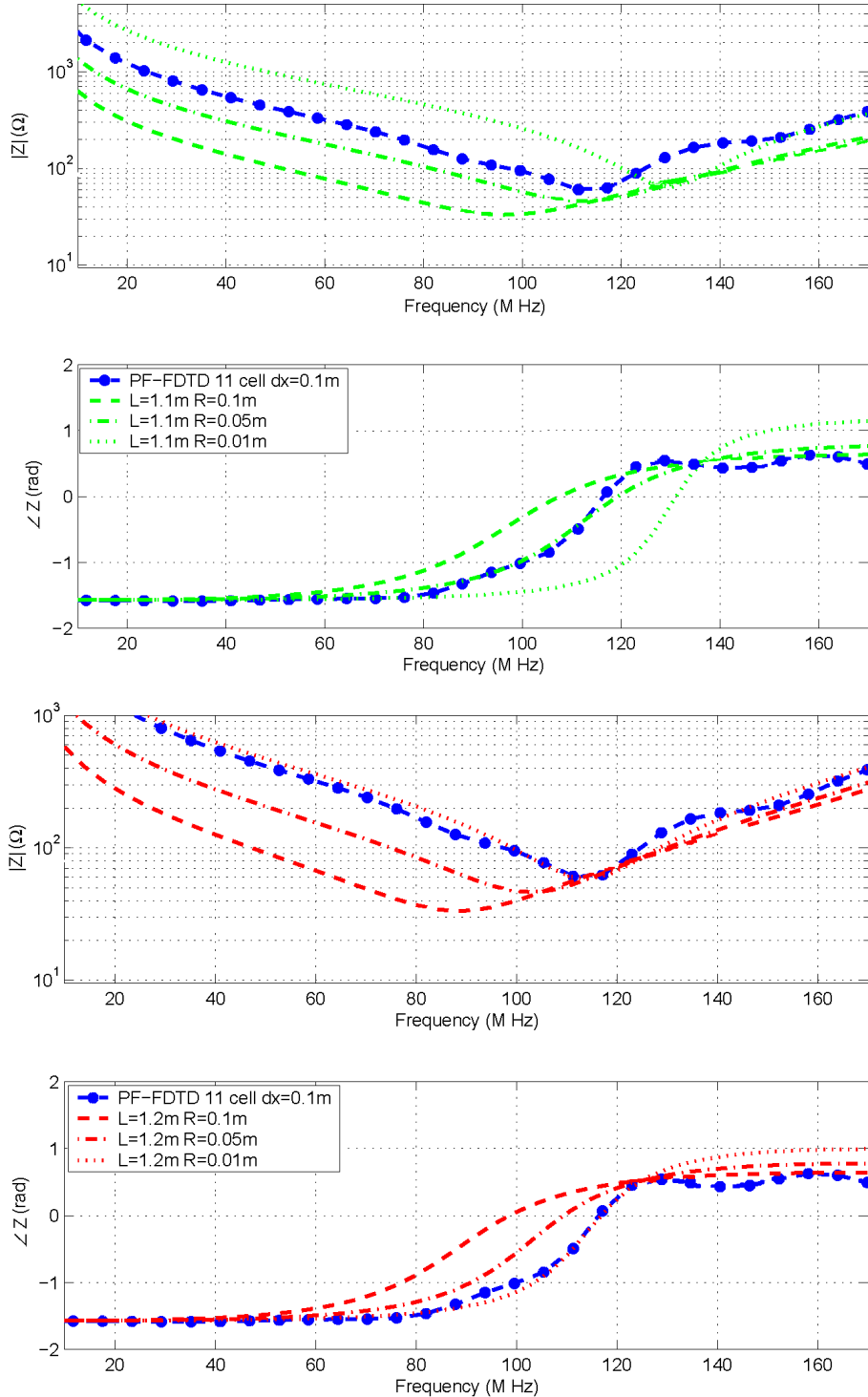


Fig. 3.1: The comparison of a 1-meter dipole in free-space and the PF-FDTD, for various L and R values, at frequencies near the natural half wave resonance point.

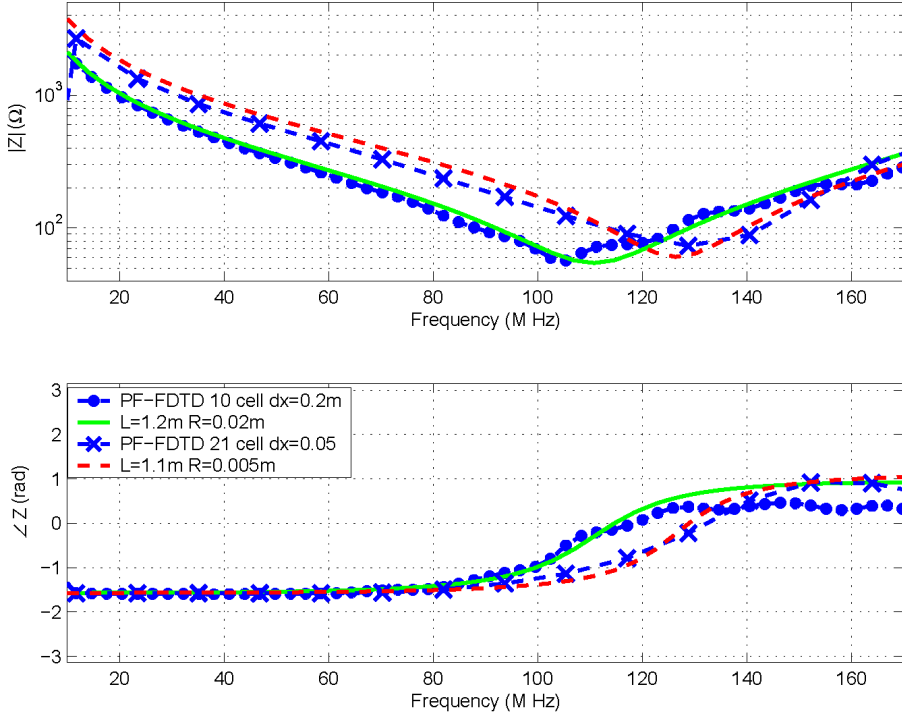


Fig. 3.2: The comparison of a 1-meter dipole in free-space and the PF-FDTD, for various dx values, at frequencies near the natural half wave resonance point.

$$R = 0.1dx . \quad (3.7)$$

This calibration is only approximate and ultimately depends upon grid size and the number of cells used to model the antenna. The range over which this relationship holds was explored by simulating a five element dipole with a regular grid of $dx = 0.5$ m and a 22 element dipole on a finer grid of $dx=0.5$ m. The scaling law of equations 3.6 and 3.7 was used for the analytic theory and the resulting input impedance magnitude and phase are shown in fig. 3.2. Good agreement is found beginning with the low frequencies and continuing through the natural half wave resonance point of the dipole. For the higher frequencies, the small L/R ratio results in a significant discrepancy in how end effects are treated. These end effects cause the variations between the PF-FDTD and the analytical model at the higher frequencies. As the L/R ratio is increased, the simulations high frequency data converges to Balanis data. However, it can become problematic to maintain a high L/R ratio and a high resolution at the low frequencies while performing the simulation within a limited

amount of computational memory.

3.2 Numerical Stability and Accuracy

Numerical models are stable so long as the error term within each calculation remains equal to, or smaller than, the previous iteration [35]. These errors can be introduced at many stages within a simulation. Modeling errors can be introduced during the derivation and construction of the model. The majority of these errors are easy to control by properly performing the temporal and spatial finite differences, by choosing the correct the spatial and temporal discretizations size for the given simulation, and by correctly terminating the flow of energy at the boundary. Improper treatment of these errors can either limit the flexibility of the model, as shown by Young [46], or introduces instabilities, as seen in Olakongal's model [44]. Additional errors, commonly called round-off errors, can also be introduced as real numbers are forced into the limited size of a computer registers (memory). While usually only occurring at the least significant bit, it is possible for these errors to multiply and compound over the course of a simulation. This type of error becomes the limiting factor in the PF-FDTD, as the simulations are run for as long as possible in an attempt to increase the low frequency resolution. The nonlinear simulation can only be run approximately 20 plasma periods while the linear simulation can exceed 100 plasma periods. In the next section, we will review several nonlinear and linear PF-FDTD model runs that demonstrate the accuracy and stability of the model as well as its limitations.

3.2.1 Effects of the Decoupling Boundary Conditions

The stabilizing effects of the boundary conditions developed in section 2.4 are shown in fig. 3.3 in comparison to no boundary conditions (a perfect conductor to only the electric field variations). The PF-FDTD simulation was initialized as a nonmagnetized cold plasma of $f_p = 2.8$ MHz and a collision frequency of $\nu = 1\% f_p$ and driven with a sinusoidal source of 20 MHz. Both simulations show the E_z component of the field some 20 grid points away from the antenna. For the first 5 ps of the simulation no signal is observed as the electromagnetic wave traverses to the observation location. A transient period lasting approximately 40 ps

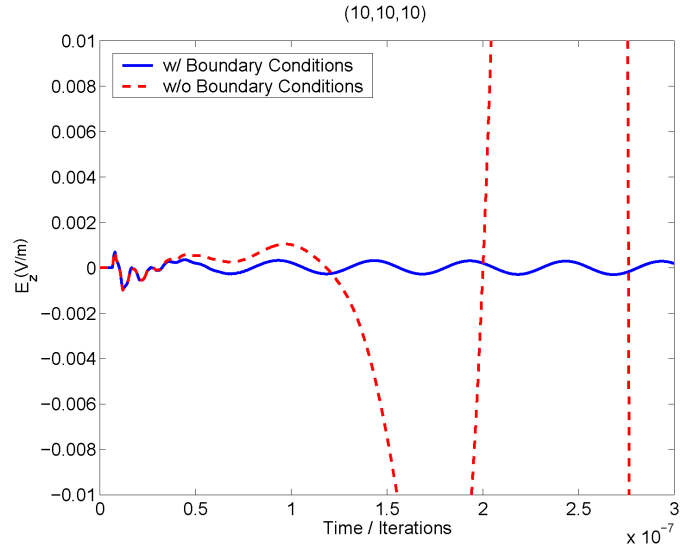


Fig. 3.3: E_z with and without the decoupling boundary condition. A $[40,40,50]$ $dx = 0.1\text{m}$ simulation of a 1.1 meter center fed dipole antenna with a sinusoidal source located at $(20,20,25)$ immersed in a $n_e = 10^5 \text{ 1/cc}$ ($f_p = 2.8 \text{ MHz}$) $\nu = 1\%f_p$ nonmagnetized cold plasma.

is then observed due to the discontinuous start up of the simulation after which the steady state 20 MHz signature of the source is observed. This is the transient period referred to in section 2.6.2, which must be allowed to settle before Furse's method can be used. The simulation with no boundary conditions went unstable after approximately 100 ps due to the inconsistency treatment of the EM and plasma fields at the boundary. The implementation of the decoupling boundary conditions allowed the simulation to remain stable.

To show that the new boundary conditions have little to no impact on the data within the simulation, two different sized simulations are compared. Figure 3.4, shows the electric field some 10 grid points away from the antenna for two different size simulations of the same warm magnetized collisional plasma. Both simulation use the decoupled boundary condition. By running the simulation for over 500 iterations the fast moving EM wave have enough time to impact the simulation edge and return. If significant energy was being reflected or generated at the boundaries then the electric field profile would be a function of simulation size. Instead, what is seen for these two warm plasma simulations are essentially identical electric field profiles.

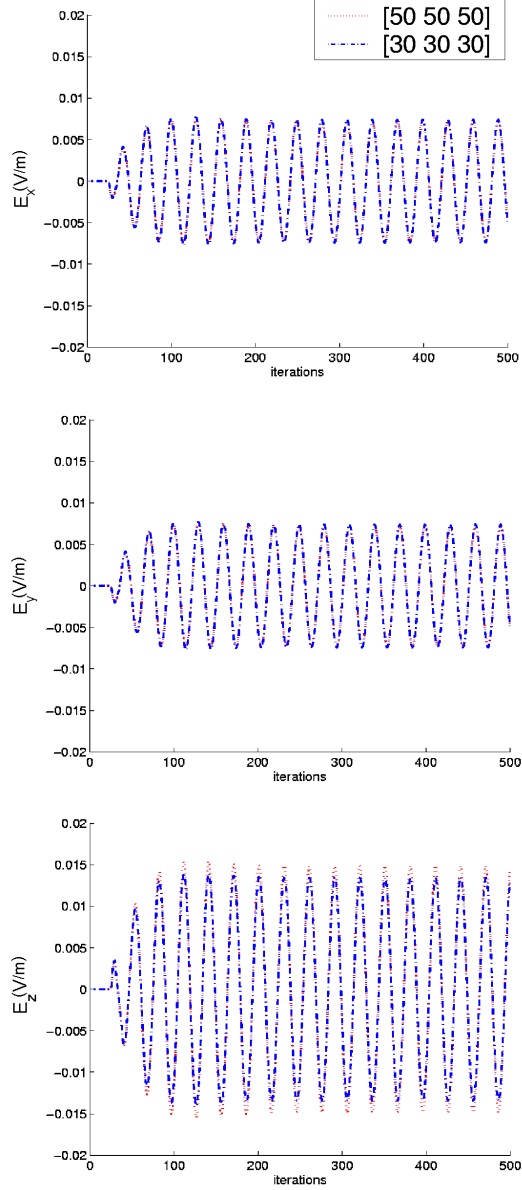


Fig. 3.4: Effectiveness of warm plasma boundary conditions using different sized simulations. E_x top, E_y Center, E_z Bottom. A center-fed 1.1-m dipole antenna with a sinusoidal source ($dx = 0.1$ m) centrally located in a $n_e = 10^5$ 1/cc ($f_p = 2.8$ MHz) $\nu = 1\%f_p$ $B_0 = 5 \times 10^{-5}$ T ($f_g = 1.4$ MHz) and $T = 1000$ K plasma. Measured at a distance of (10, 10, 10) cells away from the source.

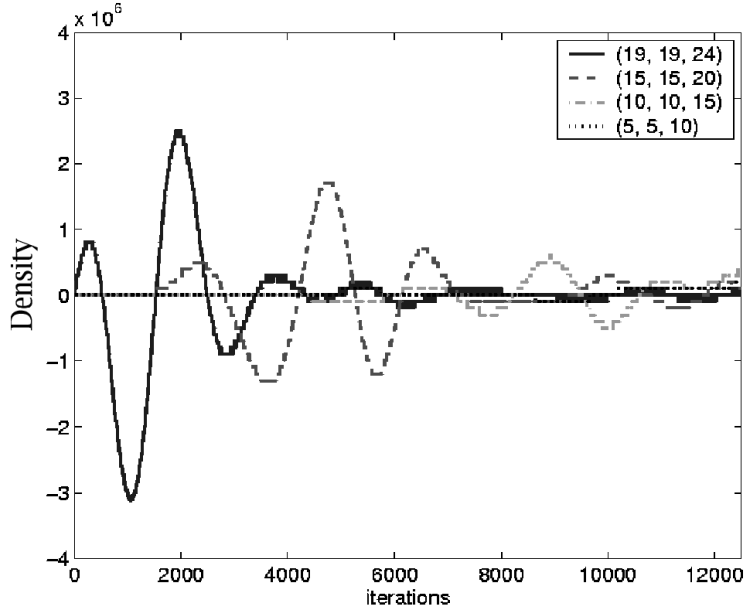


Fig. 3.5: Variations in density at different locations for a 1.1 meter center-fed dipole, centrally located in a [40,40,50] $dx = 0.1$ m simulation emersed in a $n_e = 10^5$ 1/cc ($f_p = 2.8$ MHz) $\nu = 1\%f_p$ nonmagnetized cold plasma.

The next simulation (fig. 3.5) shows the effect of a Gaussian derivative impulse on density as a function of time. The density is shown at several different locations progressively further away from the antenna. Because the plasma modeled is cold, many low-frequency wave modes do not propagate and are limited to only oscillatory modes. The density variations that are seen are the response of the plasma to the strong near fields of the antenna. They do not propagate and are quickly dissipated both temporally and spatially, consistent with the boundary condition requirement of constant density at the simulation edges. Other simulations have shown that as long as the simulation space is twice the largest probe geometry, the density of these near-field plasma oscillations is approximately zero at the boundary edges for a wide range of plasma conditions. This is not true if the input to the antenna has any significant DC frequency component such as a raised cosine or square pulse.

3.2.2 Bandwidth of Driving Source

The second type of error introduced in the PF-FDTD is best seen when analyzing the bandwidth of the driving source. For instance, to accurately model a one meter dipole antenna in a [70 70 65] size simulation with $dx = dy = dz = 0.04$ m, the temporal resolution must be less than $dt = 6.67 \times 10^{-11}$ as long as some of the energy is propagating above the upper hybrid. If just a simple cold collisional nonmagnetized single species plasma with an electron density of 10^3 cc was simulated, it would require approximately five plasma cycles to properly obtain the frequency resolution, or approximately 75,000 iterations. This is well over the traditional 1,000 iterations that most EM FDTD simulations are run. This extended length of iterations required to obtain a reasonable resolution at the desired low frequencies, causes the rounding off of small values in the data to become a larger problem.

Figure 3.6, clearly shows the effects of rounding off bits as the voltage and current values decrease to below an effective noise floor, a noise floor that is established by the multiplying of round off errors. For the cases in fig. 3.6, the applied voltage and resulting current reach the rounding off level at frequencies above 20 MHz for the source with a Gaussian derivative spike at 5 MHz, 40 MHz for the source with a spike at 10 MHz, and 60 MHz for the source with a spike at 20 MHz. The resulting low signal to high round off error can best be seen when the resulting impedance is calculated. The sharp transition in phase and magnitude is purely the introduction of a numerical error. As the amount of iterations increases, additional false impedance resonance conditions begin to appear as more frequencies begin to suffer from rounding off errors.

3.2.3 Maximum Iteration

Assuming that all other error producing effects are mitigated, the limiting factor in determining the maximum number of iterations for a given simulation, will be the time it takes any slower moving plasma waves to impact the boundary, reflect, and return to the source,

$$\text{Max Iterations} = \frac{2l}{V_s dt} , \quad (3.8)$$

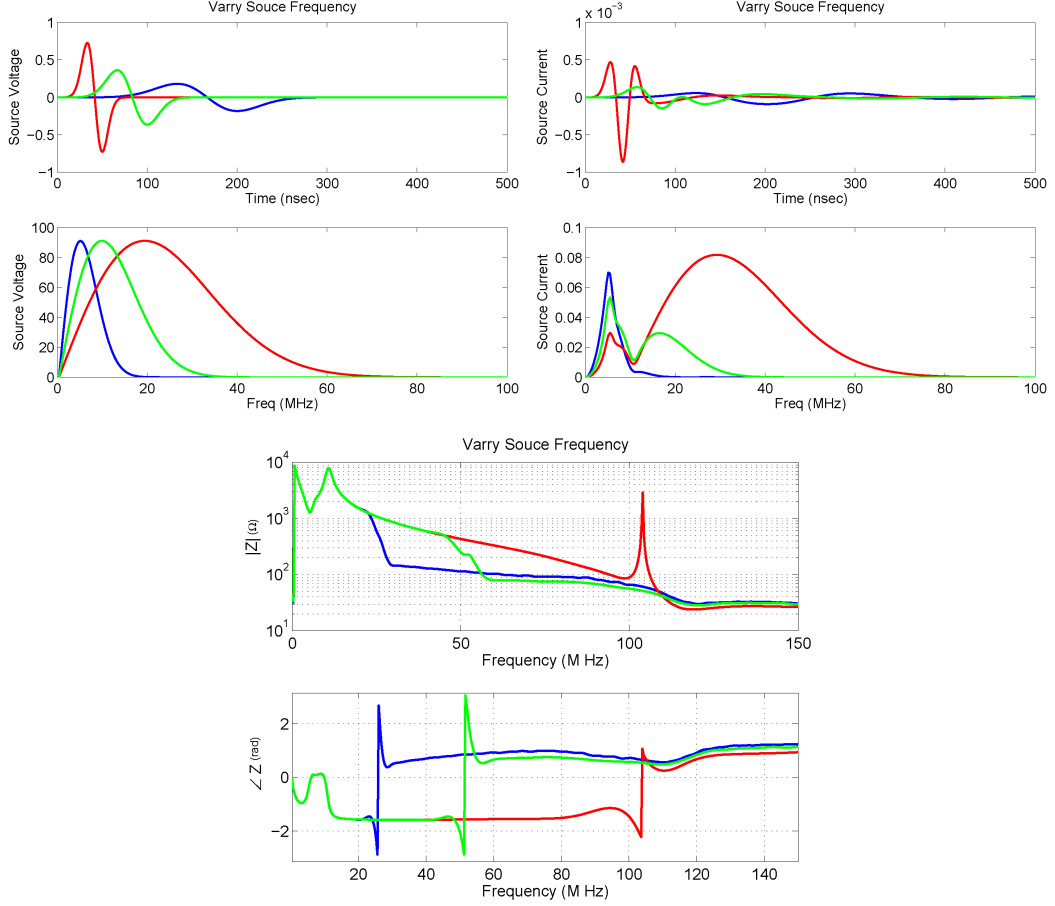


Fig. 3.6: Various applied voltage sources for a 1.1 meter center-fed dipole in a $n_e = 1.24 \times 10^6$ 1/cc ($f_p = 10$ MHz) with a magnetic field of 1.78×10^{-4} Tesla ($f_g = 5$ MHz) plasma.

where l represents the shortest distance between the probe and the simulation boundary and V_s is the speed of the slower moving wave. For the case of a cold collisional magnetized plasma, the Alfvén wave is the second fastest mode of energy propagation,

$$V_s = \frac{B_o}{\sqrt{\mu_0 n_s m_s}} . \quad (3.9)$$

Other modes of energy propagation exist in warm collisional magnetized plasma, each with their own speed of propagation that can be inserted into equation 3.8.

However when several nonlinear PF-FDTD were simulated, the results were not as expected, see fig. 3.7. While the $f_p = 15$ MHz and $f_p = 10$ MHz simulations show a

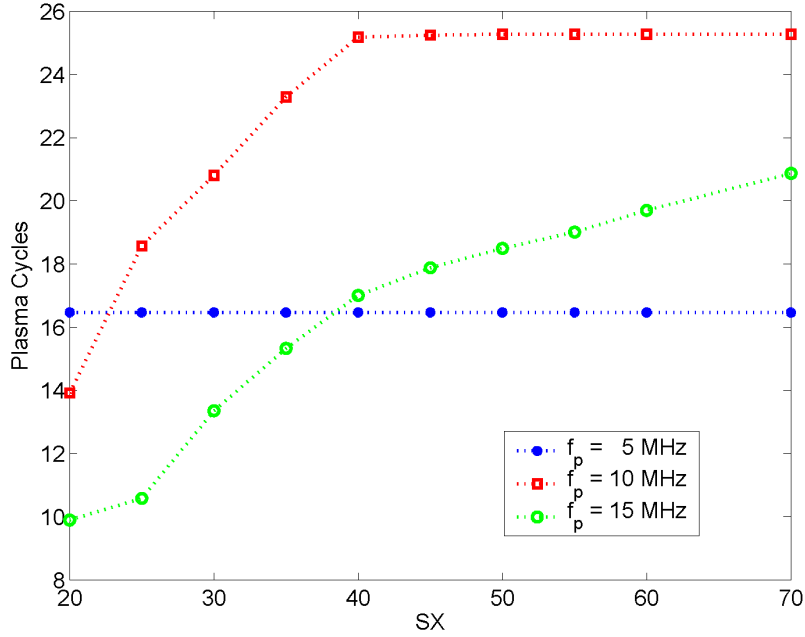


Fig. 3.7: Maximum iterations in plasma cycles versus simulation size for various plasma environments ran using the nonlinear model.

relationship of max iteration to simulation size, they became unstable prior to the calculated iteration of equation 3.8. In addition, the $f_p = 10 \text{ MHz}$ and $f_p = 5 \text{ MHz}$ entered a region of saturation. They became unstable regardless of the increased simulation space. It was not until further investigation that the cause of these instabilities was found.

The connection between simulation size and stability seen within the cases of $f_p = 15 \text{ MHz}$ and the low frequencies of $f_p = 10 \text{ MHz}$ is actually the impacting of the near field effects upon the simulation edge. These near field variations violated the constant density assumption of the decoupled boundary condition.

The second feature, the flat lining that is seen in cases $f_p = 5 \text{ MHz}$ and the high frequencies of $f_p = 10 \text{ MHz}$ is related to the rounding off of the least significant terms in the field values. For a fixed source bandwidth, the smaller the plasma frequency decreases the total amount of energy applied to the plasma. This results in smaller field variations that begin to approach the order of the round off bit. This can be mitigated by decreasing the source frequency in an attempt to maintain a constant power density near the plasma effects. In so doing, the desired signals are kept above the round-off error.

3.2.4 Nonlinear Versus Linear Models

Round-off errors are a part of all numerical models. However, the temporal and spatial averaging performed in traditional FDTD simulations helps to minimize the effects. This is not the case with the PF-FDTD. The direct multiplication of field values that occurs within the continuity, momentum, and Ampere's equations can actually compound the round-off error. For example, the nonlinear PF-FDTD can only run for approximately 20 plasma cycles, see fig. 3.7. When the linear PF-FDTD is properly implemented, the effects of the round-off errors decrease. This is not to say that the rounding off does not occur, but that the errors do not multiply as fast. This is why the PF-FDTD has been successfully run for over 200+ plasma cycles multiple times. These limitations in the amount of iterations greatly effect the accuracy of the PF-FDTD. In fact, the conversion from maximum iteration to frequency resolution (df) is based upon the Nyquist rate,

$$df = \frac{4}{\# \text{ of Iterations} * dt} . \quad (3.10)$$

The four comes from the fact that two samples are needed per signal cycle and that the FFT process relates the frequencies to values ranging from $-\infty$ to ∞ .

Even allowing the plasma resonances to occur in the 10's of MHz range, is not enough to properly resolve many of the low frequency plasma features. A simulation of cold collisional magnetized plasma ran for 20 plasma cycles has a low frequency resolution of only 1.75 MHz, were as one ran for 200 plasma cycles has a much higher resolution, see fig. 3.8. With this lower resolution it is even difficult to resolve the slope leading into the upper hybrid.

3.3 Nonmagnetized Plasma Results

The most basic and fundamental plasma parameter is the electron density. While plasmas can be cold or warm and magnetized or nonmagnetized, every plasma must have an electron density. By limiting the analysis of the PF-FDTD to just a cold nonmagnetized single electron fluid, with stationary ions, it becomes easy to identify the effects of the plasma density on the input impedance of an antenna, see fig. 3.9. A parallel resonance,

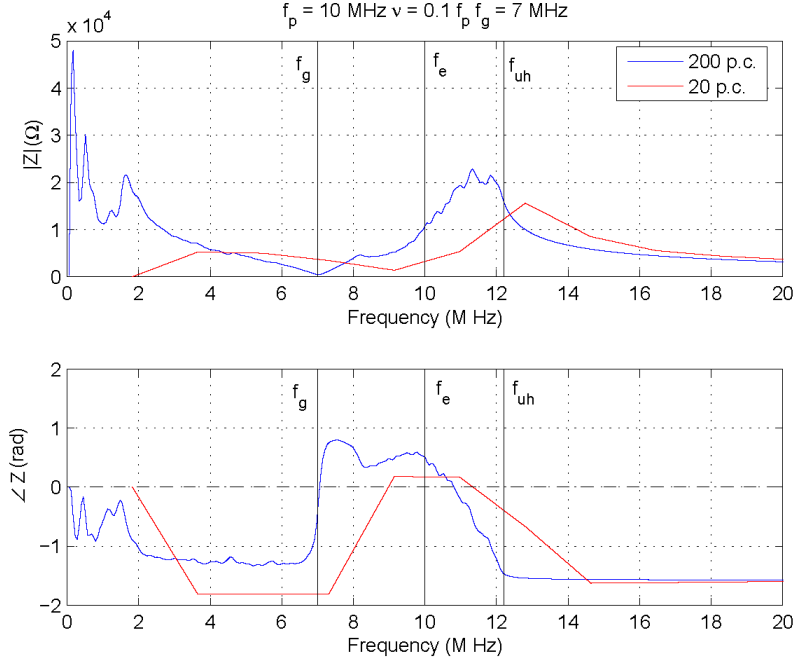


Fig. 3.8: A 1.1 m dipole antenna with in a cold collisional magnetized plasma simulated run for various maximum iterations.

at the plasma frequency, appears in the characteristic impedance curves. While there is obvious disagreement between the PF-FDTD and Balmain, the basic shape is the same.

At frequencies above the plasma resonance, the electromagnetic variation occurs too fast for the plasma to respond, leaving only the free-space impedance. However, as the drive frequency approaches the plasma resonance frequency (f_p), energy leaving the antenna is re-actively coupled into the motion of the electrons. During 1/2 of the electron cycle, energy is pumped into the electron oscillation; while during the other 1/2, energy is being reabsorbed by the antenna. As the electrons collide with other particles their paths are altered, either increasing or decreased the path of the oscillation. This causes a natural spreading of this interactive frequency as various frequency wavelengths resonate with the various paths of oscillation. The spike in magnitude is due to the fact, that since the plasma frequency is determined by a collection of electrons, any applied energy must stimulate the same collection of charged particles. This results in a higher input impedance as more energy is required to gain the same effect. Below the plasma frequency, as the drive frequency approaches zero,

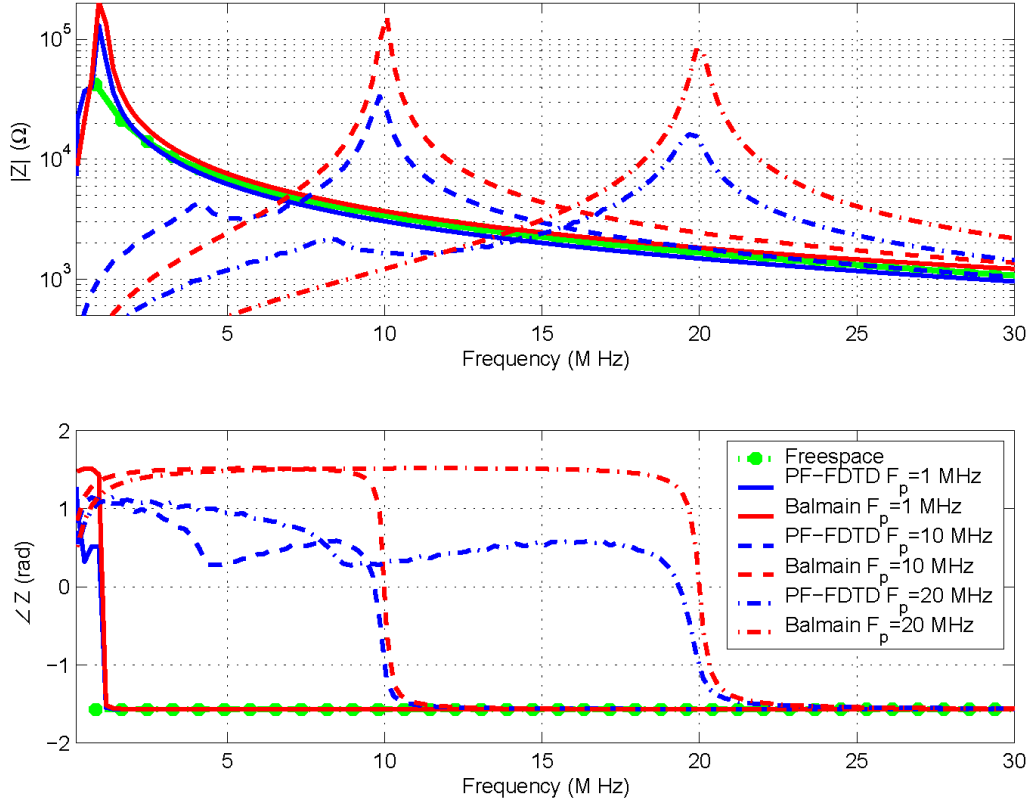


Fig. 3.9: The PF-FDTD versus Balmain for a 1.24 m x 0.004 m dipole for various plasma densities with no DC magnetic field. The PF-FDTD ran for 2^{16} iterations, between 4 to 80 plasma cycles.

the conductive nature of the plasma effectively shorts the two feed terminals of the antenna in an inductive type fashion.

Figure 3.9 also demonstrates the additional physics modeled by the self-consistent full wave solution, over the quasi-static analysis of Balmain. First, the PF-FDTD converges, faster than Balmain, to the free-space value. This is because the time variation of the vector potential is not forced to zero ($\frac{\delta \vec{A}}{\delta t} \neq 0$). Second, the magnitude of the PF-FDTD differs from Balmain at the parallel resonance, implying that the current may not be a pure triangular distribution, which is typically the case at a resonance frequency. Third, a new “resonance” is introduced, that coincides with a stimulation of electron and how they couple with an effective length of the antenna. This additional resonance appears to be a combination of full-wave effects and current distributions.

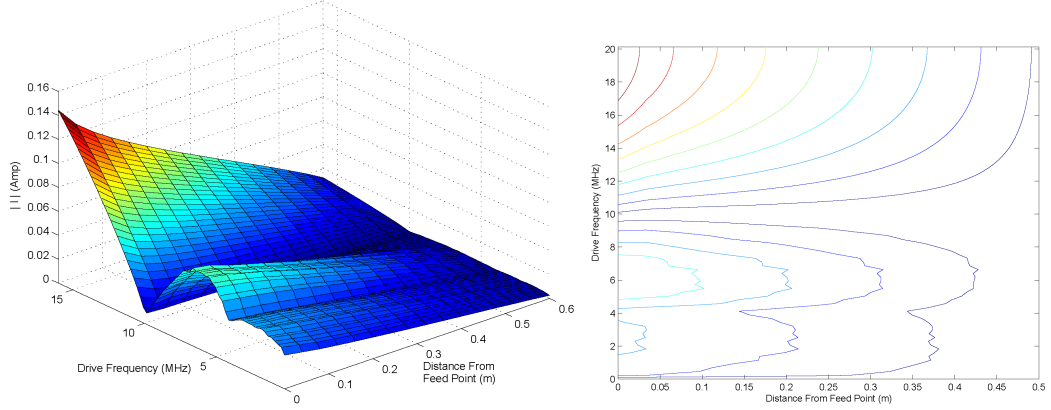


Fig. 3.10: The magnitude of the current distribution along a $1.24 \text{ m} \times 0.004 \text{ m}$ dipole antenna immersed in plasma density of $1.24 \times 10^6 \text{ 1/cc}$ ($f_p = 10 \text{ MHz}$) for various drive frequencies.

Current Distributions

The prescribed current distribution appears to be one of the greatest limiting factors of the analytical theories. The discrepancy between Balmain and the PF-FDTD theories at the peak of the resonance frequency within fig. 3.9 is a direct result of this dependence. The PF-FDTD predicts a lower resonance, similar to experimental observations [30]. This is due largely to the self-consistent calculation of the current distribution ($I(l)$) along the length of the dipole antenna ($2l$). When plotted (see figs. 3.10 - 3.12) the traveling and attenuating wave current distributions measured by Ishizone and modeled by Singh can be seen to various degrees, depending upon the drive frequency [31,32]. As the drive frequency nears the plasma resonance (fig. 3.12) the majority of the energy is dissipated near the feed point. This attenuating wave, produces an evanescent type distribution along the length of the antenna. This is similar to the exponential current distribution proposed by Nikitin and Swenson [14]. This attenuating wave effectively decreases the L/R ratio of the antenna, which decreases the peaks of the parallel resonances. A result commonly seen in the free-space full wave length resonance [54]. Once at the plasma frequency, the magnitude of the current distribution ($|I(l)|$) undergoes a significant change in shape. Below this cut-off frequency $I(l)$ is a combination of a traveling wave and an attenuating wave. These two types of $I(l)$ then cause the peak, in $|I(l)|$ to transition off of the feed point, at 8.463 MHz

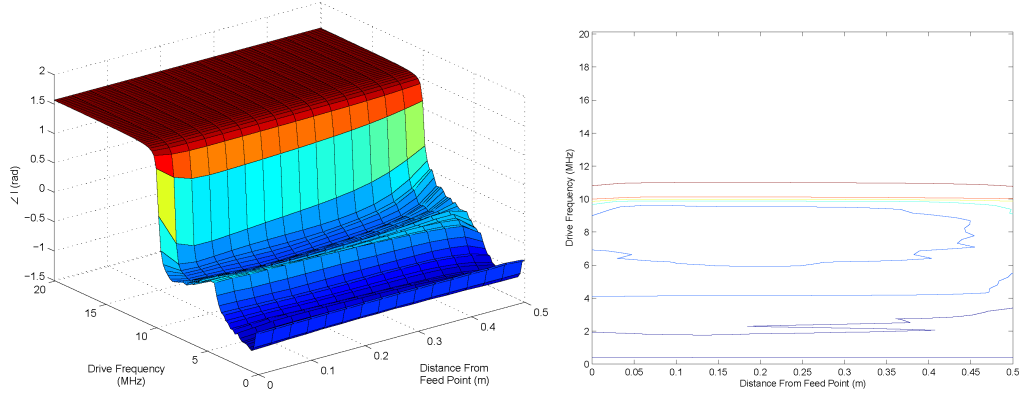


Fig. 3.11: The phase of the current distribution along a $1.24 \text{ m} \times 0.004 \text{ m}$ dipole antenna immersed in plasma density of $1.24 \times 10^6 \text{ 1/cc}$ ($f_p = 10 \text{ MHz}$) for various drive frequencies. The drive voltage is set to zero phase.

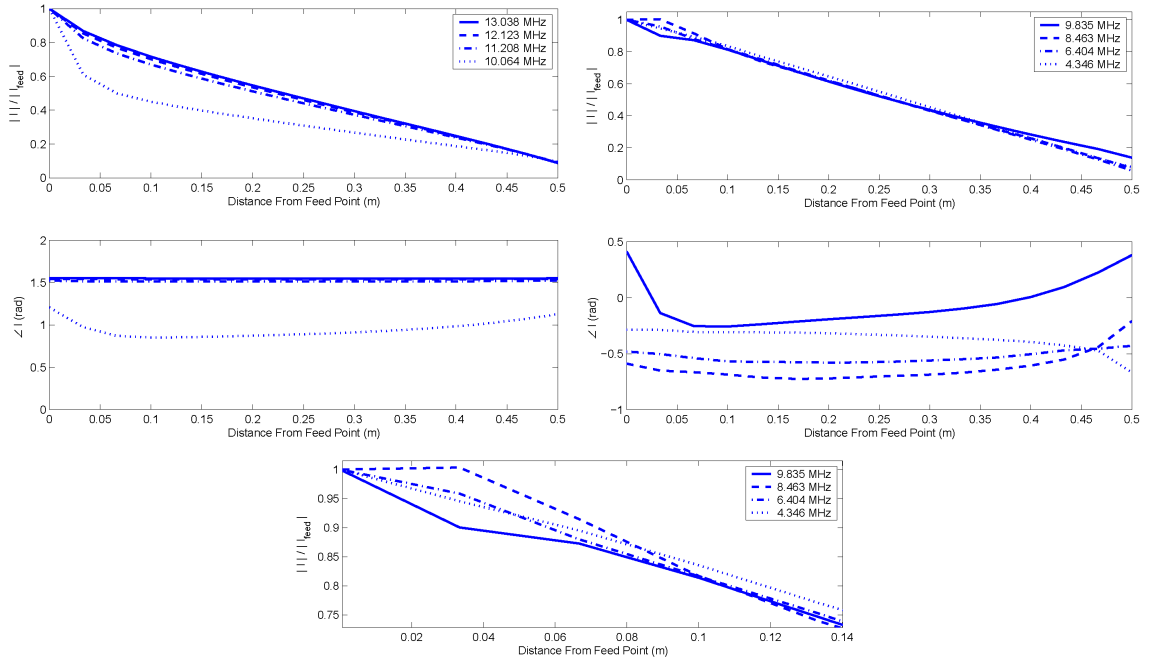


Fig. 3.12: The magnitude and phase of the current distribution along a $1.24 \text{ m} \times 0.004 \text{ m}$ dipole antenna immersed in plasma density of $1.24 \times 10^6 \text{ 1/cc}$ ($f_p = 10 \text{ MHz}$) for a few fixed drive frequencies. The drive voltage is set to zero phase. Note: The bottom figure is a close-up view of the upper right magnitude values.

in fig. 3.12. It is at this cut-off frequency, the plasma frequency, that the feed point current minimum occurs, see fig. 3.11. A secondary minimum, in the feed current magnitude, also coincides with the removal of the traveling wave, see 4 MHz in figs. 3.10 and 3.12. This secondary minor “resonance” appears to depend upon both the plasma conditions and the antenna geometry. It also appears to be coupled in with the additional resonance in the input impedance curve, see fig. 3.9.

The PF-FDTD provides a self-consistent calculation of the phase of the current distribution ($\angle I(l)$), taken to be constant in analytic approaches, see figs. 3.11 and 3.12. Above the plasma frequency, $\angle I(l)$ is the traditional constant ($\pi/2$). Once the drive frequency drops below the plasma resonance, the cut-off frequency in a nonmagnetized plasma, $\angle I(l)$ begins to transition to a negative phase, like that of an inductor. However, this decrease in phase appears to be stimulated by a point just off the feed location ($l = 0$), see fig. 3.12. It is almost as if the oscillating plasma has a wavelength of 0.15 meters in this case. This oscillation of the plasma may be greatly exaggerated at the feed point, since the two sides of the antenna are driven with voltages 180 degrees out of phase with each other. As this dip eventually “pulls” the phase of the feed point to zero, the phase of the input impedance ($\angle Z$) approaches zero, see fig. 3.9. The delay in frequencies, between when the decrease starts to occur (f_p) and when the phase of the feed point ($\angle I(l = 0)$) actually reaches zero, causes the zero phase of the input impedance ($\angle Z$) to occur at a lower frequency than the spike in the magnitude of the input impedance ($|Z|$). Additional frequency simulations have shown that this frequency shift is a result of antenna geometry, since the phase of all of the current along the antenna must be pulled negative. During the process of pulling the phase negative, $\angle I(l)$ also takes on a distinctive concave type nature. This concaveness continues until the second minor “resonance” in current magnitude is reached, however it should be noted that $\angle I(l = 0) \neq 0$ at this frequency. At this point, it appears as if the coupling of the plasma to the plasma resonance decreases and the $\angle I(l)$ transitions to a convex nature.

The transition between the convex and concave $\angle I(l)$ and the minor dip in $|I(l = 0)|$, explains the dip in $\angle Z$ and spike in $|Z|$ around 4 MHz for $f_p = 10$ MHz in fig. 3.9.

Similar effects can also be seen in the $f_p = 1$ MHz and 20 MHz, and all other data sets used throughout the remainder of the chapter. However, additional simulations have been inconclusive as to whether or not this additional feature is truly related to the effective length of the probe within the plasma, a harmonic of the plasma resonance, or possibly a combination of both. Regardless, there does appear to be a distinctive feature in the electron density variations that coincides with the secondary “resonance.”

Energy Flows

Throughout the frequency region of interest, centered around the critical plasma frequencies, the input impedance of the short dipole remains highly reactive. This implies based on equations 1.21 and 1.22, that the majority of the energy is stored within the fields near the antenna and that these near field effects predominantly control the input impedance to an antenna in this frequency range. One additional benefit of the PF-FDTD, besides monitoring the properties of an antenna, is that most if not all of the effected fields can also be monitored (depending on computer resources). This enables researchers to view how energy and waves propagate near a probe, in an attempt to minimize coupling effects between probes, or maximize sensitivity to a given coverage area.

To aid in this discussion, two specific points have been monitored throughout the majority of the simulations performed in this chapter, see fig. 3.13. Point \mathcal{A} will be referred to as being “perpendicular to the antenna” and point \mathcal{B} will be referred to as being “parallel to the antenna”. While these points are not equally spaced from the physical structure of the antenna, they are equally spaced from the feed point. This spacing was specified due to the realization that the majority of the energy should be dissipated near the feed point and not equally along the antenna, as evidenced by the current distributions.

Figure 3.14 shows the density variations from an initial value at points \mathcal{A} and \mathcal{B} , negative values represents a void and positive values represents an increased collection. A FFT was used to determine the frequencies at which these temporal variations occurred. When these temporal variations are analyzed. Two major effects appear the EM effect and the plasma effect.

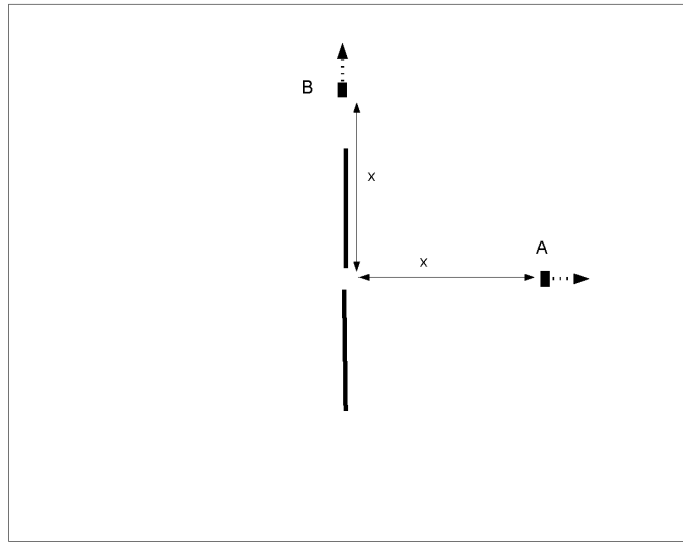


Fig. 3.13: Physical location of the density, kinetic energy, and Poynting vector measurements with respect to the probes' feed point.

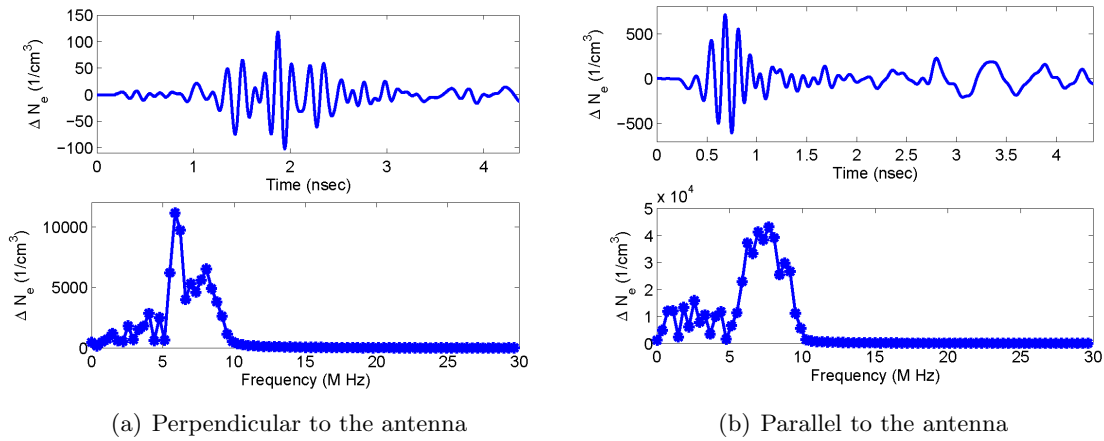


Fig. 3.14: Temporal and frequency fluctuations in the electron density, 1 m away from the feed point of a $1.24 \text{ m} \times 0.004 \text{ m}$ dipole antenna immersed in plasma density of $1.24 \times 10^6 \text{ 1/cc}$ ($f_p = 10 \text{ MHz}$).

The EM effects occur as the electromagnetic waves propagate past the measurement point and are resolved early in the simulation, approximately 1 ns for point \mathcal{A} and 0.5 ns for point \mathcal{B} . While expected in the electric and magnetic field data, the EM wave effects can also be seen in the plasma data, as the variations in the electric and magnetic field cause small local variations within the free electron and ion densities.

The slower plasma effects result more from a “shock” type effect, as the natural shielding of the plasma is unable to cope with the variations of a drive source. While these plasma variations cannot be considered plasma waves in the true sense, they do in fact propagate away from the source, slowly being dissipated, similar to an evanescent type wave. In addition to the EM and “plasma waves,” fig. 3.14 also exhibits the presence of a modeling error. The late time temporal oscillations, parallel to the antenna, appear to be due to the creation of a resonance cavity between the end of the probe and the decoupling BC. In the frequency spectrum, this error introduces a low frequency “noise” seen below the $1/2f_p$ point (5 MHz for $f_p = 10$ MHz). The effects of this cavity appear to be fleeting, since it disappears whenever a traditional energy propagation wave mode presents itself. It appears as if the wave propagation allows the energy to be either carried out of the simulation or away from the probe. For example, when a DC magnetic field is inserted (see the following sections) the $\vec{V} \times \vec{B}$ drift interrupts this resonance cavity, and the density variations disappear. While for the cases of no mode of energy propagation, the presence of this resonance cavity can raise some question about the legitimacy of the model. Any questions are quickly addressed by the fact that these variations occur at the end of the antenna. Even in free-space, because of the minimal amounts of currents present, it takes significant changes at the end of antennas to yield minor effects at the feed point [10].

It is also interesting to note, that while the plasma effects on the input impedance can be seen well above the plasma resonance, the electron movements are strongest in the range between $1/2$ to $1 f_p$. Outside of this range, especially above the plasma frequency, there is little variation. Ironically, it is in this region of density variations that the traveling wave appears in the current distribution (figs. 3.10 - 3.12), reaffirming some type of energy

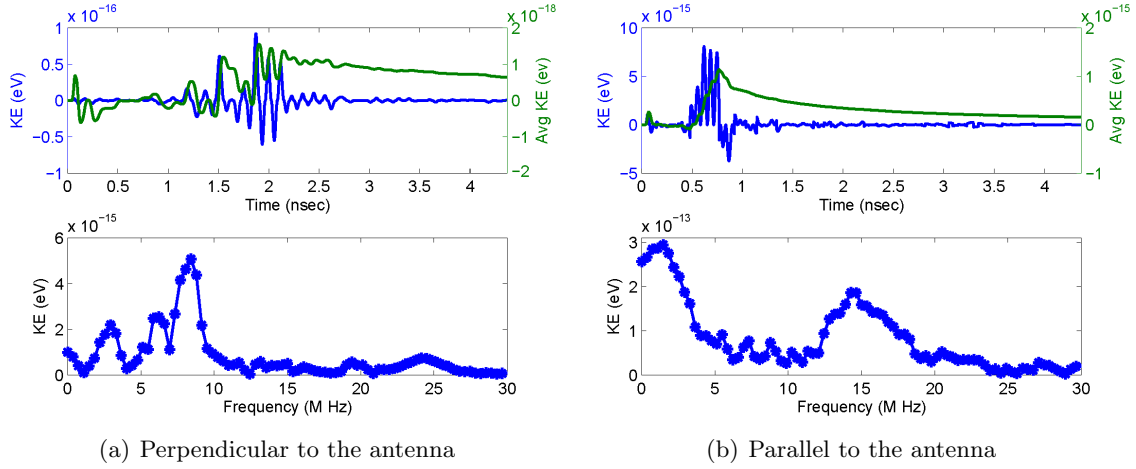


Fig. 3.15: Temporal and frequency fluctuations in the radial instantaneous and average kinetic energy, 1 m away from the feed point of a 1.24 m x 0.004 m dipole antenna immersed in plasma density of 1.24×10^6 1/cc($f_p = 10MHz$).

propagation/dissipation. While these variations appear to extend in all directions, they are most predominantly parallel to the probe surface. This implies that the continuous current flow along the antenna allows for an increased coupling with the plasma oscillating parallel to the antenna as opposed to the plasma flowing perpendicular.

The generation of a “plasma wave”/“shock wave” within the electron density can also enable the radiation of kinetic energy away from the probe,

$$KE_\rho = \frac{1}{2} m_e U_\rho^2 , \quad (3.11)$$

where ρ represents the radial unit vector in spherical coordinates. Figure 3.15 shows the radial kinetic energy at points \mathcal{A} and \mathcal{B} , and the frequency component of its variations. It should also be noted, that it is possible to have a constant flow of electrons through a PF-FDTD cell, registering as kinetic energy, but not as a density variation. This would be akin to radiation and should appear as a resistive effect on the characteristics impedance of an antenna. It is also possible to have a collection of particles being feed or drained by a constant kinetic energy. This would act like a reactive type device, similar to an inductor or a capacitor that could be charged or discharged given the correct situation. As such, this

effect should appear as a reactive type load in the input impedance of an antenna.

For the perpendicular case, point \mathcal{A} in fig. 3.13, there appears to be a direct correlation between the frequencies of density variation (see fig. 3.14) and the frequencies of kinetic energy propagation (see fig. 3.15). In that any energy propagating within this band is reactively stored in a localized plasma collection. While extensive runs are still required to explain much of the physics behind the various spikes and dips, it should be noted that the dip in the kinetic energy around 7 MHz coincides with the decreased density fluctuation just above the spike in the density (≈ 6 MHz) and that the additional increase in the perpendicular kinetic energy around 3 MHz appears to be a harmonic of the other two kinetic energy spikes. One additional feature that is of specific interest to this dissertation, is the presence of a small amount of radiated kinetic energy, shown as the final average kinetic energy. This points to the inaccuracy of the quasi-static approximation used in many of the analytical models.

It also appears as if more radiated kinetic energy effects appears at point \mathcal{B} . Since above the cut-off frequency, there is energy flowing through the simulation as the plasma density remains uniform. This implies that any energy within this band propagates directly to the simulation boundary. A similar effect also happens below the $1/2 f_p$ point, with the electrons able to absorb energy at frequencies between $1/2$ and $1 f_p$. However, a close examination of fig. 3.15, shows that these frequency limits are only a crude approximation. The actual limits appear to be dependent upon the geometry of the antenna and further research must still be conducted, in order to formalize a relationship. It is also unclear as to what effect the antenna simulation BC resonance cavity has on this topic.

A similar analysis can be performed on the radial Poynting vector ($\vec{S} = \vec{E} \times \vec{B}$), see fig. 3.16. In so doing, it appears as if the EM energy at \mathcal{A} , while showing a minor temporal presence of the plasma environment, does not exhibit any frequency dependence. The dip centered around 23 MHz is actually due to the round-off error associated with the Gaussian derivative drive source. However, the EM energy at \mathcal{B} , does exhibit a temporal and frequency plasma presence. Moreover, the parallel variations of \vec{S} appear to be combinations

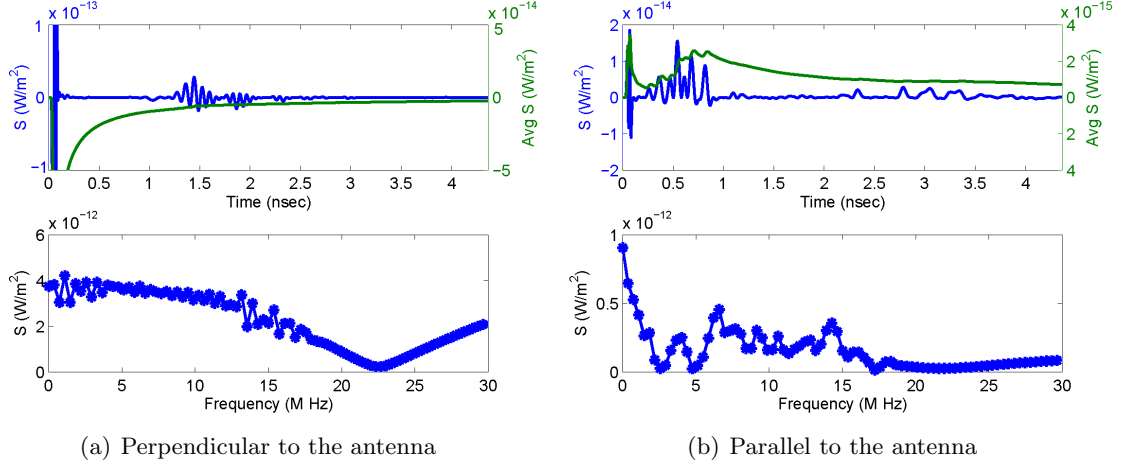


Fig. 3.16: Temporal and frequency fluctuations in the radial instantaneous and average Poynting vector, 1 m away from the feed point of a $1.24 \text{ m} \times 0.004 \text{ m}$ dipole antenna immersed in plasma density of $1.24 \times 10^6 \text{ 1/cc}$ ($f_p = 10 \text{ MHz}$).

of all of the density and velocity (kinetic energy) variations. It is also worth noting that shy of the DC EM energy propagation, the parallel EM energy is of the same order as the kinetic energy. This is not true for the perpendicular propagation.

Finally, a general study of figs. 3.14 - 3.16 reveals that there appears to be some form of energy propagation that violates the quasi-static assumptions made in the analytical methods. The frequency spectrum of this energy propagation matches the frequencies in which there is a disagreement between the PF-FDTD and Balmain, see fig. 3.9.

It should also be noted that these results were obtained using a naturally resorting drive source. If a nonnaturally restoring source is used there will be other variations as a sheath is built around the antenna.

3.4 Magnetized Plasma with an Incident Angle of Zero

The addition of a magnetic field drastically affects the characteristic impedance curve of an antenna in plasma. Any drive signal applied to the antenna will stimulate the plasma, introducing a $\vec{V} \times \vec{B}$ drift. This movement of electrons can then transport energy away from the antenna. As this energy is radiated, the results can be seen in the input impedance of the antenna, see figs. 3.17 and 3.18. In addition, the gyro resonance also couples with

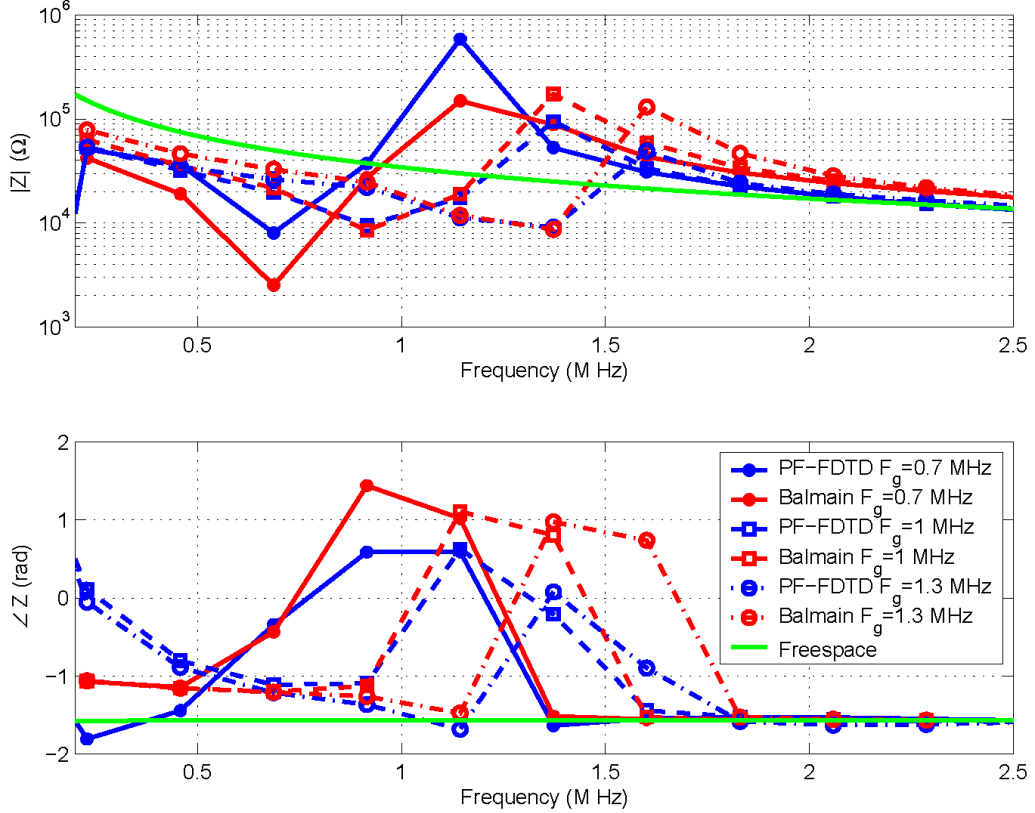


Fig. 3.17: The PF-FDTD versus Balmain for a $1.24 \text{ m} \times 0.004 \text{ m}$ dipole for various weak magnetic field strengths with a plasma density of $1.24 \times 10^4 \text{ 1/cc}$ ($f_p = 1 \text{ MHz}$). The PF-FDTD ran for 2^{16} iterations, 4 plasma cycles.

the plasma resonance to create an upper hybrid frequency ($\omega_{uh}^2 = \omega_p^2 + \Omega^2$). This upper hybrid frequency effectively extends the plasma physics to higher frequencies, as it replaces the plasma frequency as the plasma cut-off point. The combination of all of these factors introduces two new distinct features in the impedance curve. A series resonance located at the gyro frequency and a parallel resonance located at the upper hybrid.

Figures 3.17 and 3.18, also show the reduced frequency resolution associated with simulating smaller plasma properties for a fixed number of iterations. While this resolution is not necessary around the series resonance of the gyro frequency, it does aid in understanding the nature of the upper hybrid. In addition, figs. 3.17 and 3.18, show the two main cases of plasma conditions $\omega_p > \Omega$ and $\omega_p < \Omega$.

The presence of the magnetic field also introduces a preferential direction for the flow of

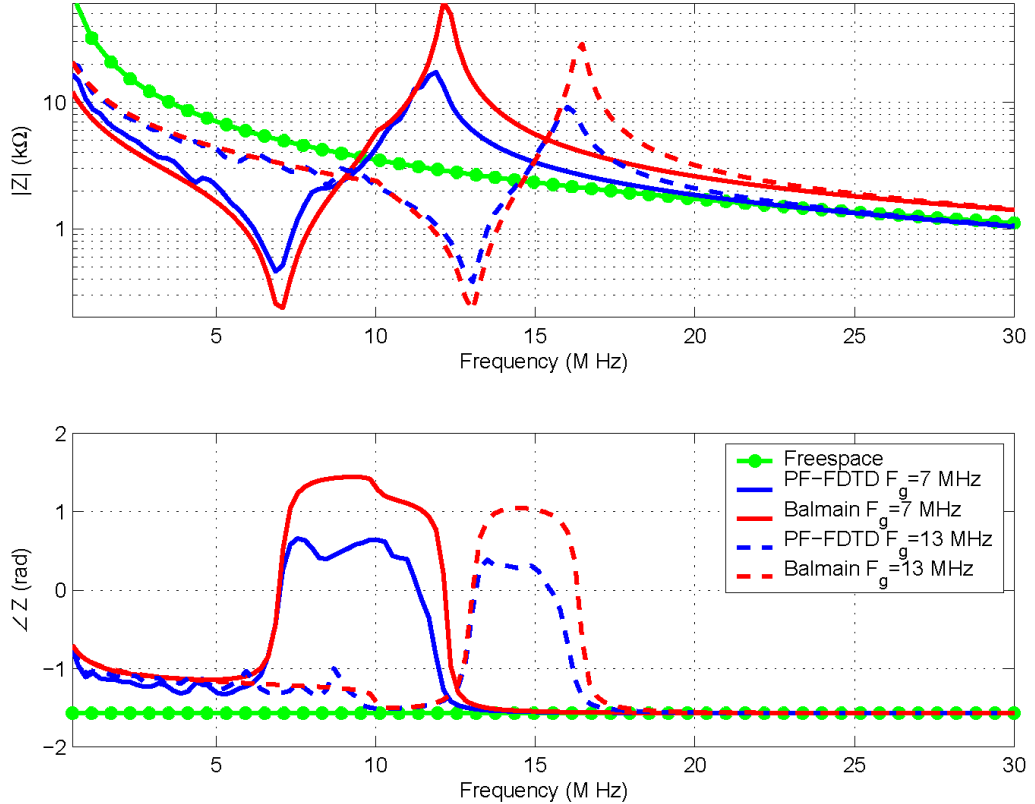


Fig. 3.18: The PF-FDTD versus Balmain for a $1.24 \text{ m} \times 0.004 \text{ m}$ dipole with a plasma density of $1.24 \times 10^6 \text{ 1/cc}$ ($f_p = 10 \text{ MHz}$) and two magnetic fields. The PF-FDTD ran for 2^{16} iterations, 40 plasma cycles.

plasma, as charged particles easily travel along magnetic field lines. However, the movement is confined to frequencies on the order of the gyro frequency because of the ease at which charged particle can travel on magnetic field lines. This ease of mobility also decreases the overall resistance seen at the probe terminals, as energy is effectively radiated away from the antenna, see figs. 3.17 and 3.18. While the dip in resistance primarily occurs at the gyro frequency, it has a dispersive effect caused as the plasma collides with other particles that increase or decrease the effective oscillation path of the plasma.

In addition to creating the gyro resonance, the presence of a DC magnetic field also modifies the plasma oscillation within the plane perpendicular to the magnetic field. This upper hybrid becomes the dominate “high frequency” mode within the plasma, significantly effecting the plasma and cyclotron resonances. However, the fact that the upper hybrid

remains an oscillation as opposed to a wave implies that any energy applied to the plasma near the upper hybrid frequency will be reactively coupled into the plasma. This yields a highly resistive resonance condition at the upper hybrid, similar to the plasma frequency of the nonmagnetized case.

3.4.1 Plasma Frequency > Cyclotron Frequency

For ionospheric measurements within the F-region and most laboratory experiments, the plasma density is high enough to cause the plasma resonance to exceed the cyclotron frequency. In these cases, the presence of the magnetic field causes the upper hybrid oscillation to become more dominate than the plasma oscillation. This can best be seen by the fact that the plasma resonance cannot be identified in $|Z|$ for figs. 3.17 and 3.18. However, the plasma resonance effects do not completely disappear as there still remains a significant phase variation centered around the plasma resonance, see from 9 MHz to 10 MHz in fig. 3.18 for the $f_g = 7$ MHz. Figures 3.17 and 3.18 also show that as both the plasma and upper hybrid are relatively far away from the gyro resonance, the limited band of radiation at the gyro frequency has little effect on the reactive nature of the plasma and upper hybrid. As the plasma frequency approaches the gyro resonance, the radiative nature of the gyro frequency becomes more dominate and the plasma frequency effects are muted even more.

Current Distributions

The current distributions in magnetized plasma show a result similar to that seen when the nonmagnetized plasma case was present. Specifically $|I(l)|$ entering the upper hybrid is very similar to the current distribution entering the plasma resonance with no magnetic field, see figs. 3.19 - 3.21. The presence of the attenuating wave along the antenna shows that energy is being reactively coupled near the feed point. As the drive frequency begins to match the plasma resonance, the traveling wave becomes superimposed upon the attenuation wave, causing the peak in $|I(l)|$ to move off the feed point. The combination of these two current distributions continues until just below 1/2 of the cut-off frequency, the upper hybrid frequency for a magnetized plasma (see figs. 3.22 and 3.25). This is similar

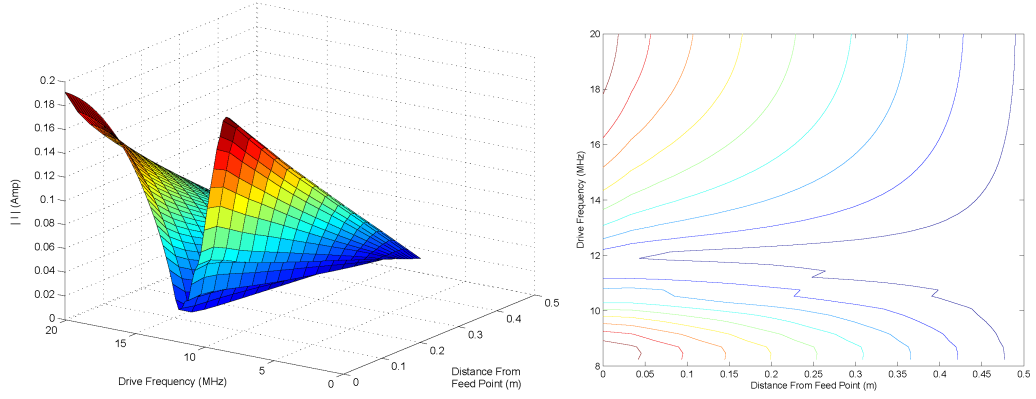


Fig. 3.19: The magnitude of the current distribution along a $1.24 \text{ m} \times 0.004 \text{ m}$ dipole antenna immersed in plasma density of $1.24 \times 10^6 \text{ 1/cc}$ ($f_p = 10 \text{ MHz}$) with a magnetic field of $2.5 \times 10^{-4} \text{ Tesla}$ ($f_g = 7 \text{ MHz}$) for various drive frequencies near the upper hybrid resonance.

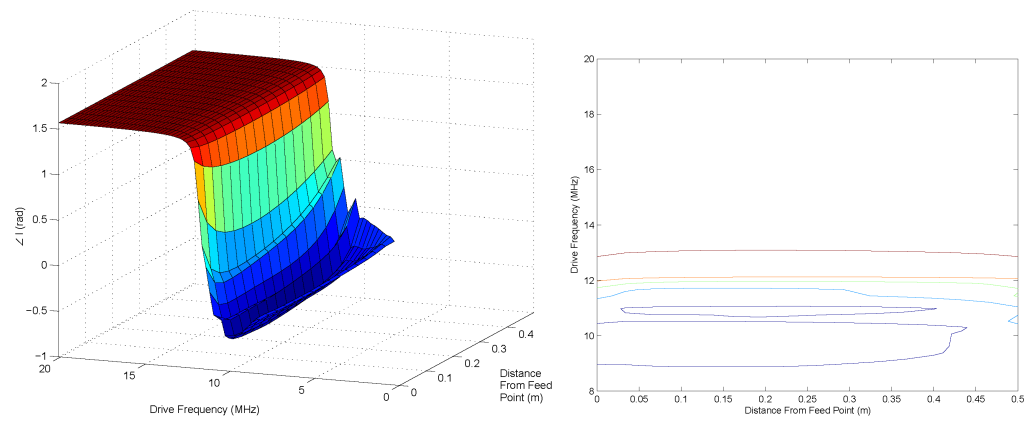


Fig. 3.20: The phase of the current distribution along a $1.24 \text{ m} \times 0.004 \text{ m}$ dipole antenna immersed in plasma density of $1.24 \times 10^6 \text{ 1/cc}$ ($f_p = 10 \text{ MHz}$) with a magnetic field of $2.5 \times 10^{-4} \text{ Tesla}$ ($f_g = 7 \text{ MHz}$) for various drive frequencies near the upper hybrid resonance. The drive voltage is set to zero phase.

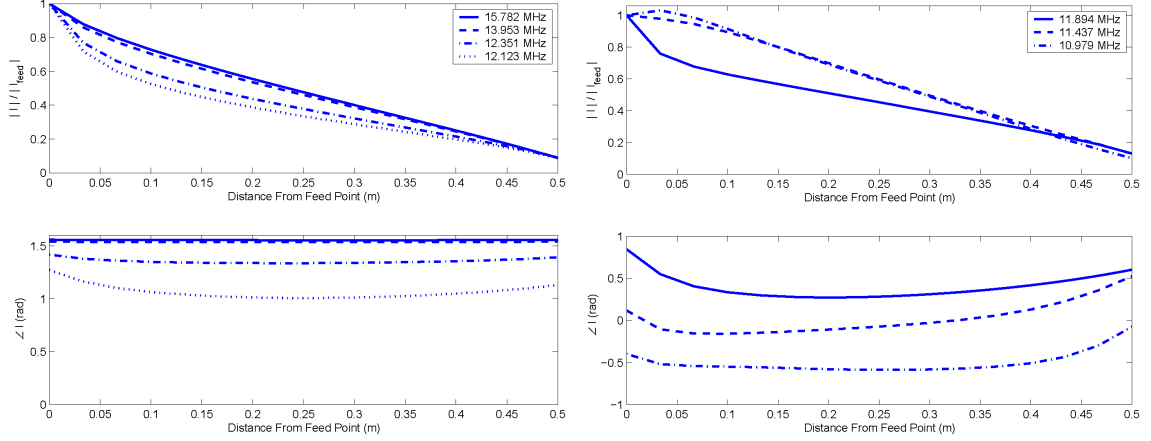


Fig. 3.21: The magnitude and phase of the current distribution along a $1.24 \text{ m} \times 0.004 \text{ m}$ dipole antenna immersed in plasma density of $1.24 \times 10^6 \text{ 1/cc}$ ($f_p = 10 \text{ MHz}$) with a magnetic field of $2.5 \times 10^{-4} \text{ Tesla}$ ($f_g = 7 \text{ MHz}$) for a select few drive frequencies around the upper hybrid frequency. The drive voltage is set to zero phase and the actual $f_{uh} = 12.207 \text{ MHz}$.

to what was seen in the nonmagnetized case.

The combination of the traveling and attenuation wave current distributions also cause the phase to transition. At the “high” frequencies $\angle I(l)$ behaves in a similar way to the nonmagnetized case, in that a dip appears that eventually drags all of the phase into the inductive realm. However, in the magnetized plasma, the location of this minimum phase point is different than the nonmagnetized case. In the nonmagnetized case the dip started and stayed at approximately 0.07 meters out from the feed point (see section 3.3). In the magnetized case the dip appears around 0.25 meters and decreases to 0.07 meters as the frequency approach the plasma frequency, see figs. 3.21-3.22. In fact, it appears as if the dip move towards the nonmagnetized case location, as the drive frequencies approaches the plasma frequency. However, once the drive frequency is just above the plasma frequency, the location of the dip becomes constant as the remainder of the probe reaches the same phase value. These frequencies coincide with the presence of a “step” in $\angle Z$, a region in-between the plasma and upper hybrid frequencies (fig. 3.18). What occurs at these frequencies is still somewhat of a mystery. However, a similar feature was seen and recorded in an experiment performed at the Air Force Research Lab (AFRL) in Bedford Massachusetts (see Chapter 4). Once past this “step,” the dip in $\angle I(l)$ begins to pull the phase negative

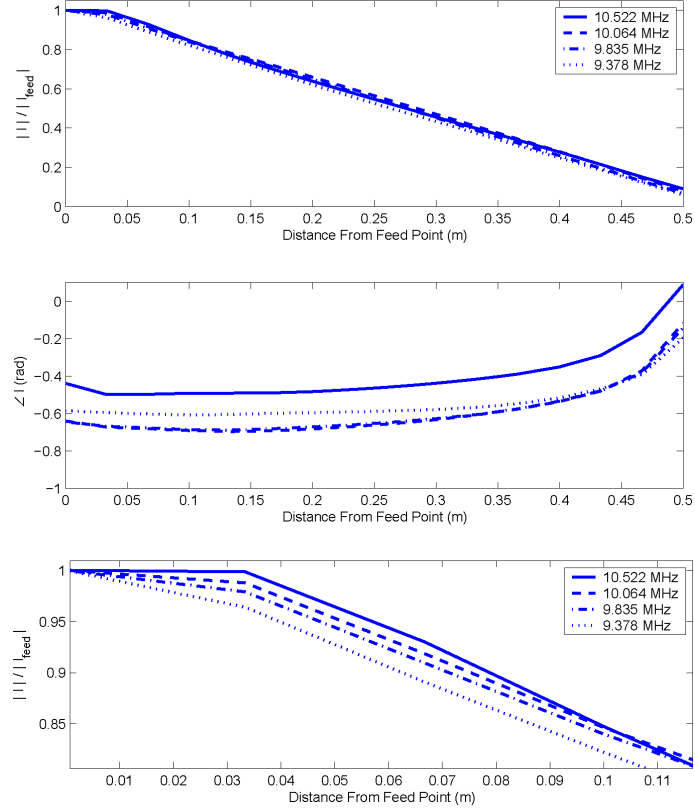


Fig. 3.22: The magnitude and phase of the current distribution along a $1.24 \text{ m} \times 0.004 \text{ m}$ dipole antenna immersed in plasma density of $1.24 \times 10^6 \text{ 1/cc}$ ($f_p = 10 \text{ MHz}$) with a magnetic field of $2.5 \times 10^{-4} \text{ Tesla}$ ($f_g = 7 \text{ MHz}$) for a select few drive frequencies around the plasma frequency. The drive voltage is set to zero phase. Note: The bottom graph is a close up of the magnitude near the feed point.

again, as the drive frequency finally reaches the plasma resonance. However, this time the location of the dip does not move. In fact, it remains near the nonmagnetized point.

One of the most important aspects of the above observations is that $\angle Z = 0$, which has traditionally been attributed to the upper hybrid, does not actually coincide with the spike in $|Z|$. In fact it appears as if for magnetized plasma, the probe geometry has a significant effect on where this zero phase point occurs, even more so than the nonmagnetized plasma case. It is the probes' geometry that determines how long it takes the descending dip in fig. 3.21 to yield $\angle I(l=0) \Rightarrow 0$.

Once below $1/2$ of cut-off frequency, $|I(l)|$ returns to purely triangular in nature and $\angle I(l)$ becomes relatively constant along the antenna, see figs. 3.23-3.25. This is especially

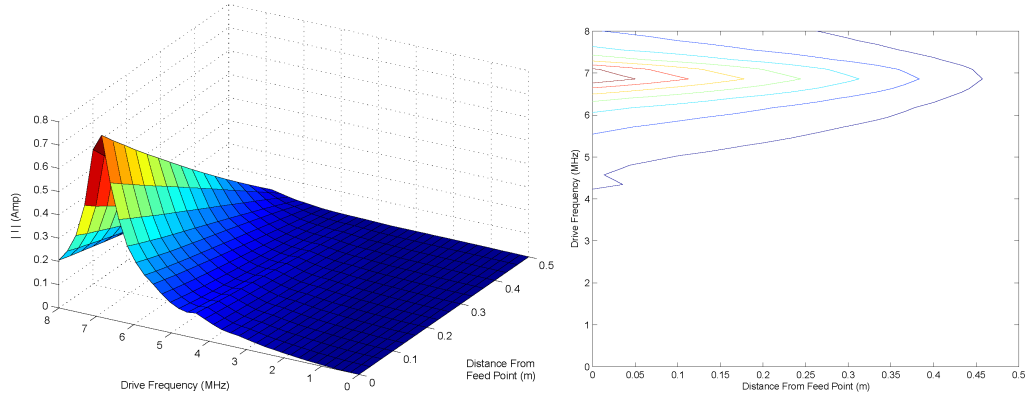


Fig. 3.23: The magnitude of the current distribution along a $1.24 \text{ m} \times 0.004 \text{ m}$ dipole antenna immersed in plasma density of $1.24 \times 10^6 \text{ 1/cc}$ ($f_p = 10 \text{ MHz}$) with a magnetic field of $2.5 \times 10^{-4} \text{ Tesla}$ ($f_g = 7 \text{ MHz}$) for various drive frequencies near the gyro resonance.

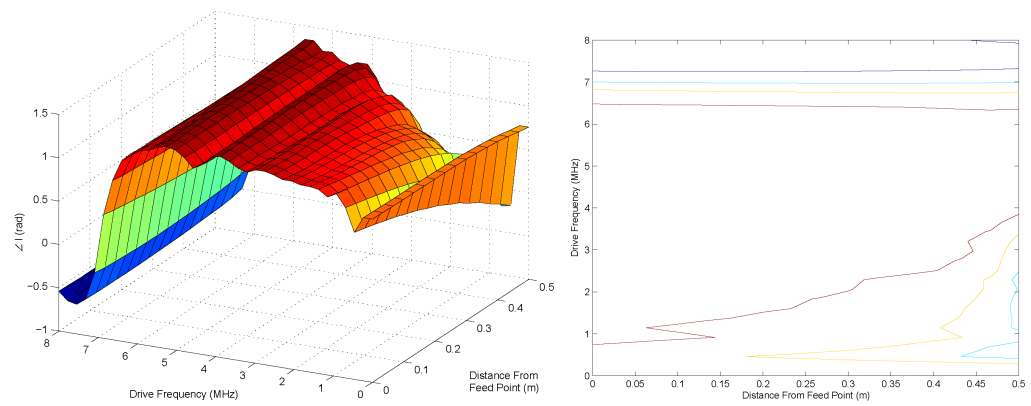


Fig. 3.24: The phase of the current distribution along a $1.24 \text{ m} \times 0.004 \text{ m}$ dipole antenna immersed in plasma density of $1.24 \times 10^6 \text{ 1/cc}$ ($f_p = 10 \text{ MHz}$) with a magnetic field of $2.5 \times 10^{-4} \text{ Tesla}$ ($f_g = 7 \text{ MHz}$) for various drive frequencies near the gyro resonance. The drive voltage is set to zero phase.

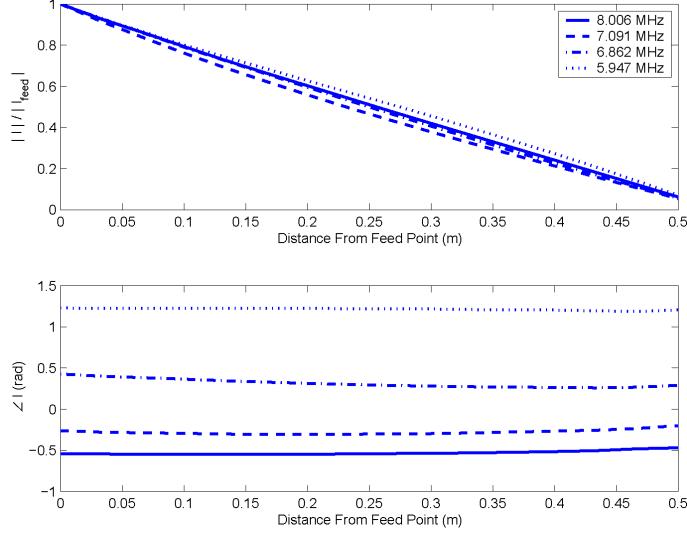


Fig. 3.25: The magnitude and phase of the current distribution along a $1.24 \text{ m} \times 0.004 \text{ m}$ dipole antenna immersed in plasma density of $1.24 \times 10^6 \text{ 1/cc}$ ($f_p = 10 \text{ MHz}$) with a magnetic field of $2.5 \times 10^{-4} \text{ Tesla}$ ($f_g = 7 \text{ MHz}$) for a select few drive frequencies around the gyro frequency. The drive voltage is set to zero phase.

true around the gyro resonance, as the presence of the magnetic field enables a mode of energy propagation. This energy mode can easily be stimulated, resulting in a relatively low impedance and high feed current.

Once below the cyclotron frequency there appear to be multiple effects that cause the phase to vary along the length of the antenna. These effects are still being investigated and no conclusive results have been obtained. Some of these effects may be the remains of the antenna boundary resonance cavity discussed in section 3.3.

Energy Flows

When a magnetic field is added to the plasma, the field and energy variations remain somewhat similar to the nonmagnetized plasma case, see figs. 3.26-3.28. There still remain the temporal fluctuations that can be related to the EM waves and the evanescent “plasma waves” and these variations occur in limited frequency bands. However, there are also some significant differences. The largest being that the majority of the energy is transmitted in the EM waves as opposed to a 50 % EM/50 % kinetic split in the nonmagnetized plasma.

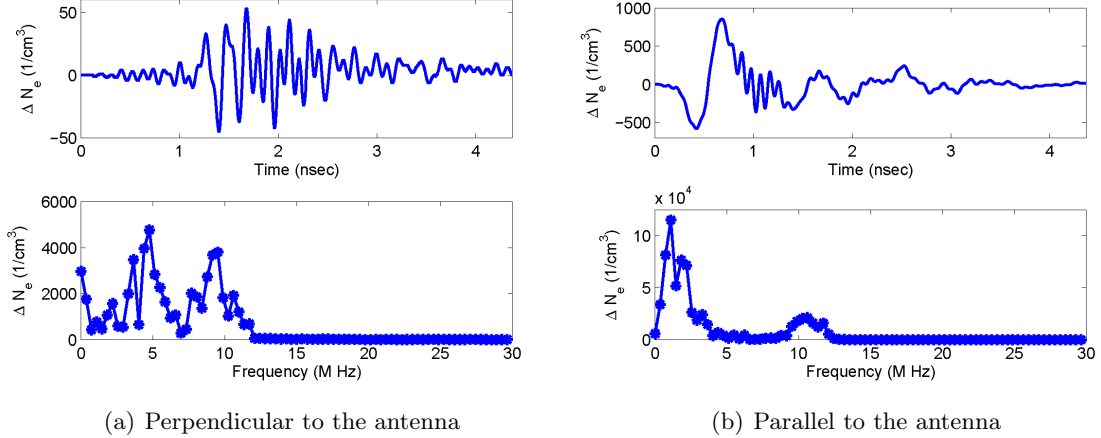


Fig. 3.26: Fluctuations in the electron density 1 m away from the feed point of a $1.24 \text{ m} \times 0.004 \text{ m}$ dipole antenna emersed in plasma density of $1.24 \times 10^6 \text{ 1/cc}$ ($f_p = 10 \text{ MHz}$) with a magnetic field of $2.5 \times 10^{-4} \text{ Tesla}$ ($f_g = 7 \text{ MHz}$).

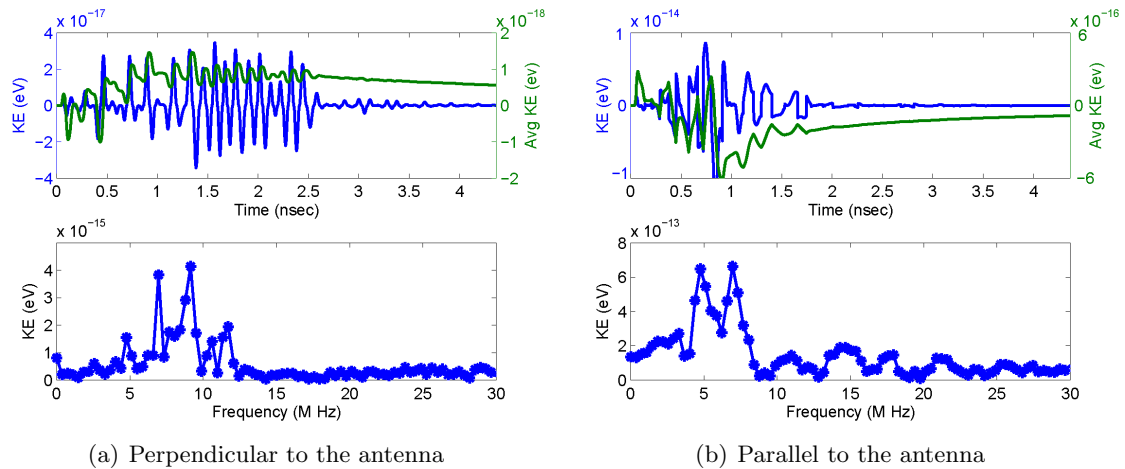


Fig. 3.27: Fluctuations in the radial instantaneous and average kinetic energy 1 m away from the feed point of a $1.24 \text{ m} \times 0.004 \text{ m}$ dipole antenna immersed in plasma density of $1.24 \times 10^6 \text{ 1/cc}$ ($f_p = 10 \text{ MHz}$) with a magnetic field of $2.5 \times 10^{-4} \text{ Tesla}$ ($f_g = 7 \text{ MHz}$).

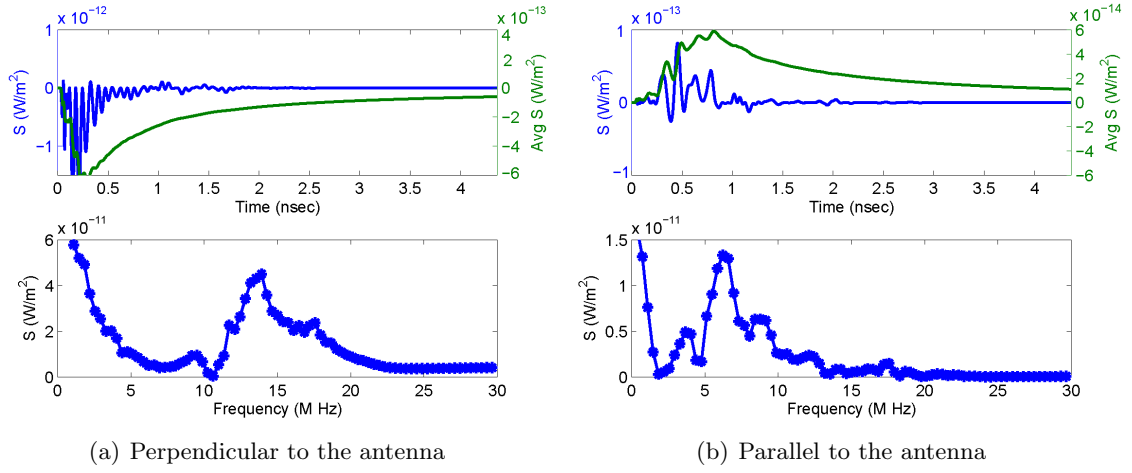


Fig. 3.28: Fluctuations in the radial instantaneous and average Poynting vector 1 m away from the feed point of a $1.24 \text{ m} \times 0.004 \text{ m}$ dipole antenna immersed in plasma density of $1.24 \times 10^6 \text{ 1/cc}$ ($f_p = 10 \text{ MHz}$) with a magnetic field of $2.5 \times 10^{-4} \text{ Tesla}$ ($f_g = 7 \text{ MHz}$).

The density variations also show the effects of the parallel magnetic field. Perpendicular to the antenna, at point \mathcal{A} , there are bands of density variations that exist from $1/2$ to 1 times the upper hybrid frequency, $1/2$ to 1 times the plasma frequency, and over the harmonic combination of the two frequencies (down to $f_{uh} - f_p$, 2.2 MHz). However, there is a distinct notch in the density variations at the gyro frequency. This notch at the gyro frequency is also noted at \mathcal{B} . These notches are most likely due to the relative ease that electrons have at moving along field lines, at the gyro frequency, to fill any possible void in the overall electron density. Point \mathcal{B} also shows a large temporal flow of particles along the same field line as the antenna that coincides almost directly with the time variations of the source, as electrons immediately try to respond.

The perpendicular kinetic energy, at point \mathcal{A} , also exhibits the presence of energy being reactively stored within the regions of $1/2$ to 1 times the plasma frequency and $1/2$ to 1 times the upper hybrid frequency. The parallel component, at point \mathcal{B} , also shows some form of energy propagation/radiation as the kinetic energy between $1/2$ and 1 f_g does not appear to be stored. This would imply that the energy is being conducted along field lines. This radiated energy on average appears to be three times that of any radiated energy in the nonmagnetized case.

As previously stated, the biggest difference between magnetized and nonmagnetized cases can be seen in the Poynting vector. The presence of the gyro frequency, dominates the EM spectrum at point \mathcal{B} as energy is conducted along field lines. It is also easy to see the effects that the other plasma oscillations have on the parallel component. However, the difference between the magnetized and nonmagnetized EM spectrum at point \mathcal{A} is somewhat unexplainable. There is a distinctive damping of the Poynting vector at the various plasma critical frequencies. Nevertheless, to date there is no explanation as to the large increase in the perpendicular Poynting vector just above the upper hybrid.

3.4.2 Plasma Frequency < Cyclotron Frequency

Not all plasma conditions dictate that the plasma frequency must be greater than the cyclotron. It is very common within the D and E regions of the ionosphere for the gyro frequency to be greater than the plasma frequency. When this occurs, there is a significant shift in the characteristic nature of the input impedance of an RF probe. Figs. 3.17 and 3.18 show the effects, namely that the transition between the parallel and series resonances occur at a faster rate, as the frequencies between the reactive upper hybrid and the resistive gyro decrease in numbers.

Current Distributions

The magnitude of the current distribution in the case of $\omega_p < \Omega$ is very similar to the $\omega_p > \Omega$ cases, see figs. 3.29 and 3.31. There are dips around both the upper hybrid and plasma resonances, and a spike near the cyclotron frequency. Also the region around the upper hybrid is dominated by the attenuated current distribution, as the energy is reactively coupled. $|I(l)|$ then changes around the cyclotron and remains dominated by the traveling distribution, as energy is radiated away.

The phase of the current distribution, see figs. 3.30 -3.31, also begins to dip when the drive frequency drops below the upper hybrid and continues until just above the gyro frequency where it becomes a constant along the whole length of the antenna. $\angle I(l)$ then remains constant until the plasma frequency is reached, at which time it begins to vary

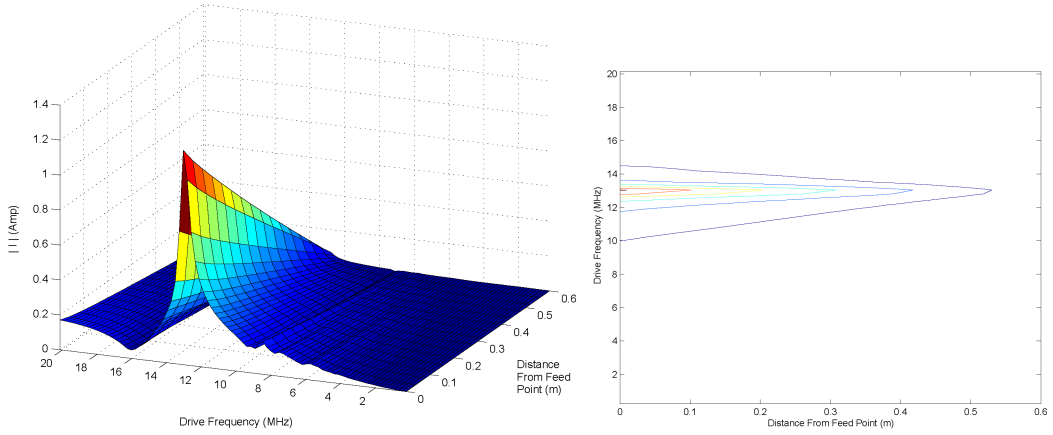


Fig. 3.29: The magnitude of the current distribution along a $1.24 \text{ m} \times 0.004 \text{ m}$ dipole antenna immersed in plasma density of $1.24 \times 10^6 \text{ 1/cc}$ ($f_p = 10 \text{ MHz}$) with a magnetic field of $4.6 \times 10^{-4} \text{ Tesla}$ ($f_g = 13 \text{ MHz}$) for various drive frequencies.

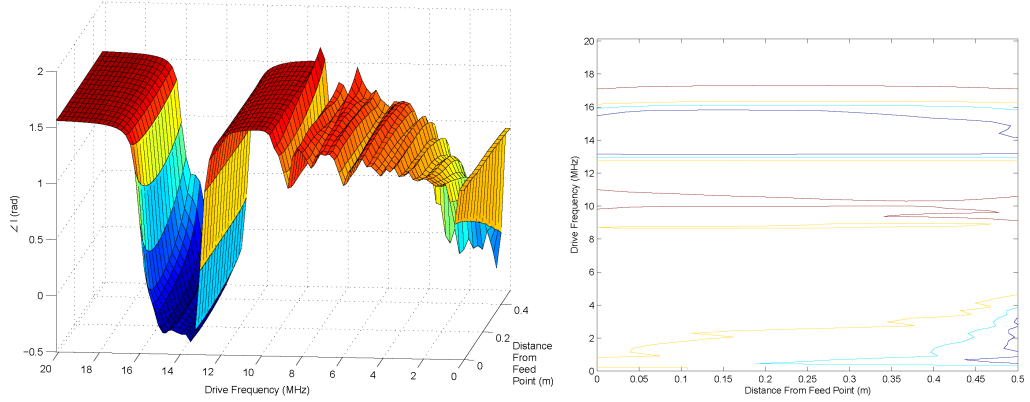


Fig. 3.30: The phase of the current distribution along a $1.24 \text{ m} \times 0.004 \text{ m}$ dipole antenna immersed in plasma density of $1.24 \times 10^6 \text{ 1/cc}$ ($f_p = 10 \text{ MHz}$) with a magnetic field of $4.6 \times 10^{-4} \text{ Tesla}$ ($f_g = 13 \text{ MHz}$) for various drive frequencies. The drive voltage is set to zero phase.

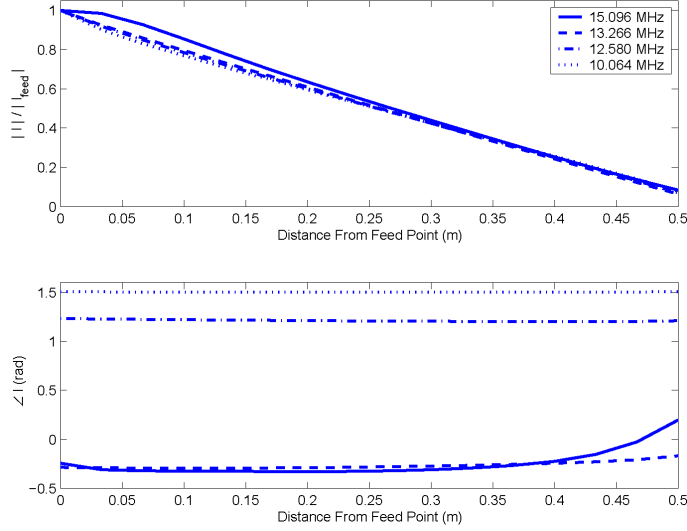


Fig. 3.31: The magnitude and phase of the current distribution along a $1.24 \text{ m} \times 0.004 \text{ m}$ dipole antenna immersed in plasma density of $1.24 \times 10^6 \text{ 1/cc}$ ($f_p = 10 \text{ MHz}$) with a magnetic field of $4.6 \times 10^{-4} \text{ Tesla}$ ($f_g = 13 \text{ MHz}$) for a select few drive frequencies. The drive voltage is set to zero phase.

again. The exact cause of these low frequency variations is still somewhat unknown, but is most likely due to the harmonics of the various plasma resonance conditions.

It is also interesting to point out, that in the region where $I(l)$ is purely a traveling wave with a constant phase (frequencies between the gyro and plasma frequencies), the PF-FDTD matches the analytical model of Balmain exactly, see fig. 3.18.

Energy Flows

When the gyro frequency is increased above the plasma, the features in the field components attributed to the gyro frequency also increase in frequency, see figs. 3.32-3.34. The density continues to vary over the $1/2$ to 1 times f_p and f_{uh} frequency ranges and remain constant at the gyro frequency. The kinetic energy also sees a increase at the gyro frequency. However, the physics behind the multiple spikes in the radial energy measured at \mathcal{B} remains unknown. The same is somewhat true for the radial Poynting vector at \mathcal{A} and \mathcal{B} . The perpendicular Poynting vector experiences the same increase above the upper hybrid and damping around the critical plasma frequencies, while the parallel Poynting vector sees the spike at the gyro frequency in addition to unknown others.

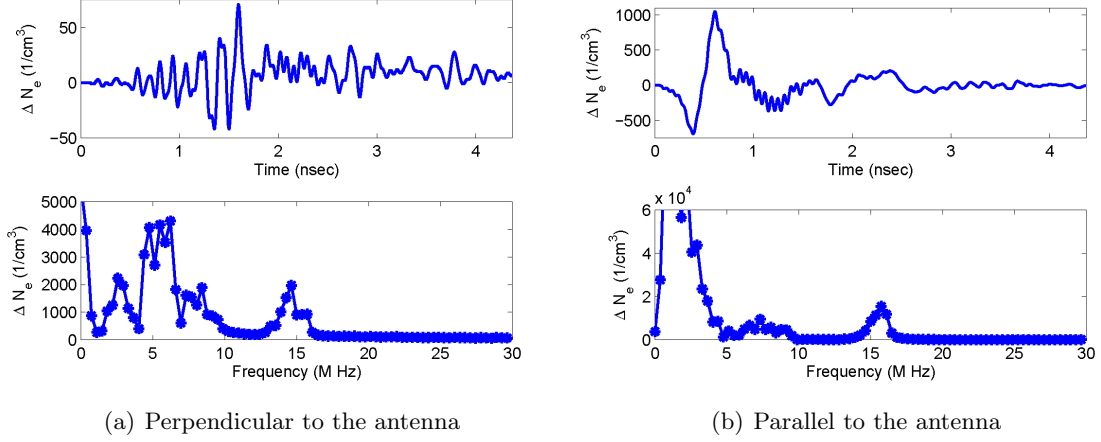


Fig. 3.32: Fluctuations in the electron density 1 m away from the feed point of a $1.24 \text{ m} \times 0.004 \text{ m}$ dipole antenna immersed in plasma density of $1.24 \times 10^6 \text{ 1/cc}$ ($f_p = 10 \text{ MHz}$) with a magnetic field of $4.6 \times 10^{-4} \text{ Tesla}$ ($f_g = 13 \text{ MHz}$).

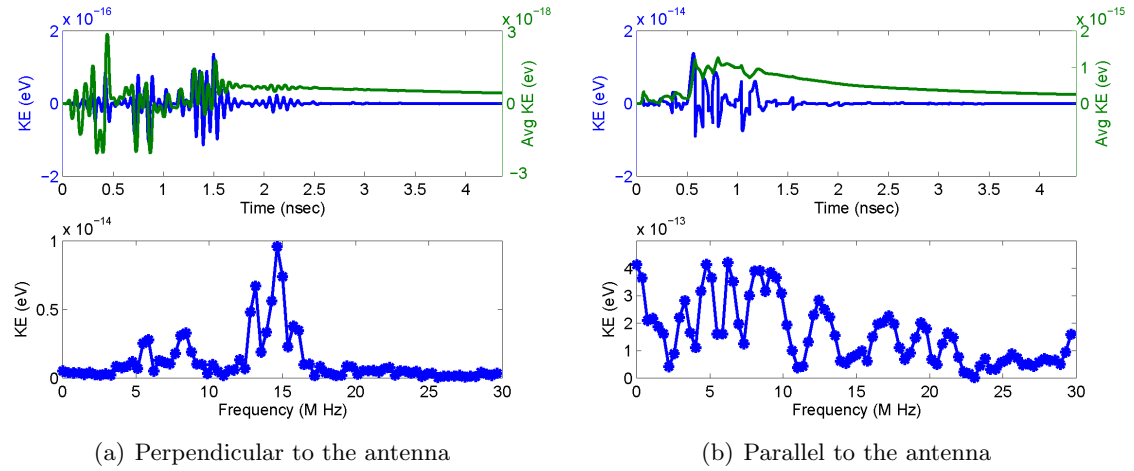


Fig. 3.33: Fluctuations in the radial instantaneous and average kinetic energy 1 m away from the feed point of a $1.24 \text{ m} \times 0.004 \text{ m}$ dipole antenna immersed in plasma density of $1.24 \times 10^6 \text{ 1/cc}$ ($f_p = 10 \text{ MHz}$) with a magnetic field of $4.6 \times 10^{-4} \text{ Tesla}$ ($f_g = 13 \text{ MHz}$).

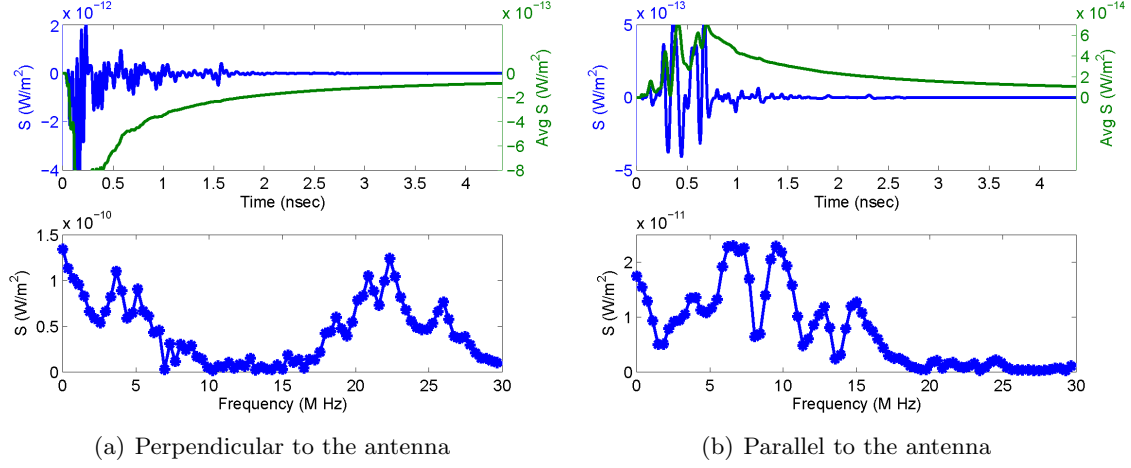


Fig. 3.34: Fluctuations in the radial instantaneous and average Poynting vector 1 m away from the feed point of a $1.24 \text{ m} \times 0.004 \text{ m}$ dipole antenna immersed in plasma density of $1.24 \times 10^6 \text{ 1/cc}$ ($f_p = 10 \text{ MHz}$) with a magnetic field of $4.6 \times 10^{-4} \text{ Tesla}$ ($f_g = 13 \text{ MHz}$).

3.5 Magnetized Plasma with Various Incident Angles

The incident angle of the magnetic field effects the input impedance of an antenna, as the antenna slices through additional conductive field lines. For example, if the magnetic field is parallel to a dipole, any electron trying to match the driving current can follow along the magnetic field lines. This decreases the amount of energy required to move electrons at the gyro frequency, thereby decreasing the overall impedance seen around the cyclotron resonance. The opposite is true for the upper hybrid resonances since its oscillations are perpendicular to the magnetic field. Because of the orthogonal nature of the antenna current and these perpendicular oscillations, any transfer of energy must be done at great cost. This results in a high impedance. If the magnetic field incident angle is rotated 90 degrees, the opposite is true. There is an increase in the resistive part of the cyclotron resonance and a decrease in the upper hybrid. Similar arguments can also be applied to any incident angle between 0 and 90 degrees.

3.5.1 Plasma Frequency > Cyclotron Frequency

Figure 3.35 demonstrates the effect that a 90-degree incident angle would have on an antenna verses a zero degree incident angle. As mentioned above, the aligning of the field

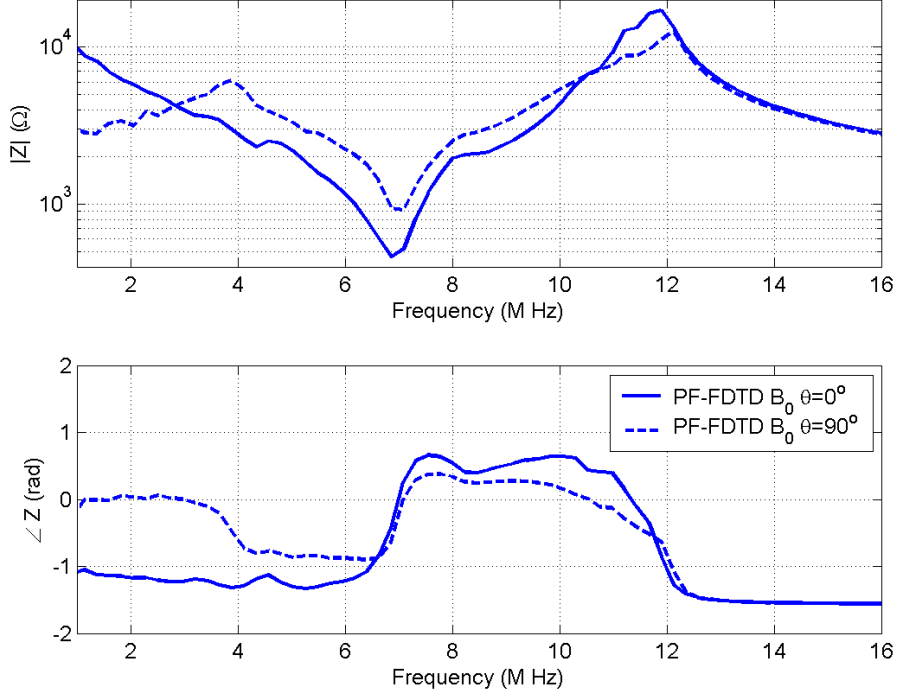


Fig. 3.35: The PF-FDTD versus Balmain for a $1.24 \text{ m} \times 0.004 \text{ m}$ dipole for various magnetic field incident angles with a plasma density of $1.24 \times 10^4 \text{ 1/cc}$ ($f_p = 1 \text{ MHz}$) and a magnetic field of $2.5 \times 10^{-4} \text{ Tesla}$ ($f_g = 7 \text{ MHz}$). The PF-FDTD ran for 2^{16} iterations, 40 plasma cycles.

lines with the flow of current along the antenna can either enhance or diminish the effects of the gyro and upper hybrid resonances. In addition, there is also a substantial shifting of the “upper hybrid” zero phase crossing, between the two incident angles. This shifting of the zero crossing is strongly dependent upon the phase of the current distribution and the antenna geometry and how they map to the magnetic field lines. However, the most prominent effect of varying the incident angle occurs below the gyro frequency, as its effects are damped due to the decreased coupling. This variation also appears to be amplified at frequencies below the $1/2f_p$ frequency, easily spotted in the $\theta = 0$ case by the small variation in $|Z|$ and $\angle Z$ around 5 MHz. Above the $1/2f_p$ frequency, the near field damping effect of the plasma minimize the effects of the increased number of incident magnetic field lines. Below the $1/2f_p$, the additional incident magnetic field lines ease the flow of the electrons,

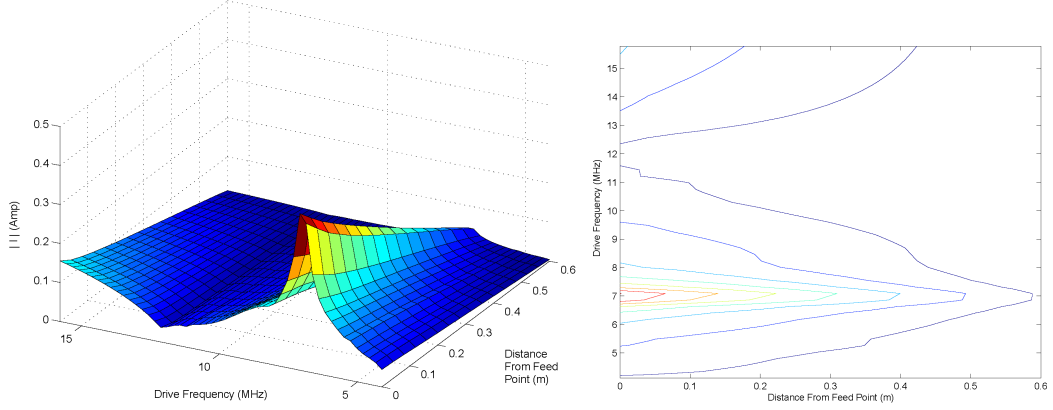


Fig. 3.36: The magnitude of the current distribution along a $1.24 \text{ m} \times 0.004 \text{ m}$ dipole antenna immersed in plasma density of $1.24 \times 10^6 \text{ 1/cc}$ ($f_p = 10 \text{ MHz}$) with a magnetic field of $2.5 \times 10^{-4} \text{ Tesla}$ ($f_g = 7 \text{ MHz}$) at an incident angle of 90° for various drive frequencies.

decreasing the reactive part of Z .

Current Distributions

The current distribution remains relatively similar to that of the zero degree incident magnetic field case for frequencies above $1/2 f_p$ (compare figs. 3.36 and 3.37 to figs. 3.19-3.24). However, there is a gradual delay in the $\angle I(l=0) \Rightarrow 0$ point, around the upper hybrid, as the dip in the $\angle I(l)$ takes longer to progress to the nonmagnetized value. This is also evidenced by the slower $\angle Z$ transition at the upper hybrid, which blurs the minor features of the plasma frequency.

The additional low frequency impedance variations can also be seen in the current distribution, see figs. 3.38 and 3.39. While these variations are small in $|I(l)|$, there are significant fluctuations in $\angle I(l)$. These phase variations also appear to show the presence of a similar dip, as seen around the cut-off frequency. However, additional resolution is needed at these frequencies in order to properly analyze the plasma effects.

Energy Flows

The field values also show significant variation between a perpendicular DC magnetic field and a parallel DC magnetic field. However it becomes difficult to perform a one to

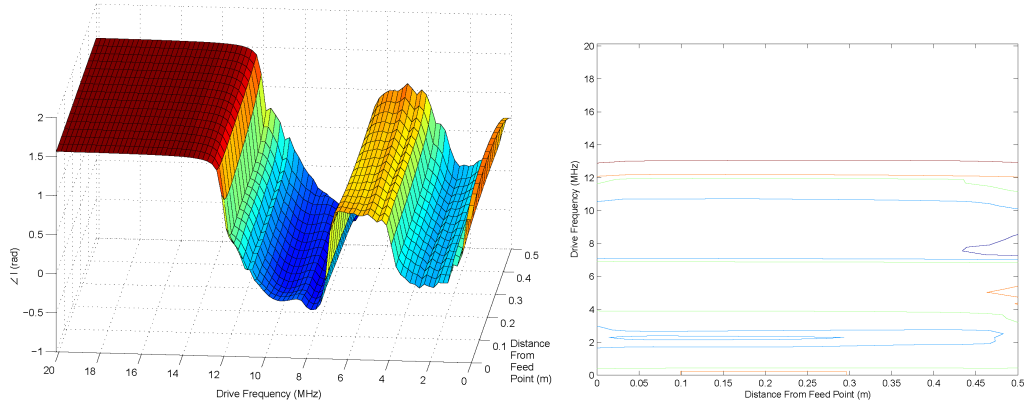


Fig. 3.37: The phase of the current distribution along a $1.24 \text{ m} \times 0.004 \text{ m}$ dipole antenna immersed in plasma density of $1.24 \times 10^6 \text{ 1/cc}$ ($f_p = 10 \text{ MHz}$) with a magnetic field of $2.5 \times 10^{-4} \text{ Tesla}$ ($f_g = 7 \text{ MHz}$) at an incident angle of 90° for various drive frequencies. The drive voltage is set to zero phase.

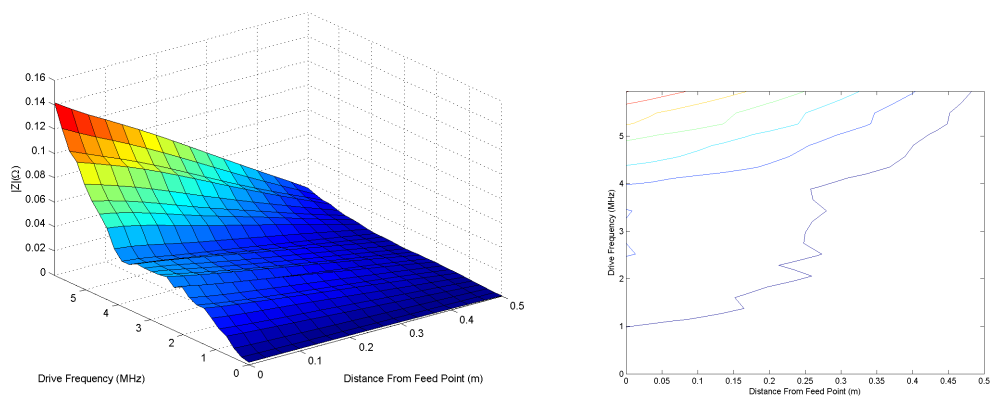


Fig. 3.38: The magnitude of the current distribution along a $1.24 \text{ m} \times 0.004 \text{ m}$ dipole antenna immersed in plasma density of $1.24 \times 10^6 \text{ 1/cc}$ ($f_p = 10 \text{ MHz}$) with a magnetic field of $2.5 \times 10^{-4} \text{ Tesla}$ ($f_g = 7 \text{ MHz}$) at an incident angle of 90° for drive frequencies below $1/2f_p$.

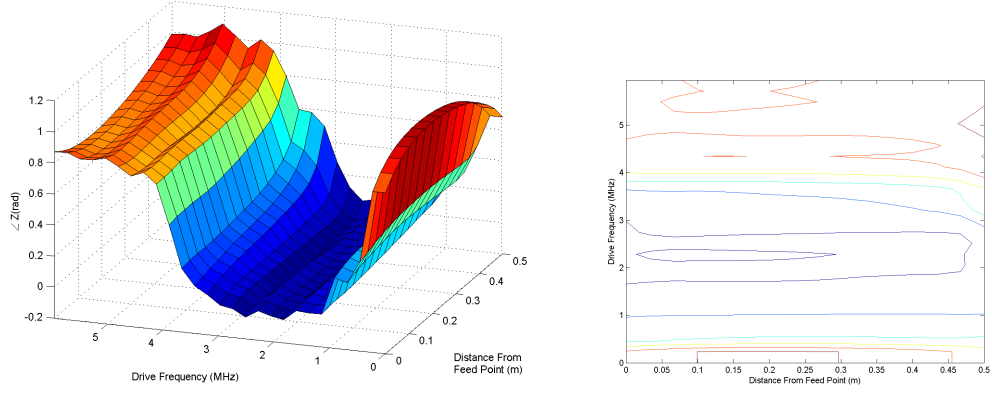


Fig. 3.39: The phase of the current distribution along a $1.24 \text{ m} \times 0.004 \text{ m}$ dipole antenna immersed in plasma density of $1.24 \times 10^6 \text{ 1/cc}$ ($f_p = 10 \text{ MHz}$) with a magnetic field of $2.5 \times 10^{-4} \text{ Tesla}$ ($f_g = 7 \text{ MHz}$) at an incident angle of 90° for drive frequencies below $1/2f_p$. The drive voltage is set to zero phase.

one comparison between them (compare figs. 3.40 and 3.42 to figs. 3.26-3.28) The specific highlights are

1. The density measured in fig. 3.40 at \mathcal{A} sees the “plasma waves” at an early time than the same point in fig. 3.26 (0.5 n sec as opposed to $> 1 \text{ n sec}$). This is due to the conductive nature of the magnetic field lines.
2. As the antenna can now stimulate plasma along multiple magnetic field lines and accelerate the plasma across field lines along the antennas surface, both the velocity and density near field at \mathcal{A} and \mathcal{B} look relatively the same.
3. Traditional free-space radiation pattern for an electrically short dipole are basically a broadside pattern (the EM fields are strongest perpendicular to the antenna). When this broadside radiation pattern aligns with the magnetic field, the Poynting vector takes on the characteristics of the nonmagnetized case (fig. 3.16).

3.5.2 Plasma Frequency < Cyclotron Frequency

As the plasma frequency is dropped below the cyclotron, the input impedance behaves as expected. The magnitude of input impedance at the upper hybrid resonance decreases,

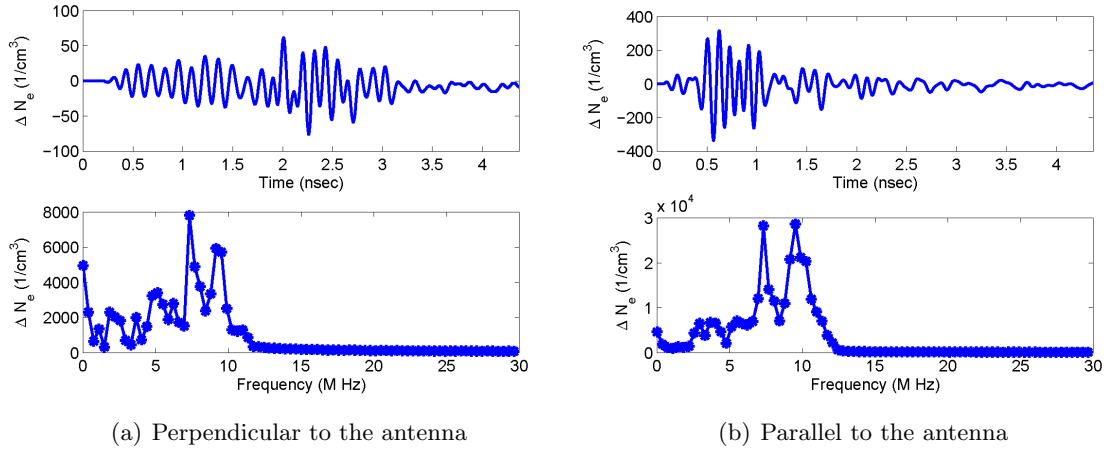


Fig. 3.40: Fluctuations in the electron density 1 m away from the feed point of a $1.24 \text{ m} \times 0.004 \text{ m}$ dipole antenna immersed in plasma density of $1.24 \times 10^6 \text{ 1/cc}$ ($f_p = 10 \text{ MHz}$) with a magnetic field of $2.5 \times 10^{-4} \text{ Tesla}$ ($f_g = 7 \text{ MHz}$) at an incident angle of 90° .

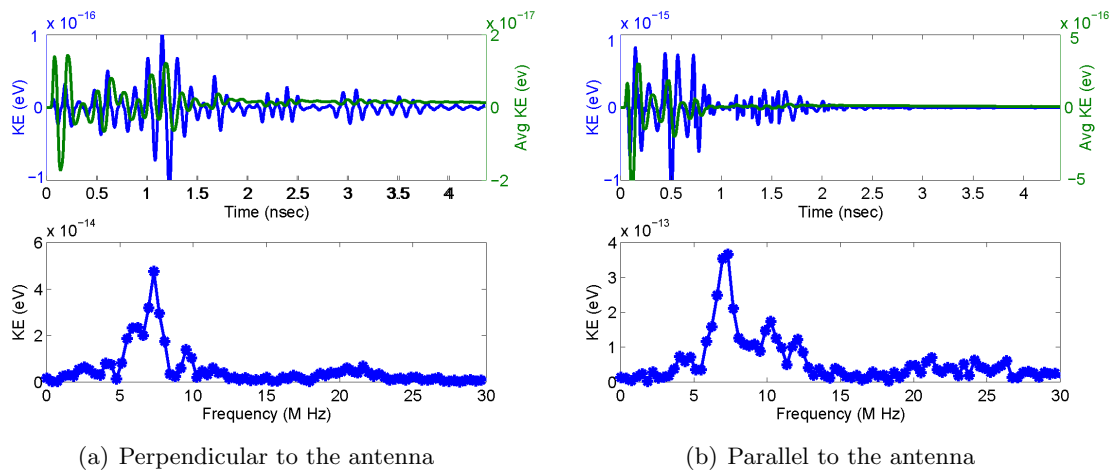


Fig. 3.41: Fluctuations in the radial instantaneous and average kinetic energy 1 m away from the feed point of a $1.24 \text{ m} \times 0.004 \text{ m}$ dipole antenna immersed in plasma density of $1.24 \times 10^6 \text{ 1/cc}$ ($f_p = 10 \text{ MHz}$) with a magnetic field of $2.5 \times 10^{-4} \text{ Tesla}$ ($f_g = 7 \text{ MHz}$) at an incident angle of 90° .

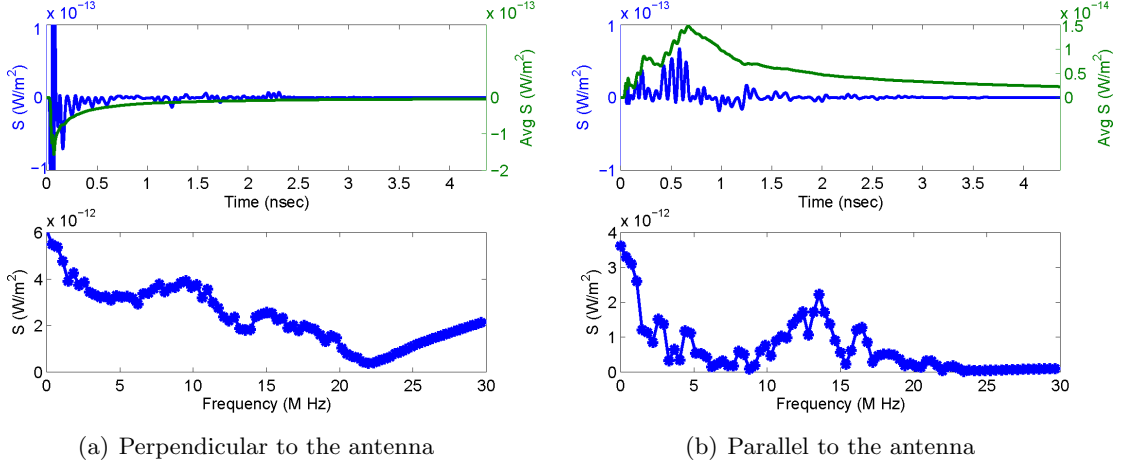


Fig. 3.42: Fluctuations in the radial instantaneous and average Poynting vector 1 m away from the feed point of a $1.24 \text{ m} \times 0.004 \text{ m}$ dipole antenna immersed in plasma density of $1.24 \times 10^6 \text{ 1/cc}$ ($f_p = 10 \text{ MHz}$) with a magnetic field of $2.5 \times 10^{-4} \text{ Tesla}$ ($f_g = 7 \text{ MHz}$) at an incident angle of 90° .

the $|Z|$ at the gyro resonance increases, the 'upper hybrid' zero impedance phase point shifts, and the "low" frequency effects are the same as in the $\omega_p > \Omega$ case (see fig. 3.43).

Current Distributions

The current distribution behaves as expected. There is very little change in $|I(l)|$ and the change in $\angle I(l)$ is in line with the observations of the $\omega_p > \Omega$ case (compare figs. 3.44 and 3.45 to figs. 3.29-3.30 and 3.36-3.39).

Energy Flows

Like the field for the $f_p > f_g$ case with an incident angle of 90° , the field and energy variations remain relatively difficult to quantify beyond what has already been discussed above, at least without expanding the simulation size and scope. However for completeness, the same fields; the density (fig. 3.46), kinetic energy (fig. 3.47), and Poynting vector (fig. 3.48) are included.

3.6 Additional Observations

The main reason for developing the PF-FDTD was to improve the modeling of the

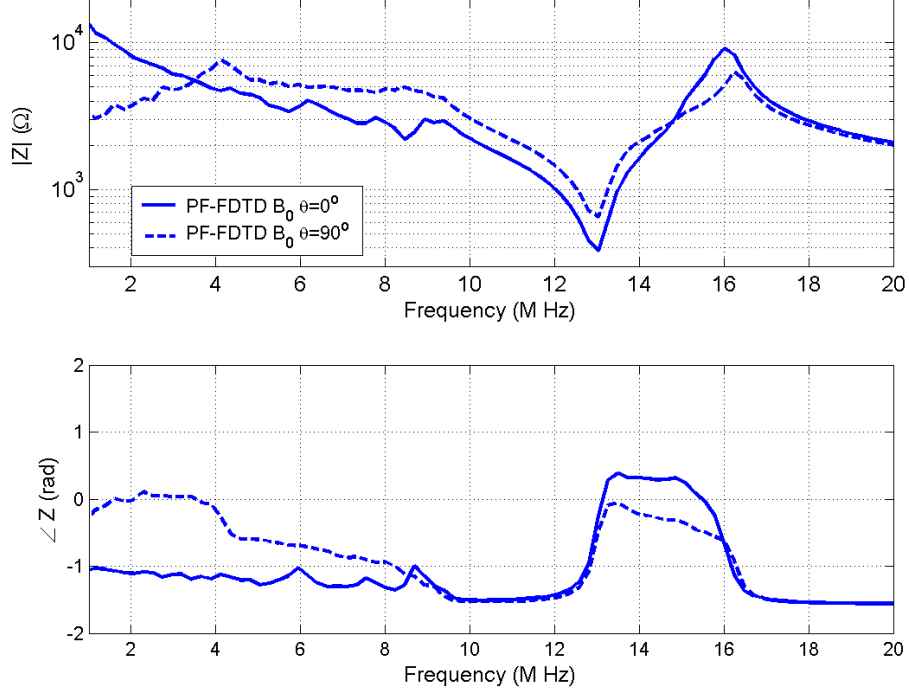


Fig. 3.43: The PF-FDTD versus Balmain for a $1.24 \text{ m} \times 0.004 \text{ m}$ dipole for various magnetic field incident angles with a plasma density of $1.24 \times 10^4 \text{ 1/cc}$ ($f_p = 1 \text{ MHz}$) and a magnetic field of $4.6 \times 10^{-4} \text{ Tesla}$ ($f_g = 13 \text{ MHz}$). The PF-FDTD ran for 2^{16} iterations, 40 plasma cycles.

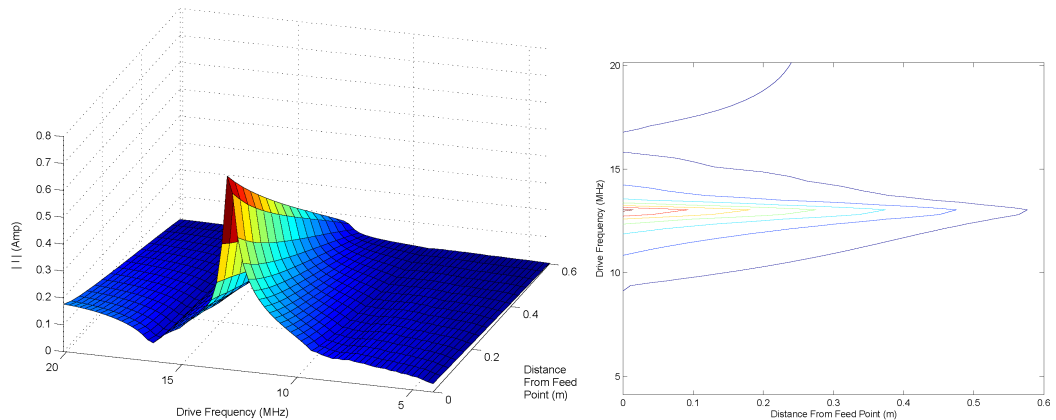


Fig. 3.44: The magnitude of the current distribution along a $1.24 \text{ m} \times 0.004 \text{ m}$ dipole antenna immersed in plasma density of $1.24 \times 10^6 \text{ 1/cc}$ ($f_p = 10 \text{ MHz}$) with a magnetic field of $4.6 \times 10^{-4} \text{ Tesla}$ ($f_g = 13 \text{ MHz}$) at an incident angle of 90° for various drive frequencies.

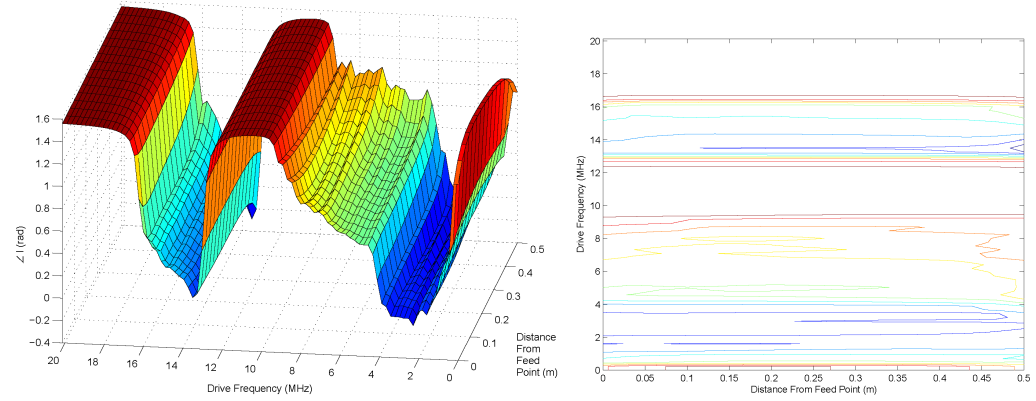


Fig. 3.45: The phase of the current distribution along a $1.24 \text{ m} \times 0.004 \text{ m}$ dipole antenna immersed in plasma density of $1.24 \times 10^6 \text{ 1/cc}$ ($f_p = 10 \text{ MHz}$) with a magnetic field of $4.6 \times 10^{-4} \text{ Tesla}$ ($f_g = 13 \text{ MHz}$) at an incident angle of 90° for various drive frequencies. The drive voltage is set to zero phase.

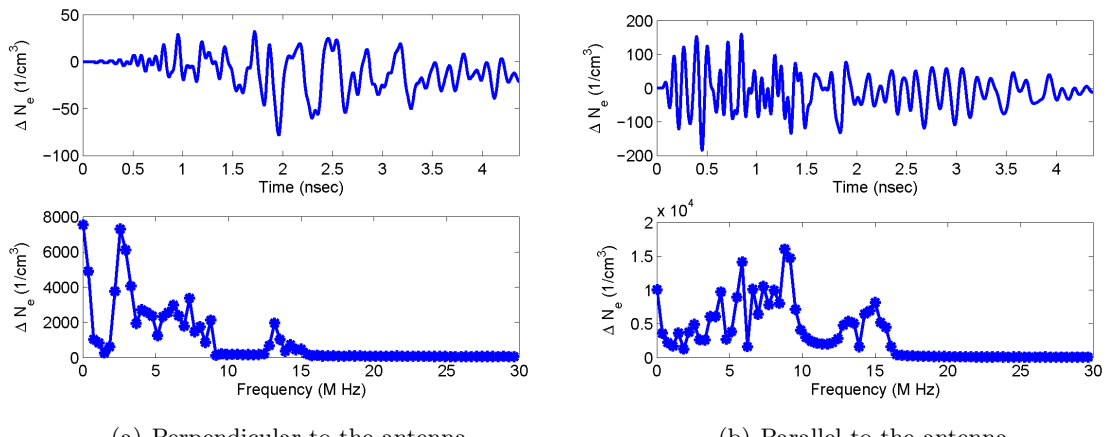


Fig. 3.46: Fluctuations in the electron density 1 m away from the feed point of a $1.24 \text{ m} \times 0.004 \text{ m}$ dipole antenna immersed in plasma density of $1.24 \times 10^6 \text{ 1/cc}$ ($f_p = 10 \text{ MHz}$) with a magnetic field of $4.6 \times 10^{-4} \text{ Tesla}$ ($f_g = 13 \text{ MHz}$) at an incident angle of 90° .

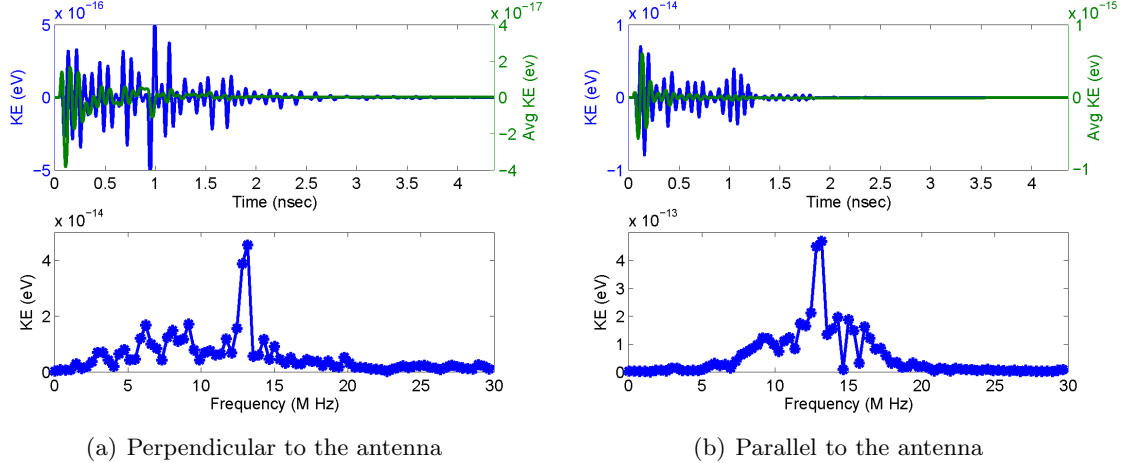


Fig. 3.47: Fluctuations in the radial instantaneous and average kinetic energy 1 m away from the feed point of a $1.24 \text{ m} \times 0.004 \text{ m}$ dipole antenna immersed in plasma density of $1.24 \times 10^6 \text{ 1/cc}$ ($f_p = 10 \text{ MHz}$) with a magnetic field of $4.6 \times 10^{-4} \text{ Tesla}$ ($f_g = 13 \text{ MHz}$) at an incident angle of 90° .

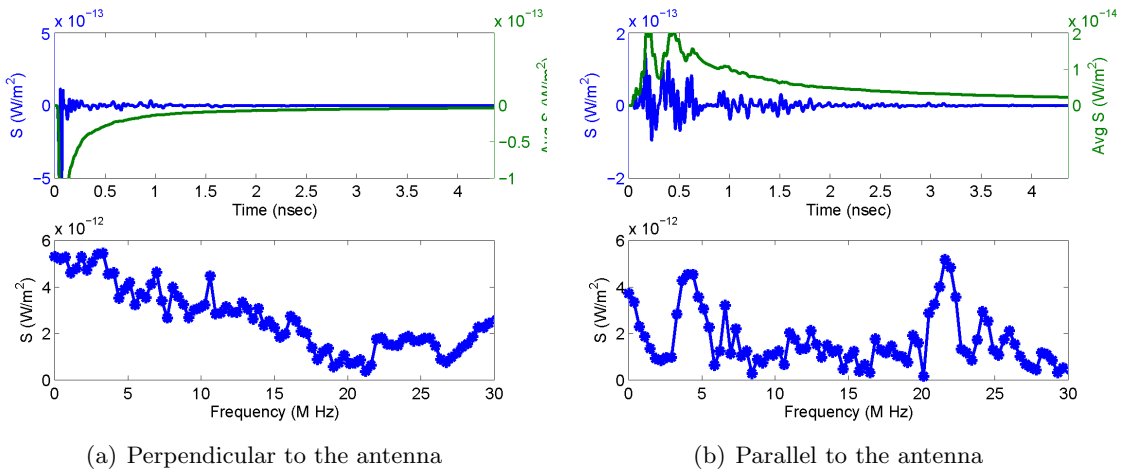


Fig. 3.48: Fluctuations in the radial instantaneous and average Poynting vector 1 m away from the feed point of a $1.24 \text{ m} \times 0.004 \text{ m}$ dipole antenna immersed in plasma density of $1.24 \times 10^6 \text{ 1/cc}$ ($f_p = 10 \text{ MHz}$) with a magnetic field of $4.6 \times 10^{-4} \text{ Tesla}$ ($f_g = 13 \text{ MHz}$) at an incident angle of 90° .

antenna plasma interaction. While the previous sections outlined many of the improvements of the PF-FDTD over the standard analytical results, there is still far more that can be analyzed. This section will briefly present a few additional topics that can be explored with the PF-FDTD. Specifically, the effect of an electron neutral collision frequency, the effect of a plasma temperature, and the effect that a multi ion species plasma has on the input impedance of an antenna, as well as a far field analysis of the fields around a RF plasma probe. Though these areas of research are included here, this section is not meant to become a definitive resource, but merely to demonstrate the effectiveness of the PF-FDTD.

3.6.1 Varying the Electron Neutral Collision Frequency

To date there has not been an in-situ instrument capable of measuring the electron neutral collision frequency much less the electron/ion or ion/ion collision frequencies. In fact, researchers are usually forced to use tabulated results that are dependent upon the known species and temperature [42]. However, as implied by Pfister and Balmain [9,11,24], the quality of the resonance conditions can be used to determine the dispersive nature of the plasma and thereby the collision rate. The only problem has been an accurate model of these resonances.

The electron neutral collision frequency can be defined as the rate that electrons elastically collide with neutral particles. This collision effectively increases and/or decreases the mean free path that an electron must traverse in order to complete an oscillation. The variation of the oscillation path causes the electron to impact the input impedance over a selective band around the natural resonances, see fig. 3.49. For example, the magnitude of the upper hybrid can be decreased as the electron neutral collisions cause the energy to be absorbed over a wider band. The same can be said for the gyro frequency. Barjatya and Swenson have even attempted to monitor the collision frequency by measuring the quality of these resonance conditions [55], where the quality (Q) is defined as

$$Q = \frac{\text{Resonance Frequency}}{\text{Bandwidth}}, \quad (3.12)$$

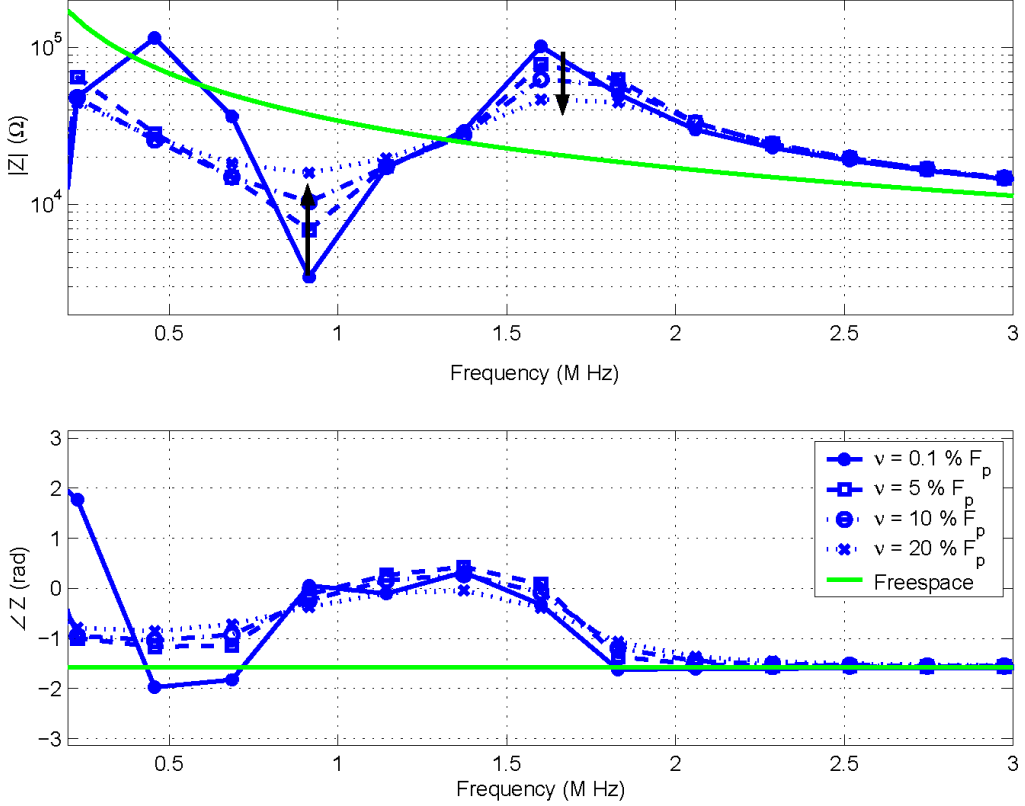


Fig. 3.49: The PF-FDTD for a $1.24 \text{ m} \times 0.004 \text{ m}$ dipole with a plasma density of $2.94 \times 10^4 \text{ 1/cc}$ ($f_p = 1.54 \text{ MHz}$) and a magnetic field of $3.2 \times 10^{-5} \text{ Tesla}$ ($f_g = 0.9 \text{ MHz}$) for various electron-neutral collision rates. The PF-FDTD ran for 2^{16} iterations, 4 plasma cycles.

A low collision frequency yields a sharp resonance, a high Q factor. The higher the collisions, the broader the resonance becomes. This implies a smaller Q factor.

Until now, questionable current distribution and/or errors in calculating the residue of the singularity have always cast some doubt on the accuracy of the analytical theories. However, the improved accuracy of the PF-FDTD enables researchers to avoid these problems and actually model the resonances. This in turn allows for the proper diagnostics of the electron collision frequency. Moreover, the PF-FDTD can also use this technique to theoretically monitor other collisional frequencies as they effect different resonance conditions. For example, it should be possible to measure the electron ion collision rate by monitoring the effects at the lower hybrid oscillation (the multiplication of the various gyro frequencies $\omega_{lh}^2 = \Omega_e \Omega_i$). However, additional simulations are needed to verify this concept.

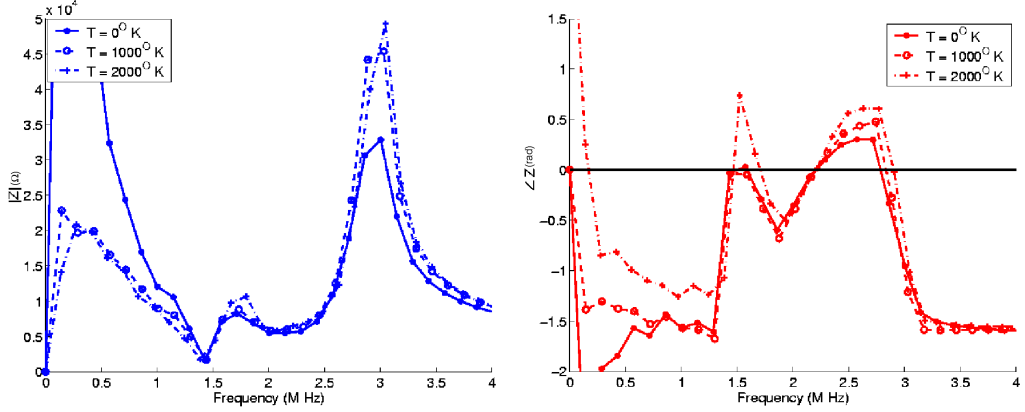


Fig. 3.50: The PF-FDTD for a $1.2 \text{ m} \times 0.01 \text{ m}$ dipole with a plasma density of $7.15 \times 10^4 \text{ 1/cc}$ ($f_p = 2.4 \text{ MHz}$), a magnetic field of $5.36 \times 10^{-5} \text{ Tesla}$ ($f_g = 1.5 \text{ MHz}$), and a electron neutral collision frequency of 0.1 MHz for various isotropic plasma temperatures.

3.6.2 Temperature and Sheath Effects

The PF-FDTD, with the addition of the pressure term (the ideal gas law), theoretically becomes capable of modeling some of the effects that a plasma temperature could have on the input impedance of an antenna. However, the apparent plasma temperature effects become difficult to isolate, see fig. 3.50. In fact, it appears as if instead of a single largely effected region, multiple regions are minimally affected by the plasma temperature. However, it is difficult to relate these effects to the presence of traditional warm plasma waves. This is also complicated by the fact that the current regions of input impedance variations, around the upper hybrid and gyro frequencies, are also effected by the collision frequency and the magnetic field incident angle. This complicates the actual development of a formalized relationship between warm plasma and the input impedance of an antenna.

However, in discussing the temperature effects using the PF-FDTD, one must remember the limiting factors associated with the underlining equations, namely the fact that the ideal gas law is used to terminate the fluid equation series. This prevents the modeling of anisotropic pressures, thermal diffusion, and thermal conduction features that may actually improve the diagnostics of the plasma temperature. Moreover, if research is to continue in the study of the warm plasma, it is strongly suggested that these higher order fluid equations be added to the PF-FDTD, the conservation of energy, the pressure tensor equation, and

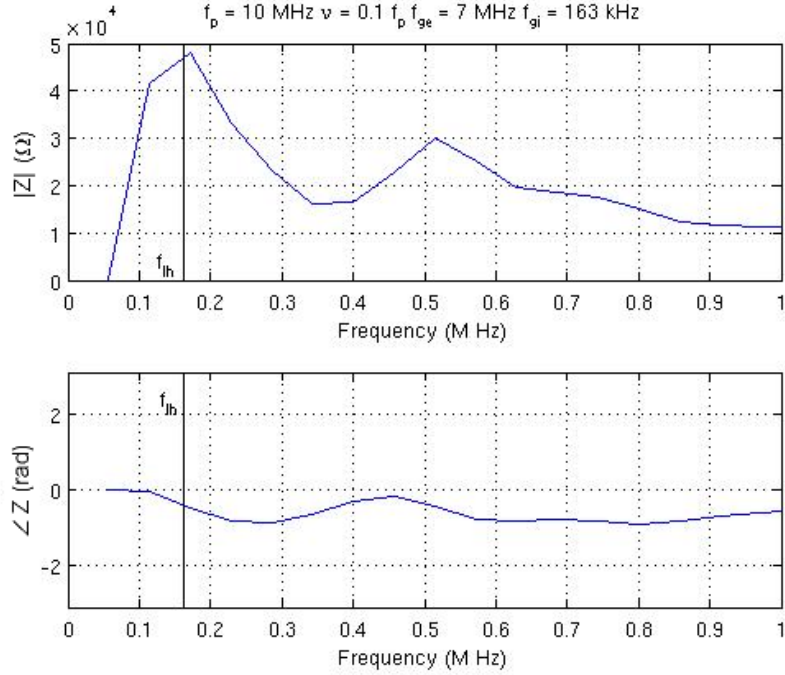


Fig. 3.51: A PF-FDTD simulation of a 1-meter dipole antenna, showing the lower hybrid resonance frequency for an electron and H^+ plasma.

possibly the heat flow equation. This however introduces a higher degree of complexity and is beyond the scope of this current dissertation.

3.6.3 Ion Effects

With the addition of another set of continuity and momentum equations, the PF-FDTD becomes capable of modeling additional plasma species. However, care must be taken as ions have resonance frequencies well below the electron resonances and as such, require the simulations to run for several hundred plasma cycles. Nevertheless, with the proper attention to details and enough time to let a simulation run, interesting results can be achieved, see fig. 3.51.

Figure 3.51 shows the presence of a resonance type structure located near the expected lower hybrid oscillation. While the resolution of this peak is difficult to distinguish, since the frequency resolution is only 80 kHz, it coincides with what is conceptually expected. In that, the lower hybrid oscillation requires electrons to cross magnetic field lines. This produces

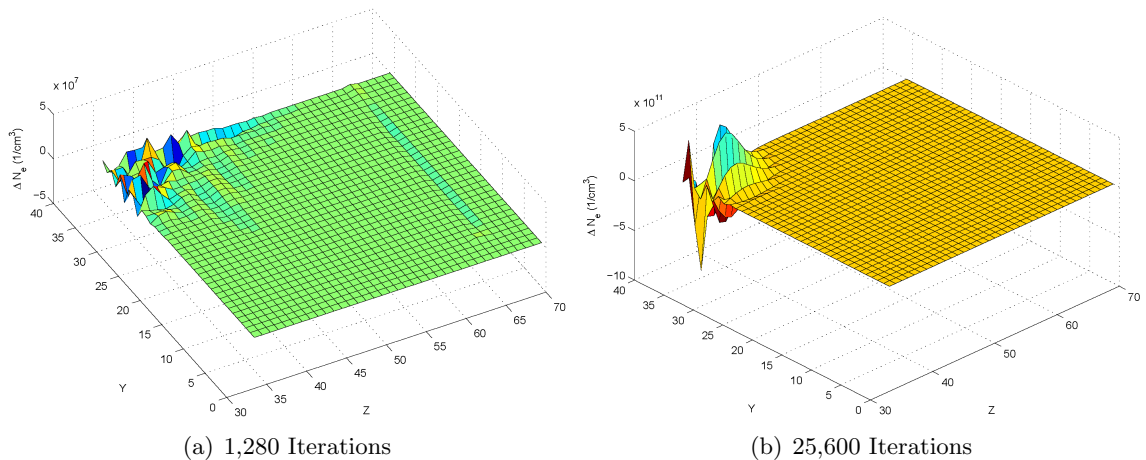


Fig. 3.52: Density fluctuations in the plane of the antenna for a $1.2\text{ m} \times 0.03\text{ m}$ dipole antenna immersed in plasma density of $1.24 \times 10^6 \text{ 1/cc}$ ($f_p = 10\text{MHz}$) with a magnetic field of 2.5×10^{-4} Tesla ($f_g = 7\text{MHz}$) at an incident angle of 0° . The antenna comprises the three cells located at $y = 35$ and $z = (34, 36)$.

the highly reactive type resonance condition, similar to the upper hybrid. While only a few simulations have been performed to this degree, it appears possible to use the location and quality of this resonance to measure the ion species and electron ion collision frequencies. However, additional simulations are still needed to develop a formalized expression. It should also be noted that a similar feature was witnessed in the sounding rocket data of the EWinds campaign, see Chapter 4.

3.6.4 Far Fields Effects

The PF-FDTD is also capable of analyzing the far field effects of an antenna. However, this can be problematic due to the increased simulation size required to model the far field effect. This increase in size requires that either additional computational memory and time are used, or the spatial resolution of the simulation is reduced. This makes it difficult to obtain accurate input impedance characteristic curves and monitor the far field effects at the same time.

Figures 3.52-3.54 show the effects of a 3 by 1 $dx = dy = dz = 0.3$ m PF-FDTD celled, center feed, dipole antenna at two different time steps. A gaussian derivative source

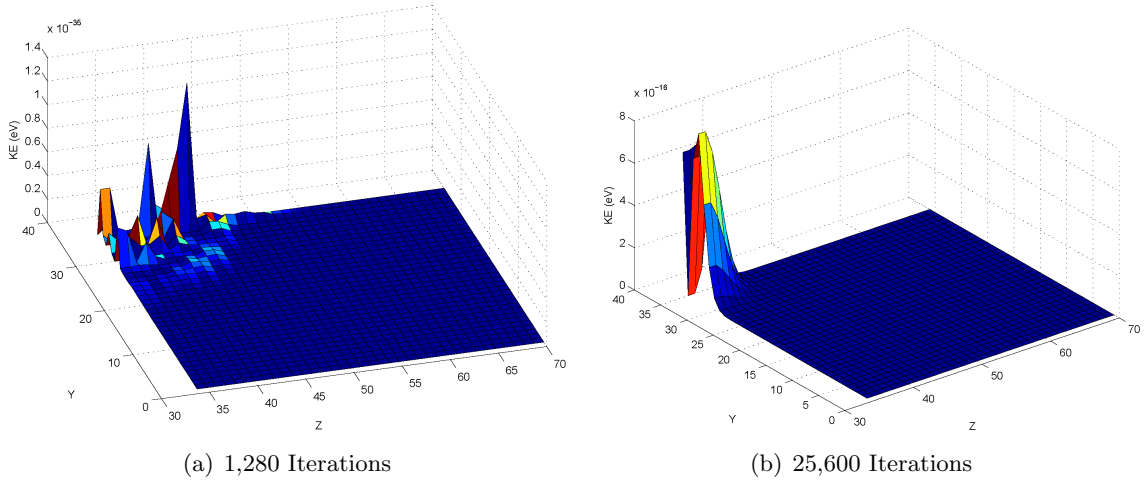


Fig. 3.53: Radial kinetic energy fluctuations in the plane of the antenna for a $1.2 \text{ m} \times 0.03 \text{ m}$ dipole antenna immersed in plasma density of $1.24 \times 10^6 \text{ 1/cc}$ ($f_p = 10 \text{ MHz}$) with a magnetic field of $2.5 \times 10^{-4} \text{ Tesla}$ ($f_g = 7 \text{ MHz}$) at an incident angle of 0° . The antenna comprises the three cells located at $y = 35$ and $z = (34, 36)$.

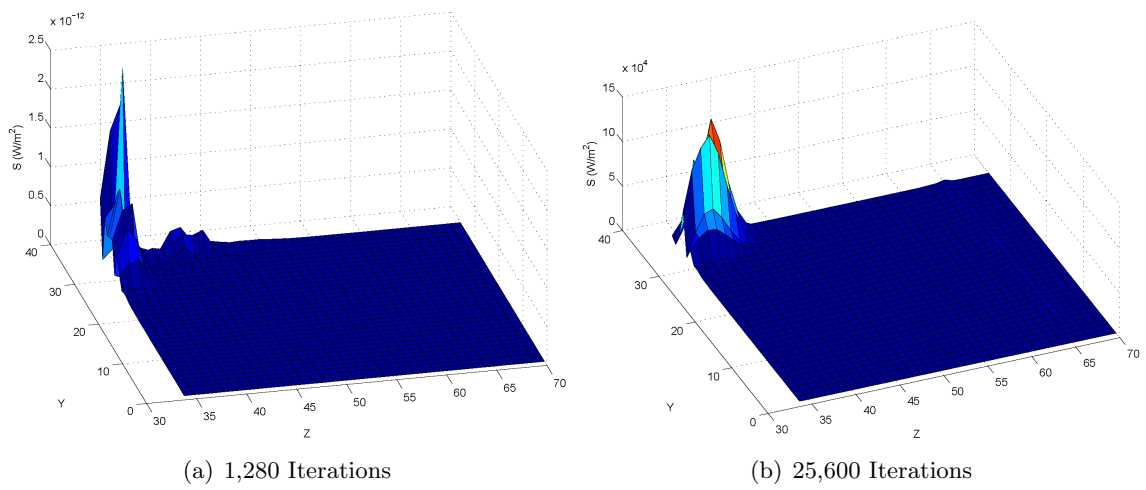


Fig. 3.54: Radial Poynting vector fluctuations in the plane of the antenna for a $1.2\text{ m} \times 0.03\text{ m}$ dipole antenna immersed in plasma density of $1.24 \times 10^6 \text{ 1/cc}$ ($f_p = 10\text{ MHz}$) with a magnetic field of $2.5 \times 10^{-4}\text{ Tesla}$ ($f_g = 7\text{ MHz}$) at an incident angle of 0° . The antenna comprises the three cells located at $y = 35$ and $z = (34, 36)$.

has been used so that a direct comparison between these plots and figs. 3.26-3.28 can be made. It should also be noted, that these plots are not meant to be compared to the traditional free-space EM radiation pattern for two reasons. Traditional RF probes operated at very low drive voltages to prevent significant driving of the plasma from occurring. At this lower drive power, the natural shielding of the plasma prevents the creation of the traditional radiation pattern at frequencies below the plasma cut-off frequency. This differs from traditional antennas that are designed to transmit power efficiently from one point to another. The second reason is that the traditional radiation pattern is frequency dependent and is usually only specified for a limited number of frequencies. Figures 3.52-3.54 have been performed at multiple frequencies in order to be directly comparable to the near field effects seen in previous sections. This is not to say that the PF-FDTD could not be used to perform high power, single frequency radiation patterns, but that the current set up has been used to pursue other research. However, if the high power radiation patterns is desired, additional work must be done to the simulation BC so that the added energy flow can be properly dealt with.

The first major effect noticed in figs. 3.52-3.54 is the lack of far field variations. There are two reasons for this. The fast moving EM waves have either been dissipated and/or radiated out of the simulation space. And, the natural shielding nature of the plasma allows for the containment of the lower frequencies waves. It is these waves that coincide with the evanescent plasma effects seen in figs. 3.26-3.28. This evanescent nature aids in maintaining the constant density level assumption in the decoupled boundary condition. The small variation at $z = 65$ in the 1,280 iteration density measurement, is due to a minor violation of this assumption as the fast propagating EM energy impacts the boundary. However, the dissipative nature of the plasma prevents this minor variation from feeding back and corrupting the source data.

Another plasma effect seen in figs. 3.52-3.54 are the high frequency variations that occur near the antenna early in the simulation. These variations result from the plasma being forced to respond to the drive source. As time progresses these variations converge to

a narrow frequency band near the gyro resonance. This also remains true for any naturally restoring impulse type function. It appears that the electrons converge to a slowly dissipating “steady state” response near the gyro frequency, similar to an overdamped resistor inductor capacitor (RLC) circuit.

Other more specific observations are, the presence of a density resonance cone, see $y = 20$, $z = 45$ in the 1,280 iteration density variation, and the acceleration of particles along the length of the antenna. There also appear to be additional effects, such as an increased Poynting vector in the feed plane and antenna plane that remain unexplainable at this time.

Chapter 4

Specific Applications of the PF-FDTD

While most of this thesis has focused on the theoretical use of the PF-FDTD, there remains a practical side to this numerical model, namely to advance the study of the Plasma Impedance Probes (PIP), through a better understanding of the antenna plasma interaction. This chapter will discuss three specific cases in which the PF-FDTD either correctly identifies “new” input impedance features or was used to design an advance PIP.

4.1 The Air Force Research Lab Experiment

In the summer of 2004, and under funding from the Air Force Research Lab (AFRL), the author had the opportunity to help improve a space environment test chamber at Hanscom Air Force Base in Bedford, Massachusetts. In the process of constructing a Langmuir probe, the author was also able to build an RF probe. The following is an experiment that was conducted using the RF probe in AFRL’s plasma chamber, fig. 4.1.

It should be noted that the testing conditions were not ideal for validation of the numerical PF-FDTD model. This was due to the large number of uncontrollable variables and questionable calibration of the network analyzer. However, the experiments did shed light on the qualitative accuracy of the PF-FDTD numerical code.

4.1.1 The Experiment

A small monopole antenna, constructed using a BNC connector and some solid core wire according to the specifications in fig. 4.2, was inserted in the plasma test chamber (see fig. 4.3). A bent grounding plain was used to shield the probe from both the feed line and the mounting hardware. This antenna was connected to a Hewlett Packard 3577A network analyzer.



Fig. 4.1: One of the space environment test chambers located at the Air Force Research Lab in Bedford, Massachusetts.

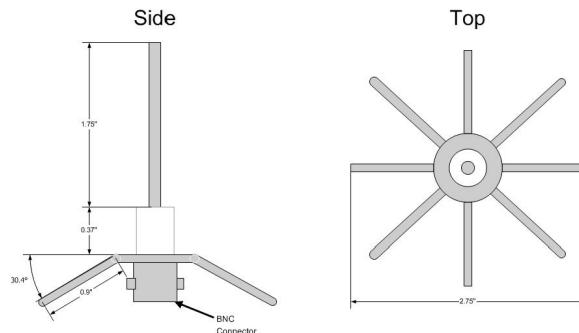


Fig. 4.2: The physical dimensions of the mono pole antenna use for the AFRL experiments.



Fig. 4.3: The RF and Langmuir probes placed within the plasma stream. The Langmuir probe is the gold sphere in the far left and two RF probes are dangling from a horizontal support bar in the center right. One of two plasma sources can also be seen elevated at the end of the chamber.

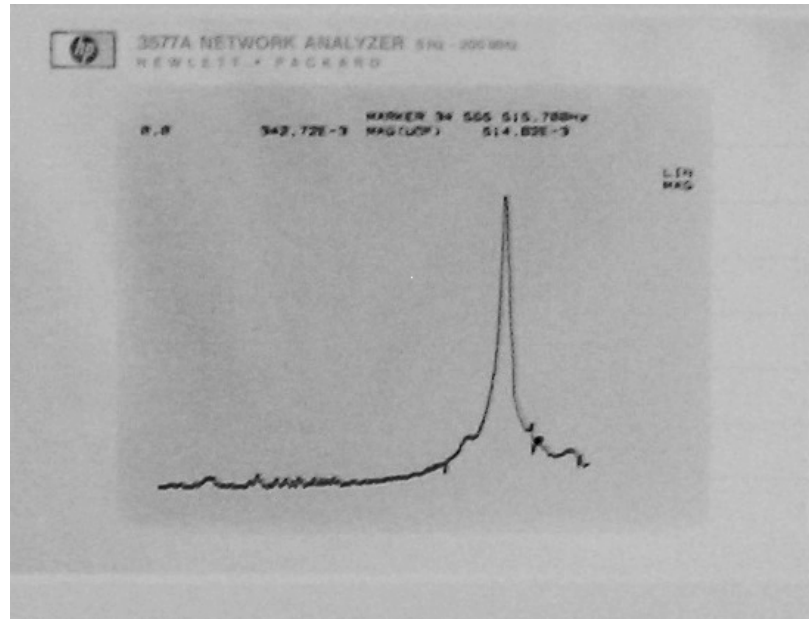


Fig. 4.4: The input impedance magnitude of the AFRL RF probe. The vertical axis is linear while the horizontal axis is logarithmic.

A hollow cathode plasma source was used to generate a stream of ionized nitrogen plasma, with a secondary filament providing a neutralizing element to create some ionized electrons. In addition, as this was very hot plasma, there was an unknown amount of secondary electrons generated from within the un-calibrated chamber.

After an OPEN, SHORT, MATCH calibration of the analyzer was performed at the connection point of the probe and transmission line, the chamber was evacuated to 1.6×10^{-5} Torr. However, this pressure increased to 1×10^{-4} Torr as the nitrogen source was activated.

4.1.2 The Data

Due to the nature of the experiment/equipment, there was no computer connection available for inputting the network analyzer data to and a spare plotter could not be found. As such, only graphically enhanced pictures of the analyzer screen are included in figs. 4.4 and 4.5, the vertical axis is linear while the horizontal axis is logarithmic.

Figures 4.4 and 4.5 clearly show the presence of plasma. The upper hybrid resonance is visible in the center right portion of the screen, while the secondary resonance occurs just

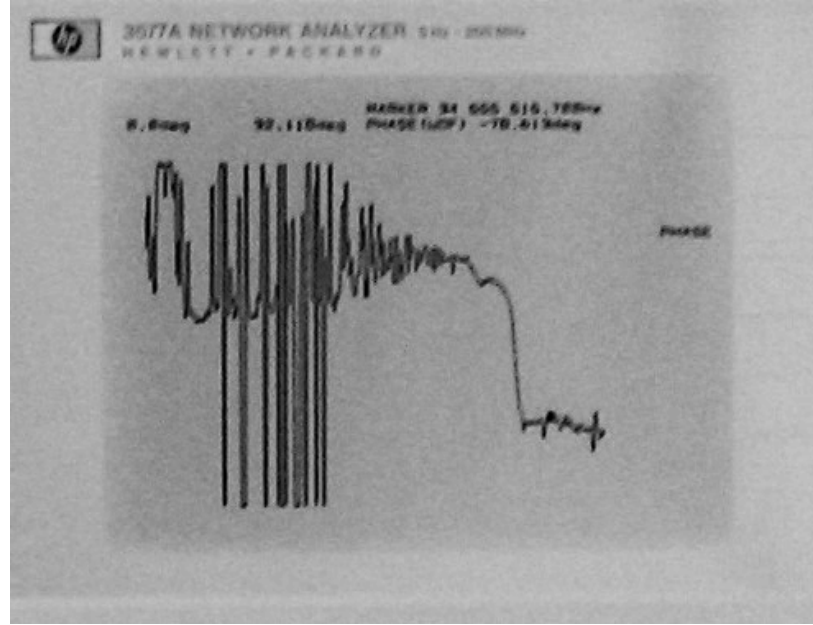


Fig. 4.5: The input impedance phase of the AFRL RF probe. The vertical axis is linear while the horizontal axis is logarithmic.

to the left of the upper hybrid. The proposed “step” in the phase can also be seen to the left of the upper hybrid phase crossing. As this plasma was only magnetized by the Earth’s magnetic field, approximately 3 gauss, the cyclotron resonance is on the order of 0.1 – 1 MHz and is located somewhere within the noise on the left side of the screen.

4.1.3 The Models

The approximate plasma data was visually read off of the network analyzer and plotted using both Balmain’s theory and the PF-FDTD and presented in fig. 4.6. While the crude nature of this experiment makes it difficult to perform a point-by-point comparison between the data and the models, the improved accuracy of the PF-FDTD becomes apparent. The PF-FDTD is able recreate a secondary “resonance” in the magnitude and a “step” in the phase.

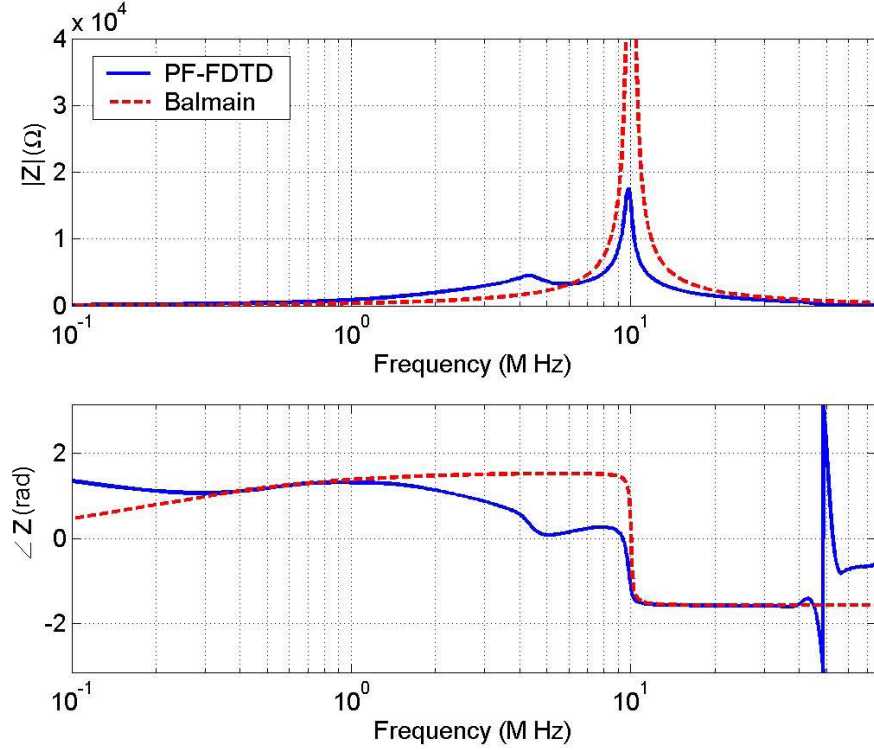


Fig. 4.6: The magnitude and phase of a 1.75 inch monopole (3.5 inch dipole) immersed in plasma density of 4.96×10^6 1/cc ($F_p = 20MHz$) with a magnetic field of 3 gauss ($F_g = 0.8MHz$) according to Balmain and the PF-FDTD.

4.2 EWIND's Ion Probe Data

On July 1, 2003, a Plasma Impedance Probe (PIP) was flown on a series of four sounding rockets that were launched at 3:19, 5:41, 6:50 and 7:07 Universal Time from Wallops Island, Virginia into the nighttime D- and E-regions. Three of the four rockets (41.036, 41.037, 41.038) were Terrier-Improved Orion sounding rockets. Each of these daughter payloads included a Utah State University (USU) PIP and a trimethylaluminum (TMA) canister experiment from Clemson for wind measurement. The other payload was staged on a Nike-Black Brant IX (27.144) and consisted of a PIP as well as three instruments from University of Texas at Dallas (UTD) to measure neutral winds, electric fields, and ion composition.

Figure 4.7 shows the ballistic trajectories of the payloads and the approximate locations of the sporadic E- and descending layers. The circles on each trajectory indicate an

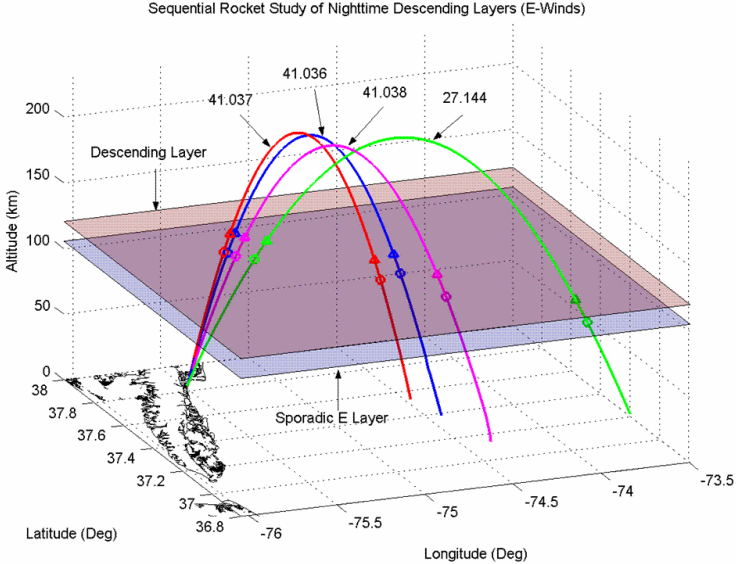


Fig. 4.7: The trajectories of the EWind sounding rocket campaign.

intersection with the sporadic E-layer, and the triangles indicate the intersection with the descending layer. The 41.036-41.038 payloads reached an altitude of approximately 200 km, and the 27.144 payload reached an approximate altitude of 225 km. Spatially, all of the payloads passed through nearly the same area on the upleg with a greater amount of dispersion on the downleg.

As part of the USU PIP payload, one data channel was dedicated to a sweeping dipole antenna over a set of frequencies centered on what was thought to be the ion resonance band. The goal was to perform a measurement of the ion resonance effects on the input impedance of an RF probe. Figure 4.8 shows several sweeps of the ion probe from flight 41.037, on the descending leg near one of the sporadic E-layers. Within this sporadic E-layer, sweep 1346 shows a distinct spike in the input admittance of the probe. Whether this spike coincides with the lower hybrid simulated in section 3.6.3 or is a different electron-ion effect still needs to be answered. Unfortunately, this will take a complete calibration of this probe and a battery of PF-FDTD simulations. However, regardless of this additional analysis effort, it is obvious that some physics exists within the ion resonance region and that the PF-FDTD may be able to explain.

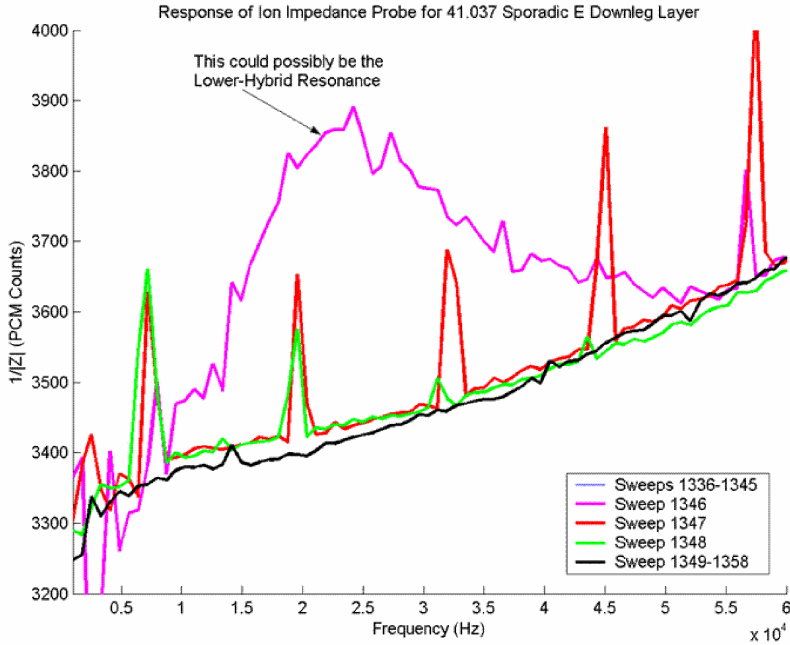


Fig. 4.8: Un-calibrated sweeps of the ion sweeping probe on board flight 41.037 of the EWinds sounding rocket campaign showing the possible presence of the lower hybrid resonance.

4.3 A Microstrip RF Plasma Impedance Probe

One of the biggest benefits of the PF-FDTD is the ability to model any structure that can be decomposed into PF-FDTD cells. This allows research the flexibility to model any antenna shape. In fact, one specific shape of interest is the microstrip patch. Traditional dipole RF probes must be stowed for launch and deployed once the desired elevation is reached. This can be problematic as in the case of the CODA sounding rocket campaign, in which a dipole type impedance probe failed to deploy properly. This could be avoided with the design of a surface mountable RF probe, previously unthinkable with analytical techniques.

4.3.1 The Design

Microstrip patch antennas have been replacing dipole antennas in many situations ranging from communication links to sensors [10,56]. The ability of the microstrip patch to

conform to any surface makes them a natural to place on satellites and sounding rockets. However, there are two major reasons why microstrip antennas have not been used as RF probes. Since researchers have struggled to develop an accurate analytical model for a dipole in a warm collisional magnetized plasma, the problems of a patch in the same plasma becomes extremely difficult. The other reason is that, the majority of the fields created by a traditional patch antennas remain very close to the surface of the patch. As over half of the resulting electric fields remain within the patch structure itself, the sensitivity of a microstrip patch to the variations in the plasma is decreased significantly. This is also compounded by the natural shielding of the plasma and any sheath that exists around the space vehicle. The development of the PF-FDTD overcomes the first difficulty to a microstrip patch RF probe and the use of a Debye Modified microstrip Patch (DMP) addresses the second problem.

The DMP is two traditional microstrip patches stacked on top of each other, with the top two surfaces driven at the same potential. The fields from the bottom patch (the guard) can completely fill the near field of the antenna, while the EM fields emanating from the top patch (the sensor) must traverse through the plasma in order to close on the grounding plain. By adjusting the sizing of the two patches, it becomes possible to force the fields from the sensor to travel farther than the shielding capability of the plasma. In addition, by rolling the edges of the guard around the side of the sensors, the DMP can even be mounted flush with a ground plain. Figure 4.9 shows the results of a free space electrostatic finite difference simulation of a DMP mounted flush with a ground plane. By designing the DMP so that the spacing between the sensor and the ground plane is one quarter to half the size of the expected sheath, it becomes possible to guarantee that the field originating at the sensor element must traverse through a portion of the undisturbed plasma.

4.3.2 The Analysis

When the DMP PIP is modeled using the PF-FDTD, the results appear to be similar to that of a dipole. Figure 4.10 shows one example of plasma parameter variation upon the input impedance of the DMP PIP. The traditional plasma resonances appear in a slightly new shape. The upper hybrid continues to act like a parallel type resonance structure with

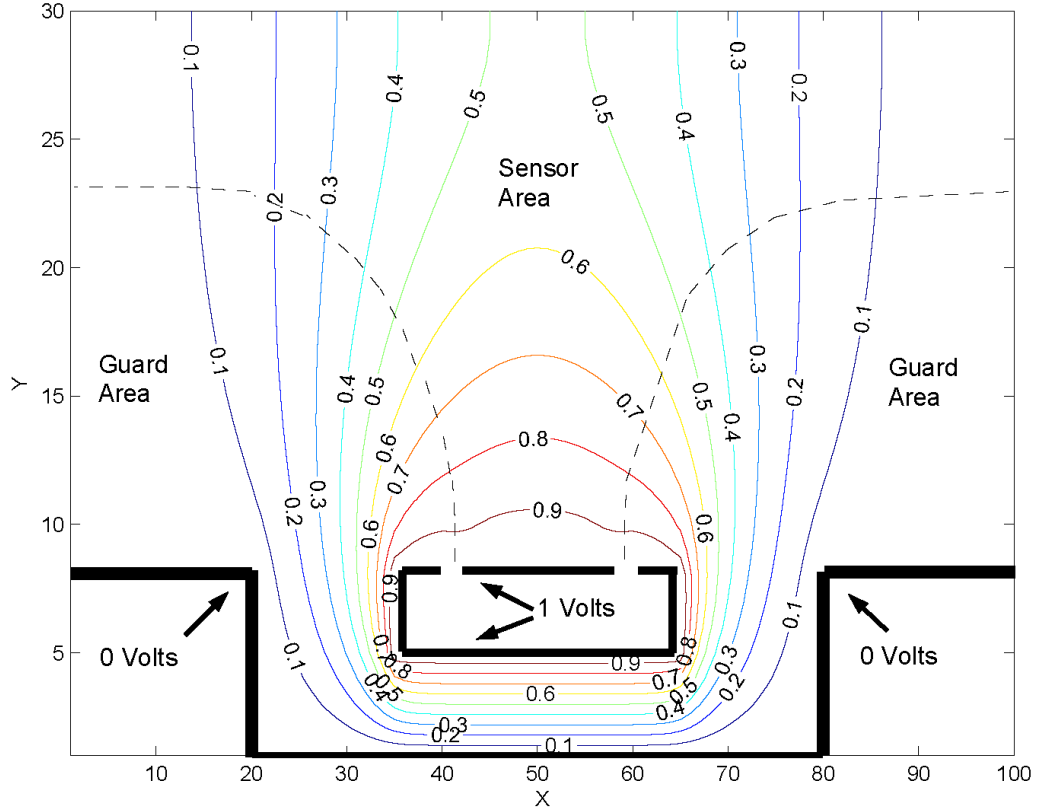


Fig. 4.9: A free space FD simulation showing the various constant potential surfaces for a surface-mounted DMP. Both the guard and patch are driven with a 1 V DC source while the ground plane is maintained at 0 V. Simple matching boundaries are implemented and the fields emanating out of the two patches are separated by the dashed line.

the zero phase point shifted due to the more complex current distribution along the surface of the patch. The phase also becomes capacitive below the gyro resonance. The angle of incident magnetic field also has a variation below the $1/2f_p$ and f_g frequencies. The only difficulty faced in modeling the DMP with the PF-FDTD, is the increased spatial resolution which greatly reduces the low frequency resolution. This forces the use of extremely long simulations and/or frequency scaling in order to yield understandable data sets.

4.3.3 The Flight

On August 7, 2004 and August 15, 2004, two Plasma Impedance Probes (PIP) were flown as part of NASA's Rocket Investigation of Winds Scattering Layers in the Bottomside Equatorial F-Region Ionosphere. This investigation was conducted at the Kwajalein Flight

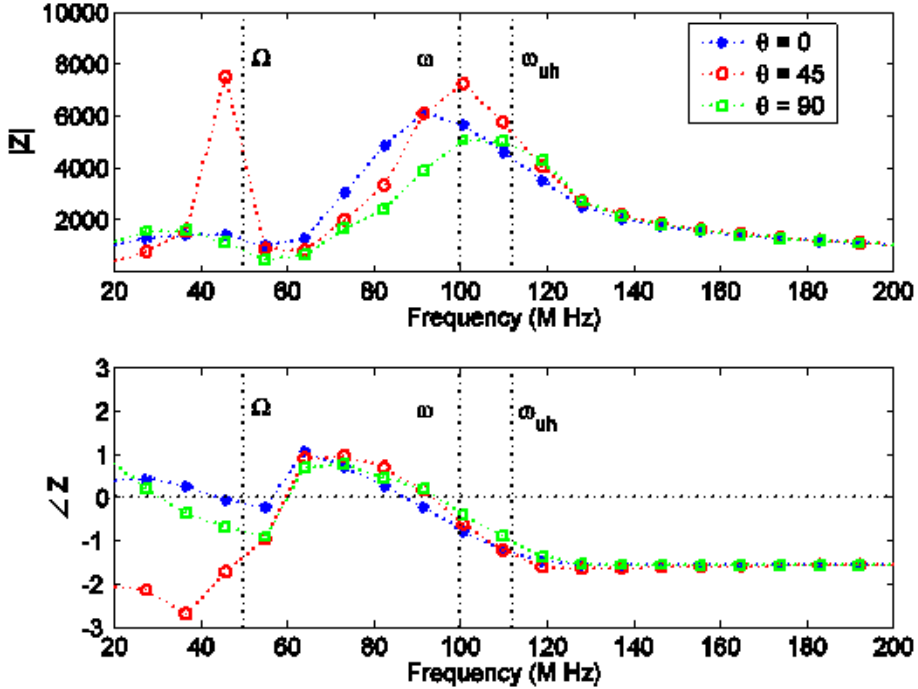


Fig. 4.10: The effects of a magnetized collisional plasma at various incident angles on the input impedance of the DMP PIP according to the PF-FDTD.

Facility in the South Pacific in conjunction with the University of Texas at Dallas (UTD) and Clemson University. These layers had been observed for many years and often occur as a precursor to fully developed equatorial spread F. On board both of these rockets was a traditional PIP and a DMP PIP, see figs. 4.11 and 4.12.

Figure 4.13 shows the uncalibrated magnitude data from the upleg of a single flight. This data set shows the relative peak (red) and dip (blue) of the upper hybrid and gyro resonances as the rocket ascends through the ionosphere. An interesting feature, besides the fact that the DMP worked, is presence of data being collected prior to the fairing ejection. This is data that the dipole PIP and analytical models could not obtain.

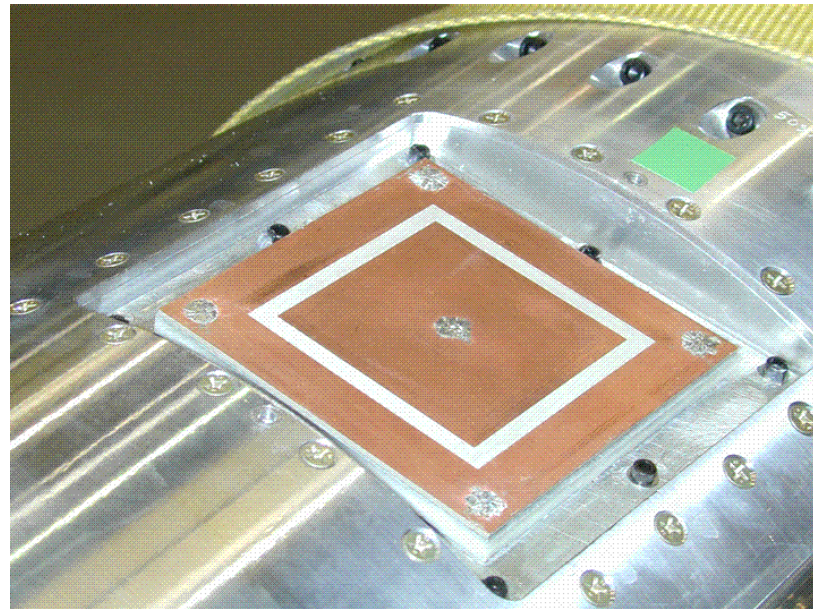


Fig. 4.11: A surface-mounted Debye Modified microstrip Patch (DMP). The center element is the sensor. The outer element and a middle layer are the guard, driven at the same potential as the sensor.

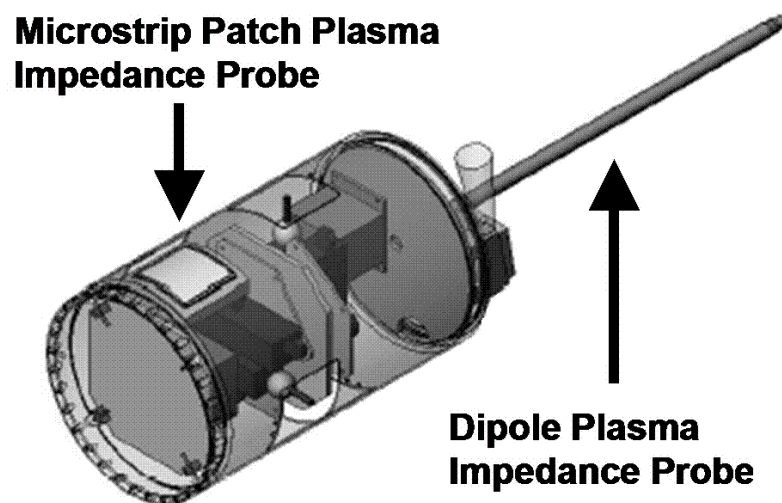


Fig. 4.12: The location of the DMP PIP in reference to the dipole PIP for the EQUIS II sounding rocket campaign.

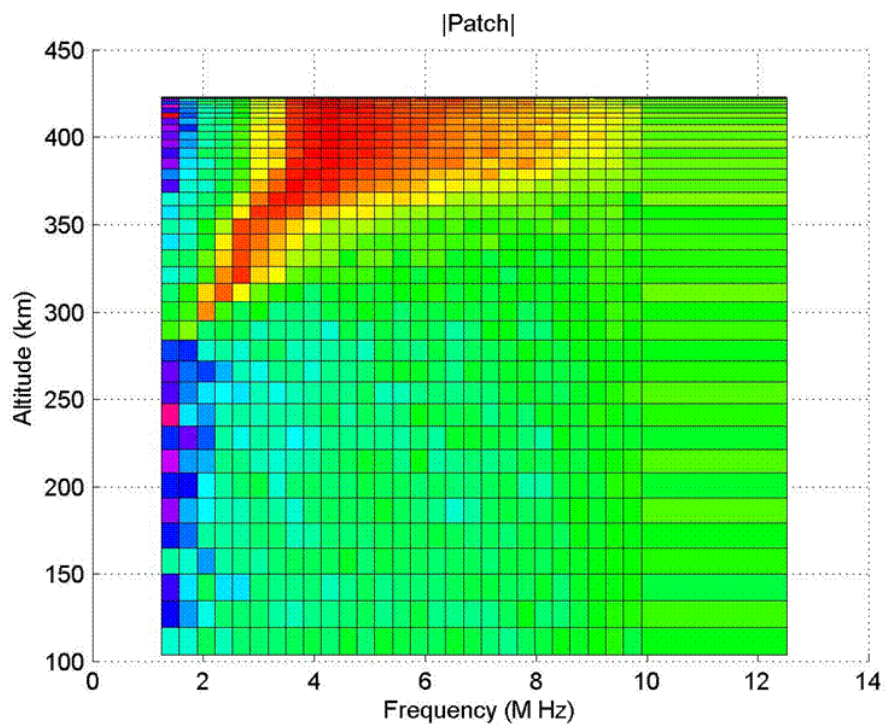


Fig. 4.13: Uncalibrated magnitude data from the DMP PIP on one of the up leg flights showing the presents of the F-region with in the ionosphere.

Chapter 5

Conclusion

Ever since Jackson first documented the effects that a plasma has on the characteristics of an antenna [4, 8], researchers have attempted to quantify the interaction, see Chapter 1. While it remained relatively easy to relate the resonance conditions present on the antenna to the upper hybrid and the gyro frequencies, no technique has been able to accurately describe all the physics seen in actual RF probe measurements [30]. In fact, it was not until the advent of computers and the accompanying numerical techniques that many of the more advanced topics related to an antenna in plasma could even begin to be addressed. The development of the Plasma Fluid Finite Difference Time Domain (PF-FDTD) model is one such attempt. With the development of the PF-FDTD, it has become possible to perform a full wave self-constant numerical analysis of the antenna plasma interaction. In short, the PF-FDTD allows researchers a more accurate way to study the plasma environment.

5.1 The PF-FDTD Summary

Based upon the five moment Maxwellian plasma fluid equations, the PF-FDTD required a rethinking of the traditional Yee cell used for free space FDTD models. Specifically, the plasma density at the center of the cell and a velocity vector that acted upon the density had to be accounted for. In addition, the traditional temporal leapfrog technique also had to be modified, since the classical EM FDTD only alternated between the electric and the magnetic fields. The new timing diagram calculates the electric and magnetic fields for a given time step and then predicts the motion of the plasma based upon the current state of the plasma and the newly applied electromagnetic fields.

This technique works wonderfully as long as the fields propagate uninhibited. However, the need to simulate an effective infinite space forced the development of a new type of

boundary conditions. Traditional EM boundaries are limited by assuming that energy propagates only at the speed of light. This is not always true within plasma. In fact, the application of traditional EM boundaries only introduced additional instabilities. The only way around this was to use a decoupling boundary condition to decouple the EM fast moving waves from the slower compressional plasma waves. With proper implementation of the decoupled boundary conditions a PF-FDTD simulation of warm collisional magnetized multi-species plasma has been run for over 200 electron plasma cycles.

As most of the PF-FDTD simulations consisted of more iterations than traditional EM FDTD models, additional complications began to surface. The rounding off of field values because of small variations and the multiplication of these errors within the continuity, momentum, and Ampères equations forced the introduction of a linearized model. By separating the constant field values from the small perturbations, and realizing that the combination of two small values is smaller than the parts, it became possible to minimize some of the round off errors and extend the number of possible iterations well into the hundreds of plasma cycles.

Additional complications were also identified when a simple dipole antenna was simulated. Not only could modeling errors result from improperly representing the probe using the newly developed cell, but the nature of the source also played an important role in maintaining a stable result. The source has to be naturally restoring, so as not to tax the BCs. Even then, care must be taken not confuse the round off error related to the low power frequencies with the features associated with the plasma response.

Nevertheless, if one is careful in setting up a PF-FDTD simulation by watching the round off errors of the source, leaving enough room between the probe and the boundaries so as not to upset the assumption of the decoupling BC, and properly selecting the bandwidth of the driving source, an immense wealth of information can be obtained. Information ranging from the input impedance, the resulting current distribution, and even the radiating and reactive near and far fields can easily be obtained. In fact, it is in the study of the current distribution and the radiating near fields that many of the differences between the

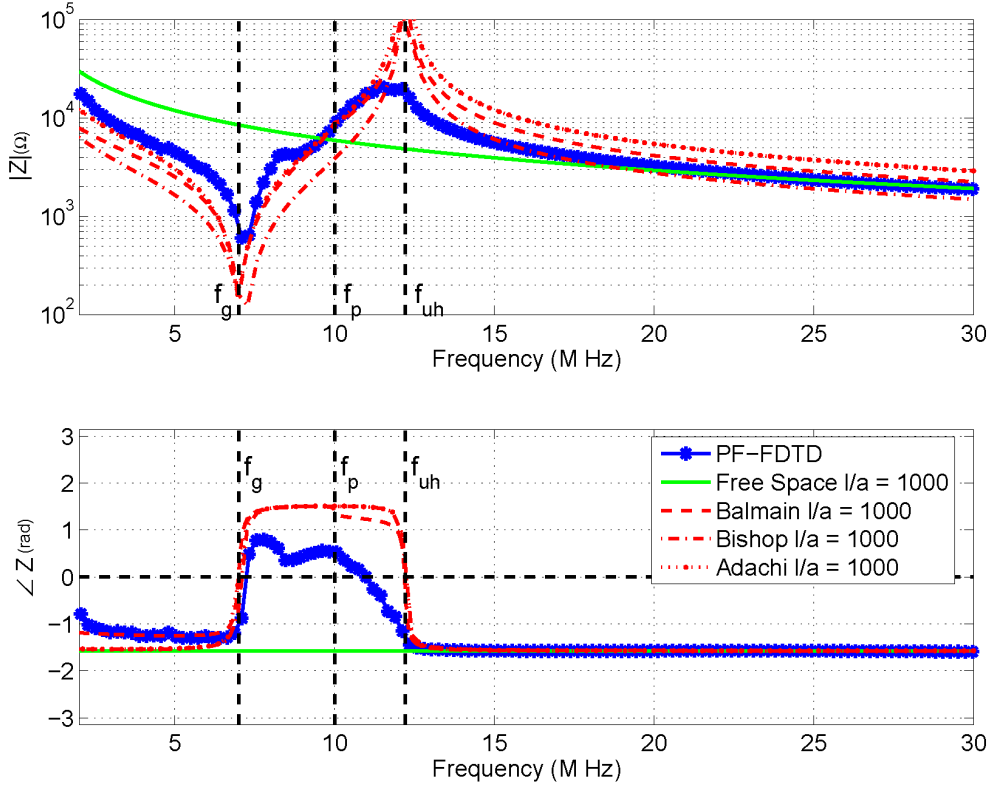


Fig. 5.1: Various approximations of the input impedance for a dipole emersed in a plasma, including the PF-FDTD. The PF-FDTD simulated a 4×0.004 m dipole antenna.

analytical theories and the PF-FDTD are defined. For example, fig. 5.1 compares several analytical theories to the PF-FDTD. The quicker convergence to free space is due to the full wave analysis in actually modeling the Poynting vector. The delay in the upper hybrid zero phase crossing is due to the plasma effecting the phase of the current distribution along the length of the dipole. Additionally, minor phase and magnitude variations seen around 8 MHz are due to the limited bandwidth of the phase variations and energy propagation. The PF-FDTD also enables the study of additional plasma effects, such as the study of the collision frequency, temperature effects, ion effects, and even the far field effects like resonance cones. However, to perform an in-depth analysis of some of these effects additional fluid equations and simulations may be required.

Finally, the fact that the PF-FDTD qualitatively agrees with laboratory experiments,

while enabling various probe geometries to be proposed, opens many new doors to the study of plasma physics.

5.2 Future Work

With all of the physics incorporated into the PF-FDTD the sky becomes the limit for future investigations. Researchers can vary the frequency region, the plasma, and the antenna structure in an attempt to increase their understanding of the antenna plasma interaction. However, before this limit is pushed too high, the PF-FDTD must still be accurately and thoroughly compared to experimental data.

The greatest benefit of numerical models can also be their detriment. The PF-FDTD is no different. While the discretization process can be used to simplify the complex equations, it can also complicate the comparison of the model to unknown experimental data, such as a sounding rocket flight. The continuous nature of the experimental data forces one of three options. First, a massive look up table of all possible combinations can be created from the output of the PF-FDTD. However, this method will require extensive time and resources and will only be as accurate as the range of simulated plasma parameters. The second involves the development of a frequency-scaling factor that would allow a limited set of PF-FDTD simulations to be scaled up and down the frequency region. This requires the normalization of all plasma frequencies to a single scalable value. The third, method requires the development of an analytical equation that fits the PF-FDTD data. However, the accuracy of this interpolation technique depends upon finding the proper function to fit. Both of the latter two options are currently under investigation, with the frequency scaling currently yielding the most promising results.

Once validated, another application of the PF-FDTD could be to analyze other types of probes. In fact, it may be possible to model other electrostatic and electromagnetic type probes such as the Langmuir, E-field, and mutual impedance probes. However, in the case of the Langmuir probe, the higher order fluid equations will need to be added to the simulation.

Finally, additional types of probes may also be developed using the PF-FDTD model.

These new probes could be optimized for specific application. For example, the PF-FDTD could theoretically be used to shrink the Debye Modified microstrip Patch (DMP) down to a size that would fit on a semiconductor wafer, enabling the monitoring of the plasma during a dry etch process. In short, The PF-FDTD opens a world of possibilities.

References

- [1] R. F. Pfaff, "In-situ measurement techniques for ionospheric research," NASA, Goddard Space Flight Center, Tech. Rep., Aug. 1996.
- [2] W. E. Amatucci, D. N. Walker, M. R. Cianciosa, G. Gatling, and P. W. Schuck, "Temporal variation of sounding rocket lagmuir probe contamination." AGU Fall Meeting, 2002.
- [3] K. D. Baker, A. M. Despain, and J. C. Ulwick, "Simultaneous comparison of RF probe techniques for determination of ionospheric electron density," *Journal Geophysical Research*, vol. 71, no. 3, pp. 935–944, Mar. 1966.
- [4] J. E. Jackson and J. A. Kane, "Measurement of ionospheric electron densities using an RF probe technique," *Journal Geophysical Research*, vol. 64, no. 8, pp. 1074–1075, Aug. 1959.
- [5] M. D. Jensen and K. D. Baker, "Measuring ionospheric electron density using the plasma frequency probe," *Journal of Spacecraft and Rockets*, vol. 29, no. 1, pp. 91–95, Jan.-Feb. 1992.
- [6] C. T. Seigies, D. Block, M. Hirt, B. Hipp, A. Piel, and J. Grygorczuk, "Development of a fast impedance probe for absolute electron density measurements in the ionosphere," *Journal of Physics D: Applied Physics*, vol. 33, pp. 405–413, 2000.
- [7] E. J. Lund, M. L. Trimpi, E. H. Gewirtz, R. H. Cook, and J. LaBelle, "The plasma frequency tracker: An instrument for probing the frequency structure of narrow-band MF/HF electric fields," in *Measurements Techniques in Space Plasmas, Fields*, ser. Geophysical Monograph (R. F. Pfaff, J. E. Borovsky, and D. T. Young, Eds.), Washington, DC: American Geophysical Union, 1998, vol. 103, pp. 169–174.
- [8] J. E. Jackson, "Rocket-borne instrumentation for ionosphere propagation experiments." Navel Research Laboratory, Upper Atmosphere Research Report 13, 1952.
- [9] K. G. Balmain, "The properties of antennas in plasmas," *Annales Des Telecommunications*, vol. 35, no. 3-4, pp. 273–283, Mar.-Apr. 1979.
- [10] C. A. Balanis, *Antenna Theory Analysis and Design*, 2nd ed. New York: John Wiley and Sons, 1997.
- [11] W. Pfister, "Survey of RF impedance probes," ser. Direct Aeronic Measurements in Lower Ionosphere, vol. Aeronomy Report 1. Urbana, IL: University of Illinois, Dec. 1963.
- [12] P. Nikitin, "Impedance of a dipole antenna in ionospheric plasma," Master's thesis, Utah State University, Logan, UT, 1998.
- [13] T. H. Stix, *Waves in Plasma*. Ann Arbor: American Instituted Of Physics, 1992.

- [14] P. Nikitin and C. Swenson, "Impedance of a short dipole antenna in a cold plasma," *IEEE Transaction on Antennas and Propagation*, vol. 49, no. 10, pp. 1377–1381, Oct. 2001.
- [15] D. T. Nakatani and H. H. Kuehl, "Input impedance of a short dipole antenna in a warm anisotropic plasma, 1, kinetic theory," *Radio Science*, vol. 11, no. 5, pp. 433–444, 1976.
- [16] S. Ichimaru, *Basic Principles of Plasma Physics*. Boston: W. A. Benjamin Inc, 1973.
- [17] F. F. Chen, *Introduction to Plasma Physics and Controlled Fusion*. New York: Plenum Press, 1984.
- [18] K. G. Balmain and G. A. Oksiutik, "RF probe admittance in the ionosphere theory and experiment," in *Plasma Waves in Space and in the Laboratory* (J. O. Thomas and B. J. Landmark, Eds.), New York: American Elsevier, 1969, vol. 1, pp. 247–261.
- [19] H. Staras, "The impedance of an electric dipole in a magneto-ionic medium," *IEEE Transaction on Antennas and Propagation*, vol. AP-12, pp. 695–702, Nov. 1964.
- [20] J. Galejs, "Impedance of a finite insulated cylindrical antenna in a cold plasma with a longitudinal magnetic field," *IEEE Transaction on Antennas and Propagation*, vol. AP-14, no. 6, pp. 727–736, Nov. 1966.
- [21] R. G. Stone, R. R. Weber, and J. K. Alexander, "Measurement of antenna impedance in the ionosphere – I: Observing frequency below the electron gyro frequency," *Planetary Space Science*, vol. 14, no. 7, pp. 631–639, July 1966.
- [22] R. G. Stone, J. K. Alexander, and R. R. Weber, "Measurement of antenna impedance in the ionosphere – II: Observing frequency greater than the electron gyro frequency," *Planetary Space Science*, vol. 14, no. 10, pp. 1007–1016, Oct. 1966.
- [23] A. A. Andronov and V. Y. Eidman, "Thin cylindrical antenna in an isotropic plasma," *Soviet Physics - Technical Physics*, vol. 14, no. 2, pp. 267–272, Aug. 1969.
- [24] K. G. Balmain, "Dipole admittance for magnetoplasma diagnostics," *IEEE Transaction on Antennas and Propagation*, vol. 17, no. 3, pp. 389–392, May 1969.
- [25] C. C. Bantin and K. G. Balmain, "Monopole and dipole antennas in a nonlinear isotropic plasma," *Canadian Journal of Physics*, vol. 52, no. 4, pp. 302–317, Feb. 1974.
- [26] S. Adachi, T. Ishizone, and Y. Mushiake, "Transmission line theory of antenna impedance in a magnetoplasma," *Radio Science*, vol. 12, no. 1, pp. 23–31, Jan.-Feb. 1977.
- [27] M. A. Matin, K. Sawaya, T. Ishizone, and Y. Mushiake, "Impedance of a monopole antenna over a ground plane and immersed in a magnetoplasma," *IEEE Transaction on Antennas and Propagation*, vol. AP-28, no. 3, pp. 332–341, May 1980.
- [28] N. Meyer-Vernet and C. Perche, "Tool kit for antennae and thermal noise near the plasma frequency," *Journal Geophysical Research*, vol. 94, no. A3, pp. 2405–2415, Mar. 1989.

- [29] K. G. Balmain, "The impedance of a short dipole antenna in a magnetoplasma," *IEEE Transaction on Antennas and Propagation*, vol. AP-12, pp. 605–617, Sept. 1964.
- [30] E. F. Pound, "Personal communications," 2004-2005.
- [31] T. Ishizone, S. Adachi, K. Taira, Y. Mushiake, and K. Miyazaki, "Measurement of antenna current distribution in an anisotropic plasma," *IEEE Transaction on Antennas and Propagation*, vol. AP-17, no. 5, pp. 678–679, Sept. 1969.
- [32] N. Singh, "A boundary-value problem treatment of an electric dipole in a warm isotropic plasma using the multiple water bag model," *Radio Science*, vol. 13, no. 4, pp. 625–637, July 1978.
- [33] T. R. Kaiser and J. K. E. Tunaley, "Radio frequency impedance probes," *Space Science Reviews*, vol. 8, no. 1, pp. 32–73, Mar. 1968.
- [34] R. H. Bishop, *Antenna impedance in the lower ionosphere*. Ph.D. dissertation, University of Utah, Salt Lake City, UT, Sept. 1970.
- [35] M. N. O. Sadiku, *Numerical Techniques in Electromagnetics*, 2nd ed. New York: CRC Press, 2001.
- [36] R. J. Luebbers, F. Hunsberger, and K. S. Kunz, "A frequency-dependent finite-difference time-domain formulation for transient propagation in plasma," *IEEE Transaction on Antennas and Propagation*, vol. 39, no. 1, pp. 29–34, Jan. 1991.
- [37] J. L. Young and R. O. Nelson, "A summary and systematic analysis of FDTD algorithms for linearly dispersive media," *IEEE Antennas and Propagation Magazine*, vol. 43, no. 1, pp. 61–77, Feb. 2001.
- [38] F. Hunsberger, R. Luebbers, and K. Kunz, "Finite-difference time-domain analysis of gyrotrropic media - I: Magnetized plasma," *IEEE Transaction on Antennas and Propagation*, vol. 40, no. 12, pp. 1489–1495, Dec. 1992.
- [39] C. K. Birdsall and A. B. Langdon, *Plasma Physics via Computer Simulations*, ser. Plasma Physics. New York: McGraw-Hill, 1981.
- [40] H. Usui, H. Matsumoto, F. Yamashita, A. Yamamoto, and Y. Omura, "Antenna analysis in magnetized plasma via Particle-In-Cell simulation," *Advances In Space Research*, vol. 34, no. 11, pp. 2433–2436, Nov. 2004.
- [41] M. E. Dieckmann, G. Rowlands, B. Eliasson, and P. K. Shukla, "Particle-in-cell simulations of electron acceleration by a simple capacitative antenna in collisionless plasma," *Journal Geophysical Research*, vol. 109, no. A12, Dec. 2004.
- [42] R. W. Schunk and A. F. Nagy, *Ionospheres Physics, Plasma Physics, and Chemistry*, ser. Cambridge Atmospheric and Space Science Series. New York: Cambridge University Press, 2000.
- [43] J. L. Young and F. P. Brueckner, "A time domain numerical model of a warm plasma," *Radio Science*, vol. 29, no. 2, pp. 451–463, Apr. 1994.

- [44] J. F. Olakangil, “FDTD model of plasma,” Master’s thesis, Utah State University, Logan, UT, 2000.
- [45] K. S. Yee, “Numerical solution of initial boundary value problems involving Maxwell’s equations in isotropic media,” *IEEE Transaction on Antennas and Propagation*, vol. AP-14, no. 3, pp. 302–307, May 1966.
- [46] J. L. Young, “A full finite difference time domain implementation for radio wave propagation in a plasma,” *Radio Science*, vol. 29, no. 6, pp. 1513–1522, Nov.-Dec. 1994.
- [47] K. S. Kunz and R. J. Luebbers, *The Finite Difference Time Domain Method For Electromagnetics*. Boca Raton: CRC Press, 1993.
- [48] S. Berntsen and S. N. Hornsleth, “Retarded time absorbing boundary conditions,” *IEEE Transaction on Antennas and Propagation*, vol. 42, no. 8, pp. 1059–1064, Aug. 1994.
- [49] G. X. Fan and Q. H. Liu, “An FDTD algorithm with perfectly matched layers for general dispersive media,” *IEEE Transaction on Antennas and Propagation*, vol. 48, no. 5, pp. 637–646, May 2000.
- [50] M. N. O. Sadiku, *Numerical Techniques in Electromagnetics*. Ann Arbor: CRC Press, 1992.
- [51] W. H. Press, S. A. Teukolsky, W. T. Vetterling, and B. P. Flannery, *Numerical Recipes in C: The Art of Scientific Computing*, 2nd ed. New York: Cambridge University Press, 1992.
- [52] A. V. Oppenheim, A. S. Willsky, and S. H. Nawab, *Signals and Systems*, 2nd ed., ser. Signal Processing Series. Upper Saddle River: Prentice Hall, 1996.
- [53] C. M. Furse, “Faster than fourier ultra-efficient time-to-frequency domain conversions for FDTD simulations,” *IEEE Antennas and Propagation Magazine*, vol. 42, no. 6, pp. 24–34, Dec. 2000.
- [54] R. C. Johnson, *Antenna Engineering Handbook*, 3rd ed. New York: McGraw-Hill, 1993.
- [55] A. Barjatya and C. Swenson, “Analysis of SAL PIP data,” *Under Review*.
- [56] N. Madan, “Embedded antennas for the measurement of dielectric properties of materials,” Master’s thesis, Utah State University, Logan, UT, 2000.

Appendices

Appendix A

Users Guide to the PF-FDTD Program and Supporting Software

The PF-FDTD is actually a combination of several C++ files and Matlab mfiles that once compiled and combined yield a complete package.

A.1 The Fundamental Program (The PF-FDTD)

The C++ files are composed of the main (PF-FDTD.cpp) file with several header/support files.

1. The memallocate.h file performs an efficient pointer type memory allocation for various sized arrays and is a modification/extension of the technique outlined by Press et al. in Numerical Recipes in C. [51].
2. The output.h file contains many of the sub-routines that format and write the data to the output .vc and .fd files.
3. The plasma.h file contains all of the sub-routines related to the plasma environment. Without this file, the PF-FDTD is similar to any free space FDTD.
4. The retard.h file is an implementation of the Retarded Time Absorbing Boundary Conditions by Berntsen and Hornsleth [48].
5. The source.h file contains a compilation of several different types of sources that can be used to stimulate an antenna.

The PF-FDTD was laid out in such a way so as to enable easy upgrades. For example, to replace the retarded time absorbing boundaries with a perfectly matched layer, only

the retard.h file needs to be replaced. However, as outlined in Chapters 2 and 3, little improvement can be made by only adding a more advanced EM BC.

While many of the more fundamental parameters are meant to be entered at the command line or in a script type file, it may be necessary to modify the header/global section of the plasma.h file. Specifically, in order to implement multi-species plasmas the number of species (#define NS 1) must be changed prior to compiling, with the actual type of plasma species (charge and mass) entered in the ‘void PLASMAclear()’ subroutine. Dynamic memory allocation has not currently been implemented on the multi-species variables. As such, the user may get an error or segmentation fault unless all multi-species arrays are defined prior to compiling the code.

Once complied, the PF-FDTD can either accept input from the command line or from a text based script file. In both cases a structure file and output file must be named (appropriate suffixes will be applied within the program), followed by the plasma parameters. The order of the plasma parameters is as follows; the plasma frequency in Hz, the collision frequency entered as a ratio of the plasma frequency, the gyro frequency in Hz, the elevation and azimuth angles of the DC magnetic field in degrees, and the plasma temperature.

If multiple runs are desired, it may be advantageous to construct a script file capable of running the PF-FDTD autonomously. For example:

line 1 pfftdt dipole dipole_10_02_10 10e6 2e5 10e6

line 2 pfftdt dipole dipole_10_02_13_30 10e6 2e5 13e6 30

line 3 pfftdt dipole dipole_10_02_7_30_0_1000 10e6 2e5 7e6 30 0 1000

: :

A.1.1 .STR File

The structure to be simulated by the PF-FDTD is input via a .str file. Modeled after the structure files associated with X-FDTD by REMCOM. The PF-FDTD .str files is laid out so that only minor modifications are needed from the X-FDTD structure file. This

allows the user to use the commercially available graphical user interface to lay out complex structure. If X-FDTD is not available the .str file may still be edited using any text based editor.

The .str is a tab delineated file and can be broken down into five main sections.

1. Grid Parameter: Used to specify the size of the simulation [SX SY SZ] and the size of the cell [dx dy dz]
2. Source Parameters: Used to specify the number and types of sources used within the simulation and output the resulting current. The first three values are the physical location of the source. The next value is the type of electric field, i.e. \vec{E}_x , \vec{E}_y , and \vec{E}_z . This is followed by the type of source and the source parameter (1=Sine with parameter=center frequency in Hz, 2=Pulse with parameter=center frequency in Hz, 3=Raised cosine with parameter=center frequency in Hz, 4=Gaussian with parameter=mean frequency in Hz, 5=Gaussian derivative with parameter=mean frequency in Hz, 6=DC with parameter=DC value in Volts, 7=Sinc with parameter=center frequency in Hz)
3. Dielectric Permittivity: Currently the PF-FDTD only allows two types of scalar isotropic dielectrics to be used.
4. Antenna Structure: This is where the various cell parameters are specified. The first three values are the \hat{x} , \hat{y} , and \hat{z} location of the cell. The next three values are the modifier to the \hat{x} , \hat{y} , and \hat{z} electric fields. A zero implies no modifier (free space). A 1 is metal, and a 2 or a 3 specifies which of the two above dielectrics modify the appropriate electric field. In cells where a dielectric is specified the PF-FDTD automatically sets the conductance term to zero.
5. Output Parameters: This section is used to specify the field values to output to the .fd file. The first value specifies how many iterations are performed between each series of program outputs. The next six values are flags (0 = off, 1 = on) used to identify which field values should be outputted using the following order; Electric fields, Magnetic

fields, Electron velocities, Electron densities, and finally ion velocities and densities. If multiple ions species are used, either all or none of the species will be output. For example, the current version does not allow users to only view the density of one type of ion species. Following the setting of the flags, the user is able to specify the exact range of cells within the simulation to be outputted.

The following is a sample of a .str file for a Gaussian derivative center feed 1.2 m x 0.01 m dipole antenna that will run for up to 5000 iterations or 20 plasma cycles whichever occurs first. The .str file is also written to monitor the current at (35, 35, 33) and (35, 35, 34) every iteration and output the electric, magnetic, electron velocity, and electron density within the region of $10 < x < 60$, $10 < y < 60$, and $31 < z < 35$ every 20 iterations:

```
//Dipole
//Grid Parameters
70 70 65
0.1 0.1 0.1
//Fail Safe Parameters
5000
20
//Source Parameters
2
35 35 33 3 5 100
35 35 34 3 6 0
//Dielectric Parameters
1.2
3.2
//Antenna Structure
11
35 35 28 0 0 1
35 35 29 0 0 1
35 35 30 0 0 1
35 35 31 0 0 1
35 35 32 0 0 1
35 35 33 0 0 1
35 35 34 0 0 1
35 35 35 0 0 1
35 35 36 0 0 1
35 35 37 0 0 1
```

```

35 35 38 0 0 1
//Output Field Info
20 1 1 1 1 0 0
10 10 31
60 60 35

```

A.1.2 .VC File

The .vc file was developed in order to speedup the analysis of the impedance data. Since the primary purpose of the PF-FDTD is to perform these impedance measurements, the voltages and currents of every source specified in the .str file are automatically output to the .vc file every iteration.

The .vc is a tab delineated file where the first column records the iteration time and the first row records the source information 'XY' (X = source number, Y = 1 for voltage value 2 for current value). The actual data for each iteration follows directly below its source definition.

For example, the output .vc file of a two source structure would appear as:

0	11	12	21	22
0.000000e + 00	4.469002e - 06	2.372461e - 08	-0.000000e + 00	0.000000e + 00
6.671114e - 11	4.555598e - 06	3.011637e - 08	-0.000000e + 00	5.930854e - 09
1.334223e - 10	4.643795e - 06	2.180360e - 08	-0.000000e + 00	1.494251e - 08
2.001334e - 10	4.733620e - 06	1.221632e - 08	-0.000000e + 00	2.079290e - 08
2.668446e - 10	4.825103e - 06	8.559181e - 09	-0.000000e + 00	2.082548e - 08
⋮	⋮	⋮	⋮	⋮

A.1.3 .FD File

The .fd file is very similar to the .vc file in that it is a tab delineated file where the first column is used to record the iteration time at which the values in the common row are recorded at, and the first four rows are used to index the data values directly below them. The first row specifies the type of field value and vector component 1Y=Electric, 2Y=Magnetic, 3Y=Velocity, 4Y=Density, X1=x-axis, X2=y-axis, X3=z-axis). The next three rows then specify the \hat{x} , \hat{y} , and \hat{z} location respectfully for the values within that column.

For example, the output of a .fd file for a simulation that was monitoring the electric and magnetic fields for cells $x > 34$, $y > 1$, $z > 35$ would appear as:

0	11	12	13	21	...
0	34	34	34	34	...
0	1	1	1	1	...
0	35	35	35	35	...
0.000000e + 000	0.000000e + 000	0.000000e + 000	0.000000e + 000	0.000000e + 000	...
2.6684460e - 009	-3.3440470e - 008	0.000000e + 000	1.0647940e - 017	0.000000e + 000	...
5.3368910e - 009	-3.1855260e - 007	0.000000e + 000	-2.9211650e - 006	0.000000e + 000	...
8.0053370e - 009	-5.5974550e - 007	0.000000e + 000	-3.5107030e - 006	0.000000e + 000	...
1.0673780e - 008	-5.6062260e - 007	0.000000e + 000	-7.0973550e - 006	0.000000e + 000	...
1.3342230e - 008	-3.3619450e - 007	0.000000e + 000	-1.9912330e - 005	0.000000e + 000	...
:	:	:	:	:	:

A.2 Matlab Files

As graphical techniques are often the best way to analyze large amounts of data, two basic Matlab graphical user interfaces (GUI) have been developed to support the C++ PF-FDTD.

A.2.1 PF-FDTD_imp

The PF-FDTD_imp.m allows a user to interact with the .vc file, see fig. A.1.

Designed to simplify the analysis technique, the PF-FDTD_imp has an interface that enables the end user to compare the impedance or admittance of the free space model of Balanis [10], the analytical models of Balmain and Adachi [24, 26], and the PF-FDTD numerical results.

Designed to be self explanatory, the PF-FDTD_imp allows a user to input the actual length and radius of an antenna as well as the various plasma parameters that the traditional analytical models are dependent upon. Markers can be set at various frequencies and graphs can be overlayed, scaled, or cleared depending upon the desired results.

The PF-FDTD section also enables the user to normalize the data to a second simulation, typically a free space simulation, in order to minimize the antenna effects.

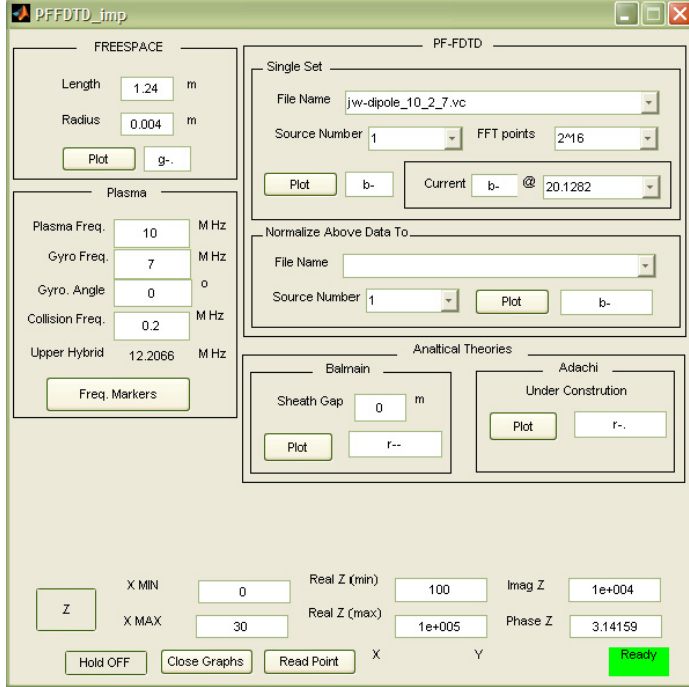


Fig. A.1: A Matlab graphical user interface designed to aid in the analysis of the .vc files.

A.2.2 PF-FDTD_field

The PF-FDTD_field.m allows a user to interact with the .fd file, see fig. A.2.

After the file is loaded via a drop down menu, the various data fields are enabled. The user can then select the field component of interest and view various slices of the field data set. Slide bars enable the user to select the intersection point of three plains within the time span of the complete simulation. Once selected the temporal and frequency variations of the intersection point are displayed at the bottom of the screen, while the various plains are plotted on the right.

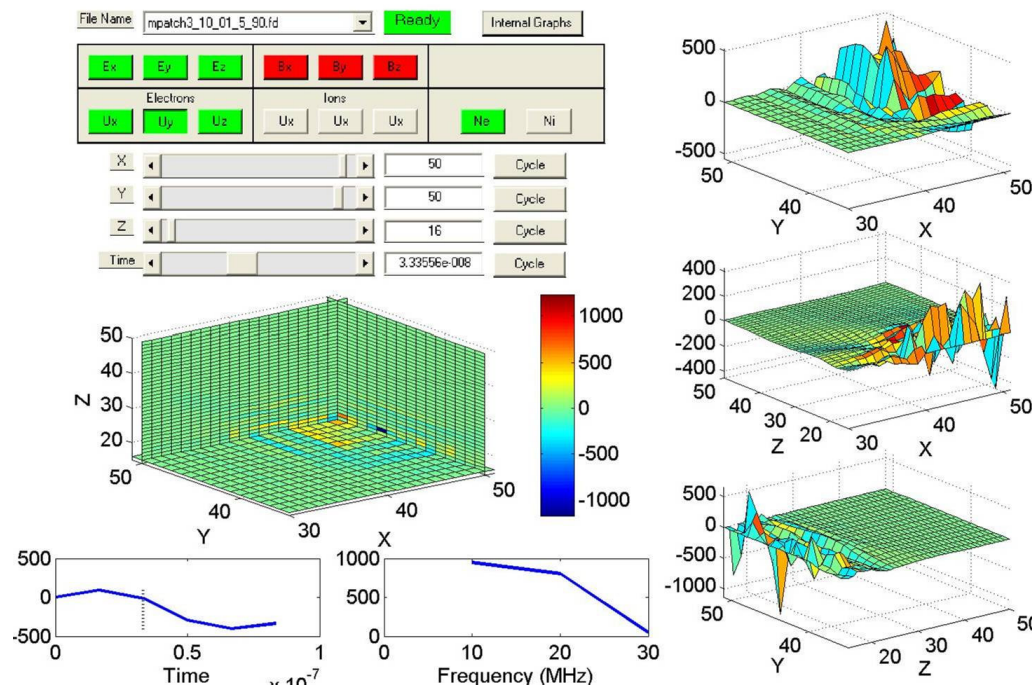


Fig. A.2: A Matlab graphical user interface designed to aid in the analysis of the .fd files.

Appendix B

Index Of Attached CD

The following is a list of the files and directories that may be found on the accompanying CD.

- README.txt file: Consisting of a text version of appendix A.
- Code1.8 directory: The latest version of PF-FDTD code.
- Mfiles directory: The latest set of Matlab scrips used to evaluate data.
- dipole.str file: An example structure file
- dipole.vc file: An example voltage current output file
- dipole.fd file: An example field output file
- JW_Thesis.pdf file: An electronic version of this thesis
- Figures directory: All figures included within this thesis
- Archive directory: Previous versions of PF-FDTD code and mfiles (where space permits)
- Links directory: Any additional information related to the PF-FDTD (where space permits)

Vita

Published Journal Articles

- The impedance of a short dipole antenna in a magnetized plasma via a finite difference time domain model, J. D. Ward, C. M. Swenson, and C. M. Furse, *IEEE Transaction on Antennas and Propagation*, 53(8):2711-2718, Aug 2005.

Conference Presentations / Posters

- Plasma Impedance Probe Diagnostics: Model and Data, C. M. Swenson, J. D. Ward, S. Humphries, C. G. Carlson, C. M. Fish, *Conference on Vehicle Charging*, Mar 2005
- Calibration of the Plasma Impedance Probe for the EQUIS II Sounding Rocket Campaign, J. D. Ward, C. M. Swenson, C. M. Fish, and C. G. Carlson, *AGU National Meeting*, Dec 2004
- Recent advances in the plasma impedance probe measurement technique, C. G. Carlson, C. M. Swenson, C. M. Fish, and J. D. Ward, *URSI National Meeting*, Jan 2004
- The Use of Plasma Fluid Finite Difference Time Domain (PF-FDTD) Models In the Analysis of the E-Winds Plasma Impedance Probe Observations, J. D. Ward, C. M. Swenson, C. G. Carlson, *AGU National Meeting*, Dec 2003
- Finite difference time domain simulations of an impedance probe, J. D. Ward, C. M. Swenson, and C. M. Furse, *AGU National Meeting*, Dec 2002
- Finite difference time domain simulations of an impedance probe, J. D. Ward, C. M. Swenson, and C. M. Furse, *URSI National Meeting*, Jan 2002

- Fdtd analysis of microstrip antennas immersed in anisotropic space plasma, J. D. Ward, C. M. Furse, and C. M. Swenson, *IEEE Antennas and Propagation Symposium, July 2001*

